UNIVERSITÀ
DEGLI STUDI
DI BRESCIA

DOTTORATO DI RICERCA IN INGEGNERIA MECCANICA E INDUSTRIALE (DRIMI)

TeSE – Energy, Fluid & Thermal, and Manufacturing Systems and Technologies

Settore Scientifico Disciplinare (SSD): ING-IND/16

XXXVI CICLO

Optimization of Biomanufacturing process for Tissue Engineering applications

Dottoranda
Rosaria Rovetta

Relatore
Dott.ssa Paola Serena Ginestra

Advisor
Dott.ssa Paola Serena Ginestra

A.A. 2022/2023

Thesis purpose

In recent years, tissue engineering has experienced significant advancements, mostly driven by the emergence of additive manufacturing technologies and the integration of biomaterials and cells. This advanced technique enables the creation of intricate structures with diverse components and properties, specifically designed for use in biomedical applications. The primary benefit of this technology is its ability to be customised, which helps minimise post-operative difficulties for patients with orthopaedic diseases and those undergoing tissue transplants. For this purpose, the essential components can be synthesised by the patient's own cells.

However, there are still other obstacles that need to be addressed in order to get satisfactory 3D printed structures. One key problem is the need to optimise the biomaterial to meet both biocompatibility and printability criteria.

In addition, the production of scaffolds for tissue engineering is a complex procedure as it requires the built structures to closely mimic the extracellular matrix in order to create a functional tissue. The key goal is to produce 3D scaffolds composed of multiple-scale structures made of cell-loaded bioinks.

The objective of this thesis is to create 3D scaffolds for tissue engineering applications using additive manufacturing technologies.

In order to accomplish this, the selection of technology and material is of crucial significance. Therefore, it is essential to optimise both the printing technique and the selected biomaterial.

The literature can assist in determining the essential parameters to be optimised in this regard. However, each specific application necessitates a thorough investigation due to the diverse and unique combinations of material technology and post-processing methods.

The technologies utilised are electrospinning, extrusion-based bioprinting, and laser powder bed fusion. The diverse range of technology provides an overview of how scaffolds can be constructed to meet various scale specifications.

Extrusion-based bioprinting utilises hydrogels, including both synthetic and natural variants, as scaffolding materials. These hydrogels are chosen because of their ability to closely mimic the extracellular matrix, which is essential for the growth of new tissue. In addition, they exhibit an optimal response to printing factors that are valuable for enhancing the printing process itself, with the aim of producing scaffolds that meet both biological and geometric requirements, including the selection of an appropriate crosslinking method.

The Ti6Al4V alloy was used to study the surface properties of an orthopaedic implant. This alloy is specifically suitable for producing orthopaedic implants using laser powder bed fusion technology.

To summarise, this thesis concentrates on the production of 3D scaffolds using additive manufacturing for tissue engineering applications. Every technology posed distinct challenges and concerns that needed to be resolved. In the end, the examination and refinement of the printing parameters and post-processing operations yielded favourable outcomes and improved knowledge of the processes.

Sommario

Negli ultimi anni, l'ingegneria tessutale ha registrato notevoli progressi, soprattutto grazie all'emergere delle tecnologie di produzione additiva e all'integrazione di biomateriali e cellule. Questa tecnica avanzata consente la creazione di strutture complesse con componenti e proprietà diverse, specificamente progettate per l'uso in applicazioni biomediche. Il vantaggio principale di questa tecnologia è la sua capacità di personalizzazione, che aiuta a ridurre al minimo le difficoltà postoperatorie per i pazienti con impianti ortopedici e coloro che subiscono trapianti di tessuto. A tal fine, i componenti essenziali possono essere sintetizzati a partire dalle cellule del paziente.
Tuttavia, ci sono ancora molti ostacoli che devono essere affrontati al fine di ottenere soddisfacenti strutture stampate in 3D. Un problema chiave è la necessità di ottimizzare il biomateriale per soddisfare sia i criteri di biocompatibilità che di stampabilità.
Inoltre, la produzione di *scaffold* per l'ingegneria tissutale è una procedura complessa in quanto richiede che le strutture costruite imitino strettamente la matrice extracellulare al fine di creare un tessuto funzionale. L'obiettivo chiave è quello di produrre *scaffold* 3D composti da strutture multi-scala realizzate con *bioink* contenenti cellule.
L'obiettivo di questa tesi è quello di creare *scaffold* 3D per applicazioni di ingegneria tessutale utilizzando tecnologie di produzione additiva.
Per raggiungere questo obiettivo, la scelta della tecnologia e dei materiali è di fondamentale importanza. Pertanto, è essenziale ottimizzare sia la tecnica di stampa che il biomateriale selezionato.
La letteratura può aiutare a determinare i parametri essenziali da ottimizzare. Tuttavia, ogni applicazione specifica richiede un'indagine approfondita a causa delle diverse e uniche combinazioni tra le tecnologie, i materiali e le strategie di *post-processing*.
Le tecnologie utilizzate sono l'*electrospinning*, l'*extrusion-based bioprinting* e il *laser powder bed fusion*. La diversa gamma di tecnologie fornisce una panoramica di come gli *scaffold* possono essere costruiti per soddisfare le diverse specifiche di scala.
Per la produzione di *scaffold* con l'*extrusion-based bioprinting* vengono utilizzati gli idrogeli a base naturale o sintetica. Gli idrogeli sono particolarmente adatti per la loro capacità di imitare struttura della matrice extracellulare, essenziale per la vita cellulare e il conseguente sviluppo di un nuovo tessuto. Inoltre, esprimono una risposta ottimale ai fattori di stampa che sono preziosi per migliorare il processo di stampa stesso, con l'obiettivo di produrre scaffali che soddisfino sia i requisiti biologici che geometrici, compresa la scelta di un metodo di crosslinking adeguato.
La lega Ti6Al4V è stata utilizzata per studiare le proprietà superficiali di un impianto ortopedico. Questa lega è particolarmente adatta per la produzione di impianti ortopedici utilizzando la tecnologia *laser powder bed fusion*.
Riassumendo, questa tesi si concentra sulla produzione di *scaffold* 3D per applicazioni di ingegneria tissutale, utilizzando diverse tecnologie di produzione additiva. Ogni tecnologia ha presentato sfide e problematiche differenti, lo studio e l'ottimizzazione dei relativi parametri di stampa e le operazioni di post-elaborazione hanno dato risultati favorevoli e migliorato la conoscenza dei processi.

Index

Chapter 1

Introduction

In recent years, production technologies have changed, moving from more traditional "subtracted" methods to more advanced "additive" methods.
Machining, often known as Subtractive Manufacturing (SM), is a highly developed and established technology. It involves using traditional or cutting-edge methods to remove material in the form of chips or particles. One of the SM's greatest advantages is its capacity to create complicated geometries with parts that have extremely high levels of dimensional quality, form, and surface finishes, a capability that sets it apart from parts produced using other methods. However, if the component has extremely complicated geometries, it might not be able to be machined even with interpolation control of five or more axes; in this case, further assembly would be required, which would be time-consuming and expensive [1].
Researchers from the early 1980s began to study new production technologies precisely to overcome these problems, in particular of a solution to the long production and design times required to produce equipment and prototypes, thus the idea of additive production was born [2].
Additive Manufacturing (AM) allows the creation of finished products, semi-finished parts, or both through layer-by-layer addition of different materials, including plastics, metals, ceramics, and composites, either separately or in combination, to create parts with intricate shapes [3].
Given the particular feature of creating geometries starting from a model and adding material is identified as three-dimensional (3D) printing.
The fact that AM may be produced on demand, that the complexity and variety of the parts do not raise the cost, that assembly is not required, and that waste generation is either eliminated or much reduced are some of the advantages that some researchers point out [4].
The domains of biology and biomedicine, which were often unaffected by conventional production technologies, can now be included in the industrial production landscape thanks to AM. Biomanufacturing emerged when researchers started using AM, namely 3D printing, to create parts made of biological and biocompatible materials in the early 2000s.
This has allowed engineering to go beyond the industrial context alone: hybrid forms of engineering are thus born that combine the design and production skills typical of the engineering fields with, for example, biological and biomedical skills.
Biomanufacturing is the process of producing biological systems and components used in biological and biomedical areas, from the synthesis of biomolecules used in the pharmaceutical industries to the creation of scaffolds required for tissue engineering [5].

1.1 Tissue Engineering

Tissue Engineering (TE) is a cross-disciplinary discipline that combines engineering and biological concepts to develop biological substitutes that maintain, enhance, or replace tissue function. The term "tissue engineering" was initially used to refer to methods of manipulating organs and tissues during surgical operations in the middle of the 1980s. Ever since, prosthetic and biomaterial device applications have all been classified as TE [6].

Transplantation, the most extreme type of reconstructive surgery, is an innovative and life-saving procedure involving the transfer of organs and tissues from a donor to a recipient. Despite enormous successes, there remain serious obstacles to the progress of transplantation. The main problem is to provide a sufficient number of tissues and organs to each patient. Additionally, over time, the immune system's continuous rejection and destruction might lead to an imbalance in immune surveillance from immunosuppression, which increases the likelihood of the creation of new tumours. Furthermore, implantable foreign materials have the potential to produce infections over time, ongoing rejection, and adverse immune system interactions, all of which raise the risk of biological changes and the emergence of serious issues.

These limitations have stimulated research and the creation of innovative approaches to provide the necessary tissue. In the early stage of TE development, two approaches were widely adopted: 2D cell culture and 3D tissue culture [7].

The key point in the history of TE development came in the early 1990s, when Joseph Vacanti and Robert Langer [8] proposed a concept of designing appropriate scaffolds to facilitate cell release and proliferation. Existing living cells, usually attached to a scaffold or matrix to direct tissue development, are used to create new functional living tissue. Scaffolds can be natural, artificial or even a combination of both, typically produced using AM.

Prior to implantation, cells can be cultured inside the scaffold or linked to the matrix. As an alternative, they may migrate inside the scaffold after implantation; nevertheless, the true challenge is in developing a scaffold made of a biocompatible material that already contains cells, a process known as 3D bioprinting.

Bioprinting (BP) is a nascent technique that has recently been employed to create and produce 3D cell structures for transplantation therapy.

The capability to fabricate 3D structures using living biological components, including nutrients and cells, is the most alluring feature of this technology.

While there is no universally agreed-upon definition for the word 'bioprinting', researchers have investigated several methods for placing living cells and biomaterials in order to achieve the common goal of producing accurate 3D structures.

The first International Workshop on Bioprinting and Biopatterning [9] was held at the University of Manchester (UK) in September 2004, during which the first formal definition of BP was proposed:

"*the use of material transfer processes for patterning and assembling biologically relevant materials – molecules, cells, tissues, and biodegradable biomaterials – with a prescribed organisation to accomplish one or more biological functions*"

BP is defined as a collection of processes rather than a singular methodology, allowing for a wide range of possibilities and applications. If a technique is capable of transferring biological materials onto a substrate to create 3D structures, it qualifies as a bioprinting process.

The primary objective of BP is to produce viable tissues and organs that may be implanted into human bodies [10].
Mironov *et al*. [11] proposed another possible definition:
"*computer aided 3D tissue engineering of living organs based on the simultaneous deposition of cells and hydrogels with the principles of self assembly*"
Since that study conducted almost 15 years ago up until the present day, there have been several advancements, but the essential framework of the BP process remains unchanged.
Cells can be isolated as fully differentiated tissue cells or manipulated to generate the desired function while being isolated from other tissues. Regenerative medicine has developed precisely with the aim of always identifying new sources of cells, such as stem cells [12]
Therefore, the application of TE to human health care can be seen as a refinement of the principles of medicine through new technologies.
In essence, TE is an engineering solution to a medical issue. However, because of its multidisciplinary character, mechanical engineers, materials scientists, and cell biologists must work together. Producing functional tissues that can sustain or repair damaged tissues and/or organs is the ultimate goal of TE (Fig.1).

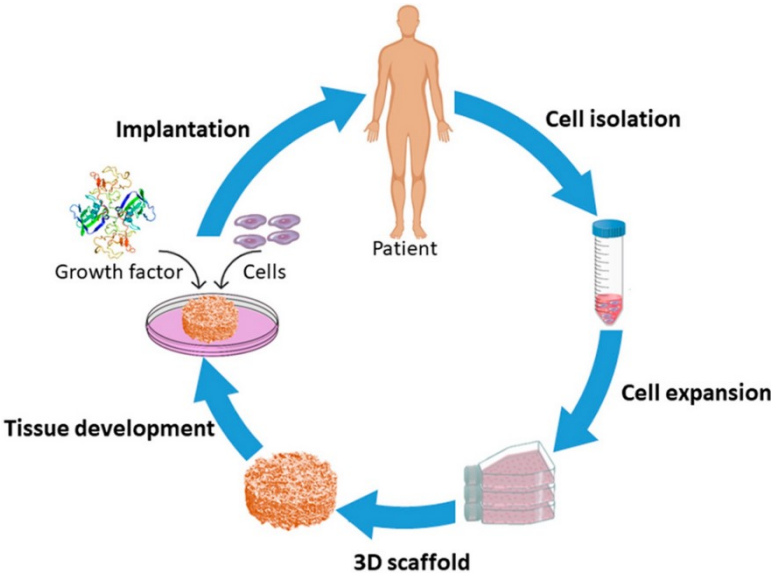

Fig. 1 Schematic diagram of TE purpose [13].

In terms of cell organisation and differentiation, TE generally seeks to recreate specific components of natural tissue development into functional tissues.
Utilising autologous cells in conjunction with growth factors and biodegradable porous scaffolds allows for the precise design and production of implantable structures [14].
The field of TE has advanced significantly over the last 20 years; among the most noteworthy turning points have been the 3D printing of biodegradable scaffolds and scaffolds built of cells and biomaterials using 3D bioprinting. TE scaffolds are all made of biomaterials, which are biocompatible and biodegradable materials [13].
In order to attain the necessary properties, such as mechanical, physical, and biological, in accordance with the particular requirements of the microenvironment, the properties of the

scaffold materials can be further refined and tailored. It is anticipated that microscale 3D techniques, which are presently being researched, would more closely and accurately resemble real tissues. The creation of vascularized tissues with clinically meaningful thicknesses where blood perfusion is produced is another exciting use for TE [15].

The crucial elements include selecting the suitable materials and choose the most appropriate biomanufacturing technique.

The upcoming chapter will examine the methodologies of BP, the materials used in BP, and the advancements in bioink through the incorporation of cells. Finally, it will discuss the fabrication of 3D scaffolds.

Chapter 2

Biomanufacturing techniques

Various manufacturing processes have been employed to produce scaffold structures using biomaterials and live cells. Typically, these procedures may be classified into three categories: traditional, electrospinning, and 3D printing [5,16].
Traditional methods do not based on the fundamental principles of 3D printing or BP. They are referring to the methods used in conventional industries to transform biomaterials into scaffolds with a randomly configuration of pores. As a result, they are significantly less competitive and do not achieve the same level of success in TE applications. These approaches rely on conventional methods of phase separation, melting, and lyophilization [17].
The introduction of AM in the biomedical industry has led to the availability of many biomanufacturing processes, each designed for specific applications and compatible with a range of materials [18].
Below, three biomanufacturing processes will be introduced: electrospinning, 3D BP and laser powder bad fusion.

2.1 Electrospinning

Electrospinning (ES) is a method used to produce extremely thin fibres, ranging in size from the nanoscale scale, by using polymer solutions or melts. This technology originated in the 1930s and has been extensively utilised in the production of TE scaffolds in the last 30 years [19].
A conventional ES configuration has three fundamental elements (Fig.2):

- a syringe containing polymer solution connected to a needle with a flat tip;
- a high voltage generator;
- a collector.

During the process of scaffold fabrication, a high voltage is applied to the polymer solution in the syringe, while the collector is connected to the ground. This creates a strong electric field between the polymer solution and the collector, which leads to a continuous ejection of the polymer solution from the needle syringe. The jet moves in a spiral pattern and then touches down on the collectors, creating a framework with a fibrous structure.
The diameter of spun fibres generally ranges from 200 nm to 5 μm, depending on the process parameters for spinning, such as the applied voltage and the distance between the spinneret and collector [20].

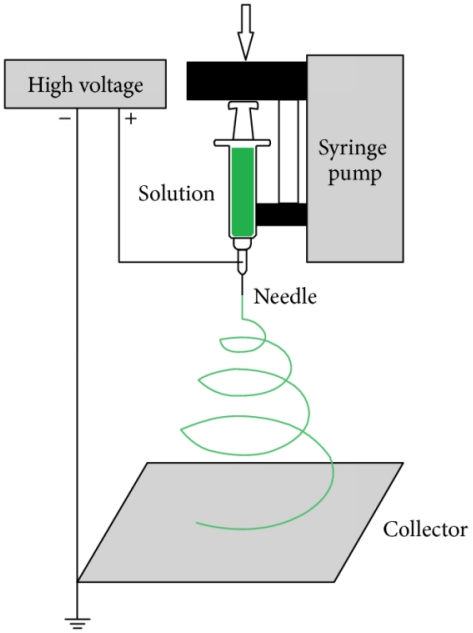

Fig. 2 Schematic diagram of an ES setup [19].

The typically used polymers are divided into two categories: natural polymers and synthetic polymers.
Natural polymers have often been used as scaffolds because of their biocompatibility, bio-functionality and lower cytotoxicity. The most frequently used are silk fibroin, chitosan, collagen, hyaluronic acid, gelatin, chitin and fibrinogen.
Numerous synthetic polymers have been applied to the construction of electrospun scaffolds. The main advantages of synthetic polymers are their spinnability, excellent mechanical integrity and cost-effectiveness. They can also be modified with chemical functional groups that can help the

growth and the proliferation of cells. The most important synthetic polymers are Polycaprolactone (PCL), Polylactic Acid (PLA), Polyglycolic Acid (PGA) and Polyvinyl Alcohol (PVA) [21].
With recent technological advancements, these devices may be engineered to fabricate many types of scaffolds, extending from 2D to 3D structures [22].

For example, with the application of a cylindrical collector, it is possible to create frameworks with a hollow cylinder shape, or, by modifying the syringe and needle you can deliver multiple polymeric solutions simultaneously [23]. For instance, a coaxial needle syringe comprising an inner needle and an outer needle can be employed to dispense two distinct polymeric solutions, resulting in the formation of fibres characterised by a core/shell architecture [24]. Additionally, cells can be included into the ES fluid to create scaffolds that include biological structures. In cases where solvent accumulation or toxicity are a problem, it is possible to use solvent-free polymer ES (via melting), called melt ES, to create scaffold [25].

2.2 3D Bioprinting

The process of fabricating 3D structure for TE applications, through the deposition or patterning of biomaterials layer by layer is referred to as 3D BP of scaffolds.
By depositing biomaterials in multiple layers, 3D printing enables precise control over the architectural characteristics of scaffolds, as opposed to the aforementioned older techniques, which produced unpredictable results. Additional advantages of this method include its simplicity and directness in generating scaffolds with porous architectures, its ability to produce intricate structures that imitate those seen in real tissue or organs, and its capacity to integrate living cells into the scaffold manufacturing process [11].
Regardless of types, BP techniques for TE applications has always the same approach composed of three distinct phases [26]:
Pre-processing: refers to the planning that takes place before production begins. This phase involves the use of devices to acquire the geometry to be reproduced, e.g. Magnetic Resonance Imaging (MRI) or computed tomography to examine the region of interest. Next, a Computer-Aided Design (CAD) model is created to convert the imaging data into a BP design. The planned geometry is converted into a Standard Triangular Language file (STL), which is then subjected to a slicing procedure with specialised software that allows it to be printed immediately.
Processing: encompasses all the phases involved in the creation of 3D scaffold. The segmented geometry file is provided to the printing machine's software, which optimises its parameters to meet the specifications and demands specified by the operator. Defining the optimal printing process and material combination is essential, since each combination affects the interaction between the constituent components and the final production.
Post-processing: it includes all the essential procedures for stabilizing the product, making it acceptable for cell culture or proliferation, capable of stimulating cell growth for tissue formation.

The 3D BP techniques cover a wide range of biological applications with different requirements such as patterning length scale, printing speed, cost and biocompatibility.
Based on the material delivery methods, these printing techniques can be generally classified as contact and non-contact techniques [27]:
contact: the printing technique requires contact between the delivery apparatus and the receiving substrate, such as the extrusion-based methods;
non-contact: the material is delivered to the substrate located very close to the delivery mechanism. Typical examples are: laser-based methods.

2.2.1 Extrusion-Based Bioprinting (EBB)

EBB is a widely used technique in biomanufacturing, particularly in 3D BP, because it enables the processing of soft materials, making it ideal for TE applications. Additionally, it allows the design and fabrication of 3D structures with different sizes and resolution [26].
The basic concept involves the extrusion of uninterrupted strands or fibres of biomaterials, layer by layer, with the purpose of fabricating 3D scaffold structures. Extrusion printing functions by applying mechanical force in three main methods (Fig.3): pressure-assisted material extrusion, piston-assisted material extrusion, and screw-assisted material extrusion, to propel the biomaterial solution contained in a syringe through a needle, and then depositing it onto a printing plate [28].

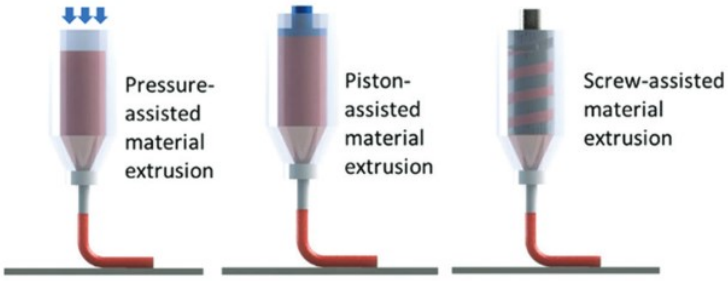

Fig. 3 Schematic illustrations of EBB methods [28].

A standard setup of a 3D extrusion-based bioprinter includes the following components:
- a printing head equipped with a syringe, or cartridge, that holds the biomaterial, with temperature control;
- a needle or nozzle, made of metal or plastic;
- a temperature-controlled printing plate;
- a positioning-control system that allows the printing head to move in the x, y, and z directions.

Printing temperature (for both the head and the plate), printing pressure within the cartridge, and head handling speed are all printing parameters that can be utilised to optimise the process [29].
It is feasible to obtain products with resolutions of 100-200 μm, contingent upon the geometry, the method of slicing, and the diameter of the nozzle. Typical scaffolds fabricated by such systems have 3D structures with repeatable layers of printed strands.
Substrate modification is also possible, contingent upon the desired outcome. For self-standing biomaterials, one may opt for traditional rigid printing plates with temperature control, or alternatively, employ “printing in bath”, in which the printing head operates within the printing medium, called bath, to facilitate cross-linking of the biomaterial, thereby enabling shape fidelity[30].
Hydrogels, which are frequently referred to as bioink when cells are incorporated, are among the materials that can be processed and exhibit the highest level of efficacy in the biomedical field [31].

2.3 Laser Powder Bed Fusion (LPBF)

The LPBF, also known as Selective Laser Melting (SLM), is a widely used metal additive technique. LPBF allows for the efficient production of complex 3D objects using powdered materials, without the requirement of lengthy and costly mould design processes [32].
This feature makes it a suitable technique for 3D printing, specifically for creating scaffolds used in TE applications. Given nowadays conditions, the shapes of objects are consistently tailored to specific requirements, making the traditional approach of fabricating moulds for metal structures impractical from both a financial and technological standpoint [33].
The system basically consists of two mobile platforms: powder feed piston and build piston, a roller and a laser with a scanning mirror (Fig.4).

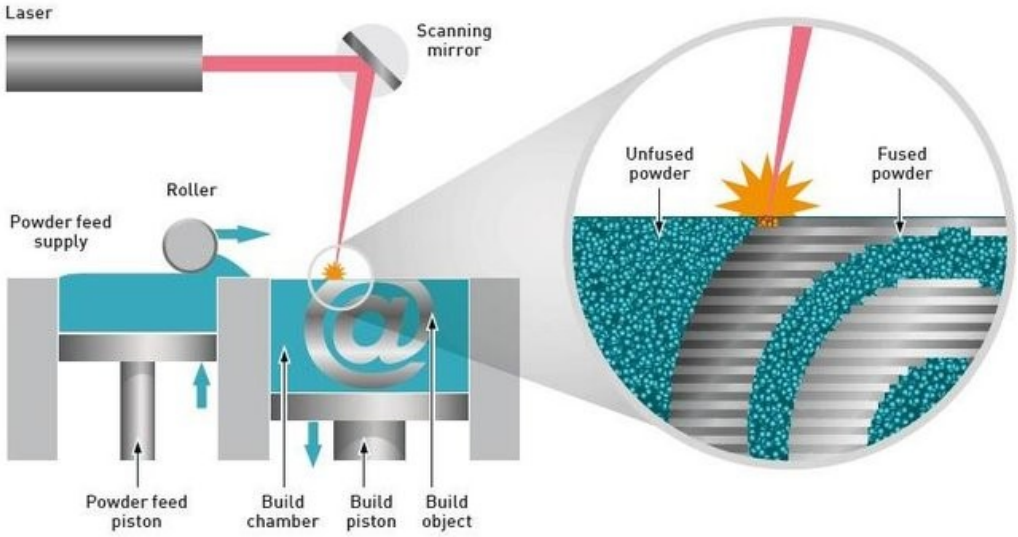

Fig. 4 Schematic of LPBF process [34].

The printing method operates by the roller depositing a thin layer of powder onto the printing platform, either directly or on top of the previously treated layer, within the build chamber. By employing mirror scanning, the high-energy laser strategically elevates the temperature of the metal powder along a preset path, contingent upon the object's shape, resulting in its melting. Currently, the build chamber lowers by a precise amount, likely matching the thickness of the layer, while the powder feed piston rises, and the roller refills the thin coating of metal powder. The method is repeated until the desired 3D scaffold is created.
After the printing process is complete, any surplus powder is eliminated, and the component is physically separated from the printing platform. In order to inhibit the oxidation of the components during the printing process, the build chamber is filled with inert gases such as Argon or Nitrogen [34,35].
The approach results in improved characteristics in components compared to those produced by conventional procedures, due to the ultrafine and graded microstructure that arises from the quick cooling and solidification cycles. Parameters related to printing, such as the scanning pattern, laser power, scanning speed, layer thickness, build orientation, and plate temperature, are commonly modified to produce parts with specific desired properties. These properties include

the quality of the surface, the level of porosity, the accuracy of dimensions, the type of microstructures (such as columnar or equiaxed grain), and various properties such as mechanical strength, hardness, resistance to corrosion, resistance to oxidation and biocompatibility [36,37].
LPBF technology can process a wide range of materials. Titanium alloys and Steel alloys are the most commonly utilised materials, while Cobalt-Chromium alloys, Aluminium alloys, and Magnesium alloys are all gaining increasing attention in research [38].

Chapter 3

Biomaterials

Biomaterials are inert substances commonly employed in therapeutic and diagnostic applications that come in contact with tissue or biological fluids.
Biomaterials can be classified as polymers (both natural and synthetic), ceramics, metals (alloys), glasses, carbons, and composites consisting of different combinations of these materials [39].
Biomaterials have been created to serve as substitutes for biological materials, fulfilling their functions. Due to their exceptional material qualities, biomaterials are extensively utilised in the production of various medical devices, pharmaceutical preparations, and diagnostic products for medical and healthcare purposes [10].
In order to be suitable for usage in intracorporeal environments, biomaterials must possess the following characteristics:

- non-toxic and non-carcinogenic;
- chemically stable and resistant to corrosion, capable of withstanding significant and fluctuating stresses within the human body;
- capable of being shaped or fabricated into complex and intricate geometries.

Subsequently, the prevailing materials utilised in the previously mentioned biomanufacturing techniques will be presented.

3.1 Bioinks

The term "bioink" was initially employed in the field of organ printing in 2003[40]. Originally, the idea was to print a hydrogel, a water-swollen cross-linked polymeric network, and subsequently introduce living cells or tissue spheroids as "bioink" by BP. Hence, the word "bioink" first denoted the biological constituent that was inserted within a hydrogel, either on its surface or within its 3D structure [41].
Hydrogels are commonly employed biomaterials in BP due to their ability to mimic characteristics of the natural Extra Cellular Matrix (ECM) and allow the encapsulation of cells in a hydrated and mechanically robust 3D setting [31].
In recent years, the advancement of 3D printing technologies, particularly the EBB, has posed a significant challenge: ensuring the stability of the 3D printed object once it has been deposited. Thus, the substance must promptly elevate its viscosity following the printing process, a phenomenon commonly achieved through subsequent cross-linking. Consequently, the requirement for a separate hydrogel became obsolete, leading to the attainment of a unified concept of bioink as a composite material comprising hydrogels and cells in the EBB (Fig. 5) [41].

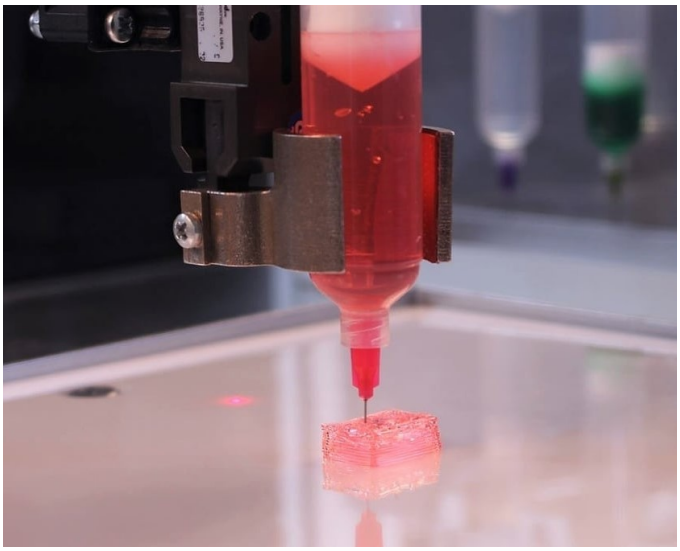

Fig. 5 Bioink in a syringe during the EBB process.
Source: Ricardo Pires, What Exactly is Bioink?, all3dp.

Bioinks can be divided into two major classes based on their source, i.e., naturally derived or synthetic. Most hydrogels used for formulating bioinks are derived from natural ECM sources, such as collagen, gelatin, fibrin, hyaluronic acid, alginate, and agarose. These naturally derived polymers have intrinsic capabilities to support cell viability and proliferation and can be relatively easy degraded or metabolized. Nevertheless, natural biomaterials have several limitations such as rejection and/or immune-related complications, rapid degradation rates, and inadequate mechanical characteristics.
Synthetic hydrogels typically exhibit biological inertness and non-biodegradability, although they can be altered to address the drawbacks associated with natural hydrogels.

Bioinks can be cross-linked or gelled under suitable conditions to form a structurally stable polymeric network, as previously mentioned. In addition, during the process of EBB, various cross-linking strategies can be applied, not only when printing is completed but also during filament deposition [31,42].
The following section describes the natural or synthetic bioinks investigated in this research.

3.1.1 Alginate

Alginate is the term used to refer to the salts of alginic acid. Sometimes it refers also to all the derivatives of the alginic acid or the alginic acid itself. Sodium alginate (SA) is the salt that is usually of interest in bioengineering [31]. It is generally extracted from brown seaweed. Indeed, calcium, magnesium, and sodium salts of alginic acid are present in the cell walls of the brown algae. The first two are not soluble in water, while the sodium salt is.
It is commonly used for many biomedical applications due to its low toxicity, its biocompatibility, and the fact that it easily cross-links in the presence of divalent cations, as Ca^{++} [43].
It is typically extracted from brown seaweed (*Phaeophycean*) as *Laminaria digitate, Laminaria japonica, Laminaria hyperborean, Macrocystis pyrifera and Ascophyllum nodosum* that are torn into little pieces and stirred with a hot alkaline solution, usually with Sodium Hydroxide (NaOH). After a couple of hours, the alginate dissolves in water as SA in a very thick slurry. The compound is also very thick due to the residual seaweed not dissolved (mainly cellulose). The solution is highly diluted with water in order to be filtered easily and eliminate the waste.
After filtering, the precipitation of alginate can be obtained with two different methods called alginic acid process or calcium alginate process [44].
The first method adds acid in the filtered extract. This forms soft gelatinous pieces of alginic acid that need then to be separated from water. The water content into the pieces is very high (98-99%) and need to be reduced usually through screw press or centrifuges. Then an alcohol is added (ethanol or isopropanol) to reach a 50:50 mixture of alcohol and water. At this point, sodium carbonate is gradually added until the paste reaches the desired pH.
The calcium alginate process instead uses a soluble calcium salt (as $CaCl_2$) that is added to the filtered extract. The calcium alginate starts forming and depending on the care in mixing, the calcium alginate can be obtained in fibres or in gelatinous solid, if bad mixing occurs. The fibrous material is then placed on a metal screen and washed to eliminate the excess of calcium. After the compound is diluted in acid, it is stirred to obtain alginic acid with fibrous characteristics of calcium alginate. The formed alginic acid is then squeezed in a screw press. Sodium carbonate is finally added to convert the paste in sodium alginate, reaching the desired pH level. In both cases, the final paste can be then dried and milled to obtain SA pellets or powder [45].

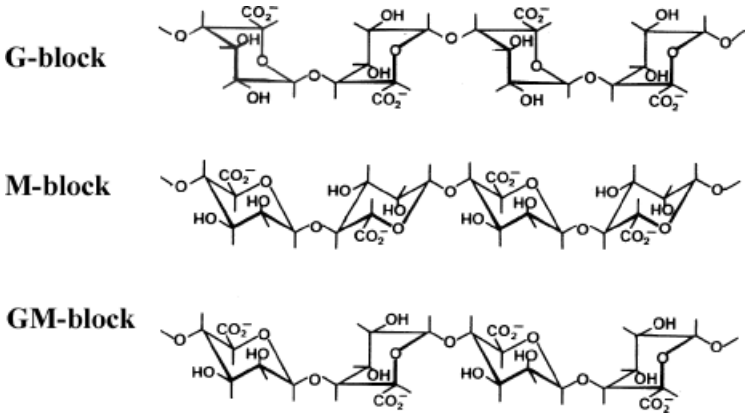

Fig. 6 Chemical structures of the various blocks in the SA [46]**.**

Alginates comprehend a whole family of copolymers containing blocks of (1,4)-linked β-D-mannuronate (M) and α-L-guluronate (G) residues. The blocks are composed of consecutive M residues (MMMMMM), consecutive G residues (GGGGGG), and alternating M and G residues (GMGMGM) [46,47] (Fig.6). There are more than 200 type of alginate that are available in commerce that difference in the presence in percentage of M or G residues and in the length of the blocks due to the sources of extraction [48]. In particular, the G-blocks are believed to participate into the cross-linking process with the divalent cation.
The molecular weight of commercial SA is in a range between 32,000 and 400,000 Da.
SA is soluble in water with which forms a colloidal solution. It is insoluble in alcohol and hydro-alcoholic solution in which the alcohol content is greater than the 30%.
The viscosity has a wide variability depending on the concentration and nature. In a solution 1% at 20°C the range is 0.02-0.4 Pa·s. It behaves as pseudoplastic fluid and so it is non-Newtonian, due to the chains length. The viscosity strongly increases in the presence of a strong electrolyte such as sodium chloride (NaCl) due to a change in polymer conformation [49].

3.1.2 Gelatin

Gelatin is a high molecular weight polypeptide derived from partial hydrolysis of collagen, the primary protein component of animal connective tissues, which include tendons, skin, and bones. The name comes from the Latin word “gelatus” that means frozen or firm.
It is produced from biological materials, whose variety influences the outcome product. It is available in commerce in two types: type A and type B. They differ in the manufacturing process, isoelectric point, and viscosity [50,51].
Gelatin swells when placed in cold water, absorbing 5 to 10 times its own volume of water. When heated to temperatures above the melting point (sol-gel temperature), the swollen gelatin dissolves and forms a gel when cooled; this conversion is reversible and can be repeated. The gel starts to melt between 27°C and 37°C; this property is highly desirable in food industry but can be critical for mechanical properties in biomechanical application due to our body average temperature that is 37°C. Gelatin is also composed of collagen bioactive sequences that are recognized by cell receptors and can interact with them, promoting cellular adhesion [52].

The manufacturing process transforms the highly organized fibres of collagen (that are insoluble in water) to a less polymerised system, gelatin, which is soluble in water.

It starts with the animal's parts, hides, and bones that are chopped into small pieces. Usually, the main source are pigs, even if collagen is present in every connective tissue of any animal. The raw materials are then disintegrated in acid or alkaline solution such as caustic lime or sodium carbonate respectively. The gelatin produced through acid treatment is called Type-A, through alkaline treatment is called Type-B. The compost is then washed in water and boiled until it becomes a gel. Then it is filtered, evaporated, and dried to separate the water from the gelatin solution. The source of raw material, the different method used (alkaline or acid) and the care during the manufacturing are some of the causes of huge variability in the outcome of gelatin.
Commercially, gelatin is available in desiccated powders, paper-thin sheet or meltable blocks. The 95% of produced gelatin is used in food industry, pharmaceuticals, photography, and cosmetics [53].

Gelatin is a compound of polypeptide chains held together by hydrogens bonds between the amino acids of adjacent chains. The mutual arrangement of the polypeptide chains is called secondary structure of a protein. Gelatin comes from the collagen, which has as secondary structure, three polypeptide chains well organized in a triple-helix conformation. Then in collagen, the triple helical molecules are further organized in fibres. This gave its structural mechanical properties that reflects the mechanical behaviour of the starting biological tissues.
Through the heating process the secondary structure partially loses order, and thus the collagen goes into denaturation. Gelatin is indeed denatured collagen (Fig. 7).

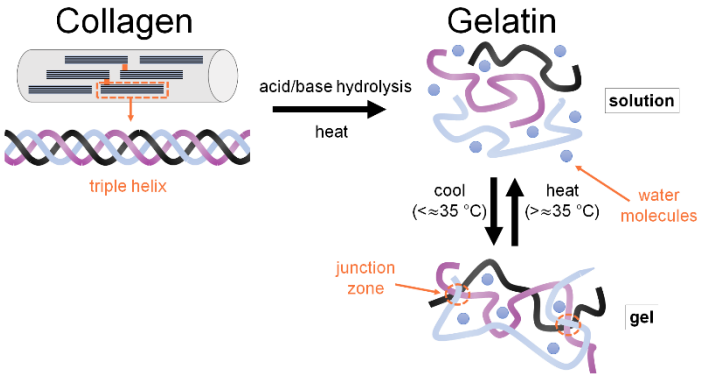

Fig. 7 Denaturation of collagen and thermoreversible process occurring in gelatine.
Source: Katie Fegan, Gelatine, ChemBAM.

To help the hydrolysis process, because collagen is insoluble in water, acid or basic condition are used as catalysts.
At approximately 35°C, the gelatin has its sol-gel transition point. When cooled below this point, the secondary structure is partially reformed, and the mechanical properties increase.
Some parts of the structure are able to reform an ordered triple-helix conformation, and they are called junction zones; other parts reform in a random disposition of chains and they are called amorphous zones. The secondary structure obtained when gelatin is cooled below the sol-gel point is however only partially similar to the collagen one.
The ability of gelatin to form a hydrogel is given from the junction zones. Indeed, with water, gelatin form a colloidal solution, where one phase is microscopically mixed within another phase.

The network made from triple-helix disposition of chain act as a cross linker and traps the water drops.
Pure dried gelatin is transparent, odourless, tasteless, brittle and glass-like solid, with a colour that vary from a pale yellow to amber depending on the clarification undergone.
The molecular weight is around 40,000 to 90,000 Da. The isoelectric point varies from type A to type B. The first usually falls between 7 to 9, while for the second typically falls between 4.8 and 5.1.
The viscosity of gelatin, in the order of mPa·s, varies significantly with the concentration, type, temperature, and time used. In general, type A gelatin has a little viscosity than type B, but no difference in the sol-gel point is found between the two.
The melting point is affected by maturing time, concentration (increases with increasing concentration), and salt presence (for instance, sodium chloride depresses the melting point) [54,55].

3.1.3 Poly(vinyl alcohol) (PVA)

PVA is obtained from the hydrolysis of poly(vinyl acetate) (Fig. 8). PVA can be transformed into a gel state by cross-linking it using either chemical or physical techniques. Additionally, it can undergo photo-curing to produce hydrogels [43].

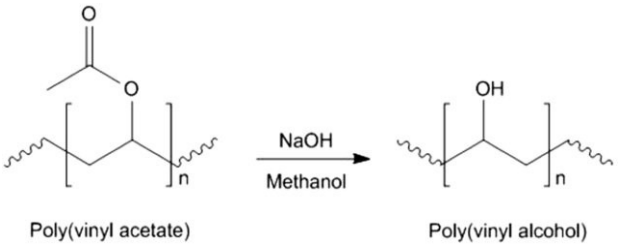

Fig. 8 Hydrolysis of poly(vinyl acetate) to obtain poly(vinyl alcohol) [56].

PVA hydrogels are neutral and non-adhesive to proteins and cells. Their friction coefficient is low and their structural features closely resemble those of genuine cartilage. Moreover, they exhibit greater strength compared to the majority of other artificial gels, rendering them effective for avascular tissue [50].
Moreover, PVA has the ability to undergo copolymerization with other polymers, resulting in the creation of a biodegradable hydrogel that may be adjusted to degrade at a desired rate.
Applications in TE are restricted due to the fact that PVA is a non-biodegradable polymer in physiological environments and does not promote cell adhesion by nature. Furthermore, the utilisation of hydrogen bonding as a cross-linking strategy in PVA introduces complexity into the process of chemical modification, which can be avoided with alternative polymers [51].
PVA hydrogels are produced using a combination of physical and chemical cross-linking methods, resulting in hydrogels that possess exceptional strength and toughness. Optimal mechanical qualities can be attained using a combination of room temperature reaction, freeze-thaw cycles, and annealing treatment. Furthermore, the mechanical characteristics of PVA hydrogel exhibited an initial increase followed by a subsequent drop when the molecular weight or mass fraction rose. The mechanical characteristics of PVA hydrogel can be efficiently modified by altering the reaction solvent. Therefore, the influences of various factors on the mechanical properties of PVA hydrogel can be obtained [43].

3.2 Bioinks properties

The success of bioprinted scaffold and its subsequent uses depends on the characteristics of the bioinks used, such as their ability to be printed, ability to create cross-links, biological qualities, and mechanical properties. The ability to be printed and the capacity to form cross-links are key factors in determining whether the bioinks can be used to create 3D structures. Meanwhile, the biological and mechanical qualities of the bioprinted constructs are intimately linked to their later applications [31].

3.2.1 Printability

Printability is a term that is used in the context of 3D EBB to describe the capacity of a bioink to produce and sustain a 3D structure. During the BP procedure, the bioink is initially applied onto a printing surface or supporting stage, and subsequently solidifies into a 3D structure via cross-linking or gelation. Additionally, the bioink is in a fluid or semifluid state during the printing process and is able to flow or extruded on the supporting stage. This occurs before the gelation process begins. Consequently, the physical form of a scaffold does not match the intended design, as seen in Fig. 9.

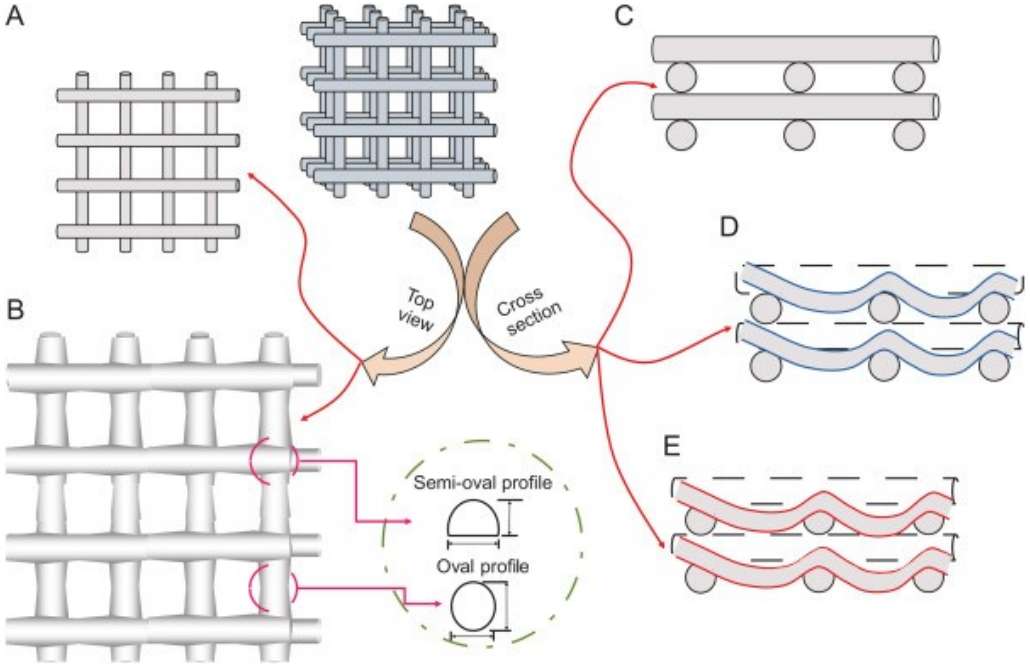

Fig. 9 Difference between the scaffold design and printed structure: top views with (A) design grid and (B) printed grid where strand have disomugeneus diameter; and cross section with (C) no overlap among layers and no deflection, (D) no overlap and deflection, and (E) overlap and deflection [57].

It is possible that the printed structure would collapse and fail to create a 3D structure in certain circumstances, both deflection and overlapping of the single filament might occur. As a consequence, the 3D structure is not completely freestanding and a bioink that behaves in this manner would be considered unprintable. Currently, there is a lack of established methodologies to accurately measure printability. However, it is usual to compare the scaffold design and printed structures based on the thickness of the strands and the size of the pores. The printability of a

bioink can be influenced by the initial layer formed on the printing stage and its physical features, including contact angle, flow behaviour, and cross-linking processes [9,58].

The first layer of printed hydrogel plays an important role in the printing process. Fig. 10 shows two strands that have been created with varying contact angles, which refers to the angle between the printed strand's profile and the surface it is printed on. A high contact angle preserves the accuracy of the printed hydrogel structure in the vertical direction, while a low contact angle secures the printed construct on the receiving surface and prevents random movements and potential distortion during the layer-by-layer hydrogel printing process. Printing hydrogel onto surfaces like glass or plastic (i.e. Petri dish) is challenging because to their high contact angles, which hinder the establishment of suitable interactions. To address this issue, hydrophobic fluids can be employed. However, if these fluids are not appropriate for biomedical purposes, an alternative approach is to manage the printing substrate by adjusting the temperature. This will enable the bioink to harden upon contact and achieve a desirable contact angle [59–61].

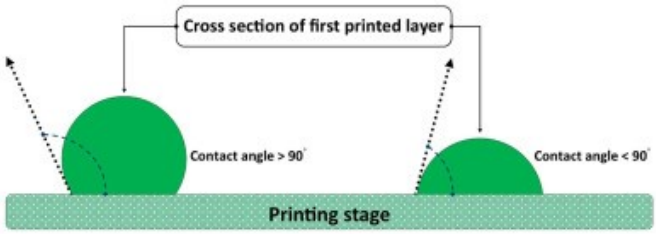

Fig. 10 Cross section of first printed layer and relative contact angle [60].

The rheological properties of a biomaterial solution are determined by its viscosity and are defined by the correlation between the applied force and the rate of deformation inside the solution. Viscosity, which is the relationship between shear stress and shear rate, is commonly used to quantify flow behaviour. The rheological properties of a bioink have a substantial impact on its capacity to be printed. Greater viscosity of the bioink solution directly correlates with improved printability. This phenomenon occurs because a bioink with higher viscosity, after it is printed, has less flowability and spreading ability, making it simpler to keep its original cylindrical shape. In contrast, encapsulated cells have a higher likelihood of survival in bioink solutions with lower viscosity, since it allows for more activity and mobility.
Moreover, bioinks with greater viscosity necessitate elevated pressures for the process of BP. Consequently, the cells in the bioink are subjected to significant stresses generated throughout the process, such as shear forces, which have a detrimental impact on cell survival and function [59,60,62].

3.2.2 Cross-linking

A crucial stage in the BP procedure is the transition of a solution capable of producing hydrogels into a solidified or interconnected hydrogel structure.
The cross-linking process can occur through either physical means, such as a reversible gelation process, or chemical means, including covalent chemical bonds, or a mix of both.
BP usually employs physical cross-linking processes such as ionic, thermal, and photo-cross-linking [63].

Ionic cross-linking is a form of physical cross-linking that takes place when a water-soluble and charged polymer forms cross-links with an ion that has an opposing charge. Alginate is a widely recognised polymer that may undergo cross-linking by the use of divalent metal ions, such as Ca^{++} or Zn^{++}. Ionic cross-linking plays a crucial role in BP by facilitating gentle and immediate gelation of hydrogel. The presence of Ca^{++} ions (or other divalent or trivalent cations) induces fast gelation of alginate solution. Due of the rapid occurrence of cross-linking in alginate gels under normal physiological settings, they have been extensively investigated for their potential use in BP for TE purposes [64]. The $CaCl_2$ concentration in the aerosol solution can be altered to modify the cross-linking conditions of alginate hydrogels during BP. This can be achieved through either aerosol spraying or printing in the bath using the Freeform Reversible Embedding of Suspended Hydrogels (FRESH) method (Fig. 11) [65]. However, it is particularly challenging to apply this method in TE applications involving soft tissue. Further investigation into this method will be presented subsequently.

It is crucial to acknowledge that a structure constructed using hydrogels that are not appropriately cross-linked may experience shape deformation and potentially experience structural collapse [64,66].

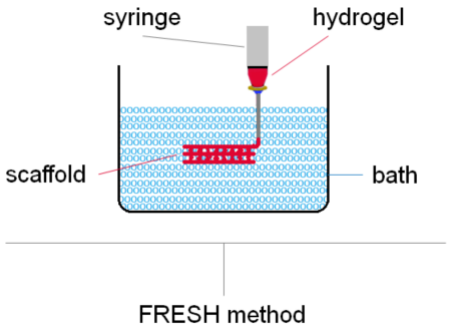

Fig. 11 FRESH bath in BP process scheme.

Thermal crosslinkable polymers exhibit temperature sensitivity, wherein changes in temperature can induce cross-linking or gelation. Polymers that undergo heat cross-linking, like gelatin and collagen, typically have a gel transition temperature at which the solution becomes a gel. These polymers undergo dissolution when exposed to heat, and their solutions may be applied onto a cooling stage. At this step, the polymer undergoes a gel transition and solidifies. Nevertheless, gels produced by thermal cross-linking often exhibit low strength and inadequate mechanical reinforcement [54,55].

When utilised as bioinks for BP, it is necessary to consider various prerequisites:

- the melting temperature and gelation temperature must be in line with the requirements of the embedded cells;
- the temperature decrease before and after printing must be appropriate.

Minor decreases in temperature can result in increased viscosity, potentially impacting the survival of cells embedded within the material.

Conversely, significant temperature drops will prolong the gelation process, affecting the accuracy of the printed structure in achieving the desired shape [66].

Photo-cross-linking is the process by which a covalent connection is formed between macromolecules using photoinduction, resulting in the construction of a cross-linked network. Photocurable polymers may be printed on an illuminated stage and undergo a chemical reaction to generate hydrogels. Polymers like collagen, fibrin, and gelatin can undergo direct photo-cross-linking when a suitable photoinitiator is added [67]. While the majority of polymers do not possess the ability to undergo direct cross-linking by light exposure, they can be rendered photo-cross-linkable through a chemical process involving an acrylate or methacrylate-based agent. Typically, these polymers undergo cross-linking by exposure to ultraviolet (UV) radiation. The use of gelatin-methacrylate, hyaluronan-methacrylate, and dextran-methacrylate has been documented for the purpose of photocross-linking polymer BP [68].

3.2.3 Biocompatibility

One crucial distinction between BP and standard scaffold manufacturing techniques is the inclusion of live cells in the creation process. The procedure involves combining living cells with a solution of hydrogel-forming polymer to create bioink, which is subsequently used in the BP process. Prior to employing any material for BP, it is essential to take into account its biocompatibility.

Biocompatibility refers to the capacity of a substance to induce an adequate reaction from the host organism in a certain context [69].

The biocompatibility of a material can be defined by three key factors:

- its ability to maintain the structure and function of cells and tissues it directly interacts with, known as cytocompatibility;
- the cytocompatibility of the degradation products it produces;
- its ability to avoid triggering any immune rejection response when implanted in living organisms.

Due to the emergence of TE, the concept of biocompatibility has expanded to encompass active engagement with natural tissues and/or the immune system, as well as the facilitation of suitable biological functions. In this framework, the assessment of hydrogel biocompatibility should encompass the entire process, starting with the BP and in vitro maturation stage (cytocompatibility), continuing through implantation (immunogenicity), and considering the long-term consequences (degradation byproducts) [31].

Throughout the procedure, cells are subjected to process-induced stressors, such as shear stress, which may potentially result in cell injury. Consequently, only a fraction of the cells in the bioink are able to survive the BP process. Cell viability is the measure of the proportion of living cells compared to the total number of cells present. A commonly employed method for assessing cell viability is the live/dead experiment. The cell viability of EBB ranges from 40 to 98% [70]. The hydrogel composition becomes crucial in promoting cell survival and proliferation once bioinks have been placed. Certain polymers obtained from natural sources contain peptide sequences that promote cell adhesion. These peptides provide a conducive milieu that enhances the survival and growth of cells, surpassing the benefits offered by synthetic polymers. Consequently, several endeavours have been undertaken to enhance synthetic hydrogels by including cell-adhesive sequences, aiming to improve cell survival, proliferation, and differentiation [60,69].

3.2.4 Mechanical properties

The mechanical characteristics of bioinks are crucial in TE applications. The printability and the resulting scaffold structure are significantly influenced by the mechanical characteristics of the biomaterial. The structures created using bioinks are usually placed in bioreactors for maturation in a laboratory setting (in vitro). They are then implanted into living organisms (in vivo), where they offer cells a 3D framework and mechanical assistance for cellular activities like migration, proliferation, and differentiation. This leads to the development of a functional TE structure or viable tissue [7].

The mechanical characteristics of bioinks or printed constructions are characterised by their strength and deterioration and are defined by the correlation between the exerted force and the subsequent deformation. The mechanical characteristics of constructions are subject to change, as biomaterial strength decreases owing to degradation and is counteracted by an increase in mechanical strength resulting from tissue regeneration [11].

Ultimately, the construct should possess mechanical qualities that closely resemble those of the tissue or organ being restored throughout the process of regeneration. It is well acknowledged that the mechanical characteristics of a structure at the beginning of implantation or of a composite structure made of scaffold biomaterials and regenerated tissue during the healing process should closely resemble those of the tissue or organ being repaired. The mechanical strength of a biomaterial must be enough to ensure the structural integrity of printed scaffolds throughout and after the construction process. This strength is necessary to offer the necessary mechanical support for cell development and tissue regeneration [60,62].

There are several ways available to enhance the mechanical characteristics of biomaterials. One effective approach involves incorporating additives or microparticles into the bioink. This method can increase the strength of the biomaterial without significantly affecting its printability and its biocompatibility [59].

3.2 Additives

Although hydrogels have been widely accepted as biomaterials used in BP due to their biocompatibility, their weak mechanical strength has limited further applications. A successful approach is the addition of substances known as additives, which are commonly incorporated to improve mechanical properties and shape fidelity at the same time.
The additives commonly employed consist of synthetic or inert substances, however, their rates of degradation and cytotoxic impacts can be regulated by manipulating the quantities during the formulation process. Furthermore, aside from improving mechanical qualities, the inclusion of growth agents or specific biomolecules can also boost biological properties. Thus, the use of additives also increases cell adhesion and proliferation on the scaffolds [71].

3.2.1 Carbon-based

Carbon-based materials can be incorporated in hydrogels to create conductive hydrogels. Carbon-based materials possess several advantages, such as excellent biocompatibility, a wide variety of physical and chemical properties, high surface area and conductivity [72].
Recently, graphene and its derivatives, such as graphene oxide (GO) and reduced graphene oxide (rGO), have emerged as a new class of nanomaterials that could be implemented for several biomedical applications, including drug delivery, cell imaging, and as tissue scaffolds (Fig. 12) [73,74].

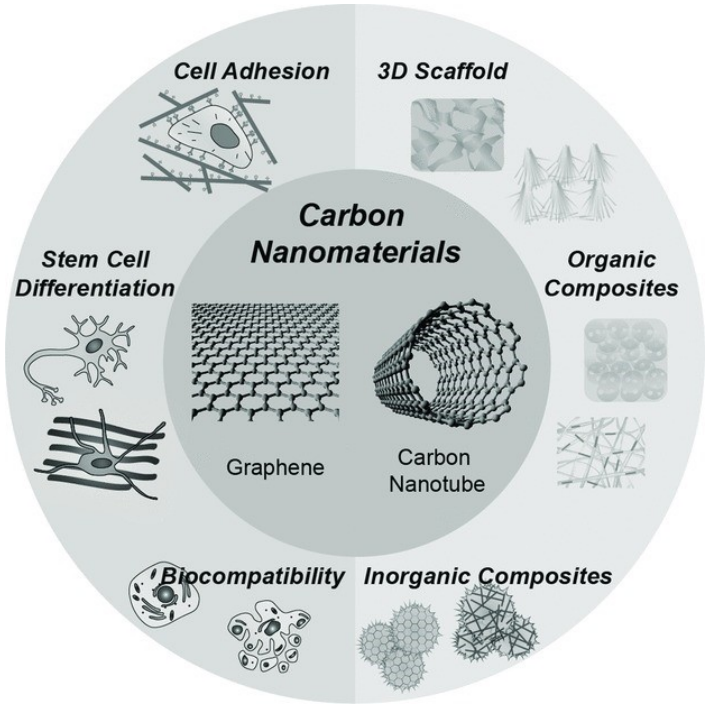

Fig. 12 Carbon-based materials for TE applications [74].

In the last decade, graphene (Fig. 12), a single-layer carbon allotrope with a two-dimensional honeycomb lattice atomic arrangement, has become one of the most effective conductive fillers for advanced TE applications due to its outstanding mechanical properties, tunable electrical

conductivity, and good biocompatibility. To fabricate graphene-based composite hydrogels for biomedical application, carbon allotropes are commonly dispersed in biocompatible and biodegradable polymers [75].

GO can be derived by the chemical oxidation and exfoliation of graphite. The oxygenated surface functionalities in the GO nanosheets give it the potential to react with many polymers.
Graphene and graphene oxide sheets are both soft membranes with high in-plane stiffness, which can potentially serve as a biocompatible, transferable, and implantable platforms for stem cell cultures. While the healthy proliferation of stem cells on various carbon platforms has been demonstrated, the chemical role of G and GO, if any, in guiding uncommitted stem cells toward differentiated cells is still unknown. The molecular origin of accelerated differentiation is investigated by studying the binding abilities of G and GO toward different growth agents. Epoxide, carboxyl, and hydroxyl groups present on the basal plane and edges of GO enable greater interactions with proteins through covalent, electrostatic, and hydrogen bonding. Recently, the ability of Chemical Vapour Deposition-grown G of promoting the adhesion and proliferation of Mesenchymal stem cells and osteoblasts has been demonstrated.
GO is commonly used in biomedical applications because of its unique chemical properties, such as high biocompatibility, low toxicity, a large surface area for effective drug binding, oxygen-containing functionalities, and improved conductivity. It also has suitable mechanical properties for cell attachment. Studies showed that scaffolds containing GO can promote cell adhesion and proliferation [76].
This material also has a long history of use as a precursor to chemically converted graphene. Many hydrophilic oxygenated functional groups in GO—such as hydroxyl (–OH), epoxy (–C–O–C–) and carboxyl (–COOH)—enable it to disperse in water solutions and to be easily exfoliated into monolayer sheets. Due to these functional classes, GO is amphiphilic, with hydrophilic edges and hydrophobic basal planes. GO contains oxygen-enriched functional groups, which react with various polymers to form polymer-based graphene oxide nanocomposites. The large surface area of GO is used to carry and distribute drugs through contact between GO functionalities and drug groups [77].

Conventional fabrication methods used for generating rGO require high- or low-pH solutions, high temperature (> 90°C), and toxic reductants like hydrazine, which are not compatible with cell studies.
One potential concern is the cellular toxicity of these materials after the hydrogel matrix has degraded. It has been shown that the cytotoxicity of these nanoparticles depends on their shape and composition. For example, two-dimensional (2D) graphene exhibits lower cytotoxicity as compared to one-dimensional (1D) carbon nanotubes. GO is usually preferred over graphene for producing homogeneous aqueous suspensions due to the oxygen-containing groups on its basal plane (hydroxyl and epoxide groups) and edges (carboxyl groups), which make the GO sheets very hydrophilic. However, GO exhibits relatively low electrical conductivity compared to graphene sheets. In addition, the cellular behaviour on the reduced version of materials based on GO (i.e., rGO) can be regulated by tuning the surface oxygen content of rGO. Specifically, it has been shown that cell adhesion and proliferation are enhanced on partially reduced GO, which may be induced by enhanced adsorption of ECM proteins on rGO surface by non-covalent interactions. Therefore, rGO is a promising material for cardiac TE applications [78].

3.2.2 Cellulose-based

Cellulose derivates are obtained from cellulose modification through mainly two methods: physical and chemical modification [79].
Physical modification goal is to obtain new properties and function by changing the surface and structure properties of cellulose without changing the chemical composition. Indeed, mechanical grinding, swelling, recombining and surface absorption are used to reach new properties. Derivates by these methods are regenerated cellulose, spherical cellulose, nanocellulose (NC), microcrystalline cellulose and membrane cellulose. NC are the one of more interest and widely used in biomedical field due to their biodegradability, non-toxic biocompatibility, wound-healing characteristic, antibacterial effect. Are mainly classified in cellulose nanofibers (CNF) and cellulose nanocrystals (CNC).
Chemical modification is divided in two types of reaction: degradation of cellulose and derivatization of hydroxyl groups. The degradation methods are then further classified as acid/base degradation, biodegradation, mechanical processing degradation and oxidative degradation. The derivatization is instead the most common process to synthetize derivates of cellulose. Of great interest and commonly used are cellulose ester, cellulose ether, and cellulose nitrate (celluloid).
Cellulose esters are for instance cellulose xanthate, cellulose acetate, cellulose acetate phthalate (CAP) hydroxypropyl methyl cellulose phthalate (HPMCP). These are synthesized by esterification of hydroxyl groups with different organic acids in presence of a strong acid as catalyst.
Cellulose ethers are obtained substituting a hydroxyl group by a hydrocarbon group. Of great interest among cellulose ethers are methyl cellulose (MC), HPMCP, hydroxyethyl cellulose (HEC), carboxymethyl cellulose (CMC) and micro-fibrillated cellulose (mFC). Compared with cellulose, cellulose ether has an excellent water-solubility and thermoplasticity, properties of great interest in the preparation of hydrogels [80,81].

CMC is an ether water-soluble anionic derivative of cellulose. The main differences with cellulose are anionic carboxymethyl groups -CH2COOH that replace some hydrogens in some hydroxyl groups [82,83].
The use of CMC and CMC derivatives is wide in biomedical, oil, paper, cosmetics, construction food, textile, and pharmaceutical industries. In the biomedical field is used in TE [84,85]bone-TE [86], wound dressing [87] and fabrication of biocompatible 3D scaffold.

mFC is composed of expanded high-volume cellulose, moderately degraded and greatly expanded in surface area, and obtained by a homogenization process. mFC actually consists of aggregates of cellulose microfibrils. Its diameter is in the range 20–60 nm and it has a length of several micrometers. mFC exhibits both amorphous and crystalline parts and presents a web-like structure, thus has a very good ability to form a rigid network. It is obtained by the mechanical disintegration of cellulosic materials without the use of hydrolysis[81].

Among the cellulose derivatives, its suspension, thickening, binding, and emulsifying properties makes CMC and mFC more used respect the others. These properties moreover are useful in pharmaceutical and food industries [79].

CMC and mFC in BP are used as thickener for bio-ink due to its compatibility as blender, slow degradability biocompatibility, mechanical properties and surface properties that support cell aggregation, differentiation, and protein adsorption. These additives are moreover interesting as viscosity modifier with a shear thinning behaviour [82].

3.3 Solvent

To prepare a bioink for BP purposes, the choice of the solvent in which suspend the solutes, reflects the final application. Depending on the type of cells embedded in the bioink, a specific of more suitable solvent may be used not to affect the cellular viability.
As major solvents selected in this study there are: pure water, Phosphate Buffered Saline (PBS) and Iscove's Modified Dulbecco's Medium (IMDM) [88,89].
Pure water used in the biology laboratories is usually the MilliQ one, also known as ultra-purified water (UPW). It means that the water is purified using a Millipore MilliQ lab system. It is filtered through membrane filter with a dimension around 0.22 μm. It is used in semiconductor industries and biology laboratories due to its high purity from particle, bacteria, and contaminant. Specific standards give references per each field of application (e.g., in semiconductor ASTM D5127-13(2018)).
PBS is a buffer solution with a pH around 7.4 used in biology researches. It is a water-based salt solution containing sodium chloride NaCl, disodium hydrogen phosphate Na2HPO4 and in some formulation also potassium dihydrogen phosphate KH2PO4 and potassium chloride KCl. The purpose of the buffer is to maintain the pH constant and indeed it is used because its ion concentration and osmolarity matches the ones of the human body.
IMDM is a modification of Dulbecco's Modified Eagle's Medium (DMEM) which is itself a modification of the Minimal Essential Medium (MEM). The MEM is a synthetic cell cultural medium based on glucose, 6 salts (potassium chloride KCl, calcium chloride $CaCl_2$, sodium chloride NaCl, magnesium sulphate MgSO4, sodium phosphate NaPO4, sodium bicarbonate NaHCO3), 13 essential amino acids and 8 vitamins ((thiamine (vitamin B1), riboflavin (vitamin B2), nicotinamide (vitamin B3), pantothenic acid (vitamin B5), pyrodoxine (vitamin B6), folic acid (vitamin B9), choline, and myo-inositol (vitamin B8)).

The DMEM differs from MEM by the concentration of the components while IMDM contains selenium, additional amino acids and vitamins, sodium pyruvate, HEPES (4-(2-hydroxyethyl)-1-piperazineethanesulfonic acid) buffer, and potassium nitrate instead of ferric nitrate. All are cultural medium used to maintain cell in tissue culture. PBS, IMDM and DMEM are usually bought by the laboratories from companies that following the protocols prepare the solutions ready to use and reliable [90,91].

3.5 Metal alloys

Orthopaedic implants are the most prevalent biomedical application of metal, and the variety of material options is a response to evolving clinical requirements. Certain applications necessitate the utilisation of inertia, such as Co-Cr alloys and gold. On the other hand, certain applications call for the binding of the implant with the host fabric, such as titanium and titanium alloys. Lastly, there are cases when the implant must facilitate tissue growth and eventually replace the implant, as seen with magnesium alloys and iron. The majority of contemporary plants utilise Co-Cr and Ti alloys [92,93].
An implantable metal must possess biocompatibility, corrosion resistance, high specific strength (i.e., maximising mechanical resistance while minimising weight), high fatigue strength, high impact hardness (the ability to absorb energy through permanent deformation without fracturing), and low toxicity. An important issue with implants is the need to prevent against stress-induced bone weakening, known as osteopenia, caused by the implant's suppression of stress on the bone. To address stress shielding, one approach is to utilise a material, such as magnesium, that possesses a rigidity comparable to that of the cortical bone. Another method involves designing the implant with a porous structure that decreases its rigidity [94].
Therefore, it may be asserted that no individual metal or metal alloy have the ability to fulfil all of these criteria. In recent years, research has integrated the properties of metals with various 3D printing technologies. The combination of material and printing technology has enabled the production of implants that fulfil the specified criteria [33].

3.5.1 Ti6Al4V

The uses of titanium alloys for producing scaffolds utilising SLM are especially interesting (Fig. 13). In fact, the quantity of titanium SLM publications has been surpassed only by those related to steel. The majority of these researches are derived from either commercially pure titanium or Ti6Al4V alloy [95].

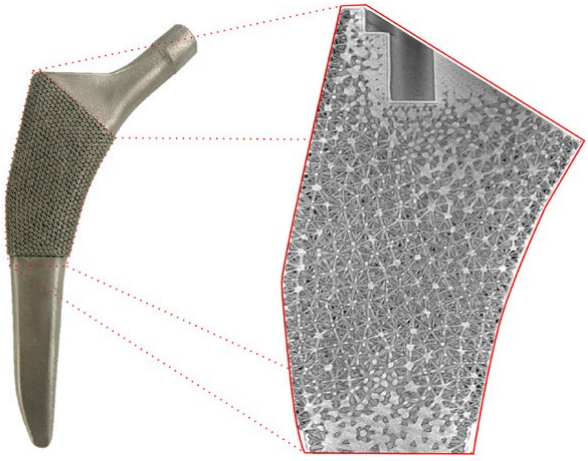

Fig. 13 Ti6Al4V implant produced by SLM with characteristic porous structure [96].

Titanium and its alloys have been widely used in biomedical implants since the 1970s due to their excellent biocompatibility, good corrosion resistance, and high specific strength [97].

Titanium has a hexagonal, close-packed lattice structure at room temperature, called α phase, and a body-centered cubic structure at 883°C, called β phase.
Alloying elements such as Al, C, and O extend the α phase by increasing the β/α transus temperature, while Mo, Ta, and Nb extend the β phase by reducing the transus temperature. Consequently, Ti alloys can be classified into four main groups: α-, near-α-, (α + β)-, and β-type alloys [98].
The mechanical properties of Ti alloys are strongly influenced by their composition, with the noticeable exception of the Young's modulus, which remains near constant.
The most common Ti-based materials used today in biomedical applications are commercially pure titanium and titanium alloy Ti6Al4V [99].
Commercially pure titanium (98.9% to 99.6% Ti alloyed with O and Fe) is a relatively weak α-type alloy that cannot be strengthened via heat treatment; consequently, it is used in non-load-bearing, corrosion-resistant applications, such as pacemaker cases, infusion drug pumps, and dental implants [93,100].
In contrast, Ti6Al4V is an (α + β)-type alloy whose mechanical strength can be increased up to 50% via heat treatment without significantly affecting its Young's modulus, making Ti6Al4V compatible with load-bearing applications, such as fracture fixation plates, hip stems, fasteners, wires, and screws. Ti6Al4V Extra Low Interstitials (ELI) alloy has fewer interstitial impurities such as O, N, C, and Fe, resulting in improved ductility and fracture toughness with some reduction in strength; consequently, Ti6Al4V ELI alloy has been widely used for bone fixation plates and in stems of artificial hip joints [101]. The grain size of Ti alloys can be modified via plastic deformation; smaller grains have fewer atoms per grain and higher surface energy, promoting higher osseointegration.
In particular, ultrafine-grained (grain structure in the submicrometer to nanometer range) commercially pure titanium and Ti6Al4V alloys have shown significantly better vascular and bone cell adhesion compared with conventional Ti6Al4v varieties [102].
Ti6Al4V alloys spontaneously form a passive TiO_2 film that contains OH^- ions that react with the bones' mineral constituents, promoting osteointegration. Although 50% of biomedical implants use Ti6Al4V, the alloy causes some concern as it contains Al and V, which are cytotoxic; consequently, aluminum- and vanadium-free Ti alloys have been developed for implant applications [103].
Furthermore, commercially pure titanium and Ti6Al4V are much stiffer than human bone, causing stress shielding. However, a key benefit of 3D printed Ti-based materials is the inclusion, without resorting to chemical processes, of an engineered porous structure to match the stiffness of the implant with that of the natural bone; the porosity also enhances bone cell growth, creating a strong twist lock between the bone and the implant that improves the success rate of the implant [104].

Chapter 4

3D printing Case Studies for tissue engineering: Bioprinting

The process of designing 3D scaffolds for TE applications is intricate, as it requires the analysis of multiple elements:

- tissue that needs to be replicated, whether it is rigid, flexible, etc.,
- appropriate material for the framework,
- cells that will be enclosed in the bioink are obtained and cultured in isolation, while maintaining their specific cultural characteristics,
- selecting a printing process that is appropriate for the chosen material and the cells that need to be encapsulated.

To successfully carry out this procedure, multiple skills are required: biologists contribute by providing knowledge regarding the structure and function of tissues and cells, while engineers are responsible for designing the geometry to be product and optimising the printing procedure.
This chapter will address the optimisation processes for printing parameters in EBB and ES, employing both inorganic polymer materials and biocompatible hydrogels and the incorporation of cells into a bioink for the construction of scaffolds using 3D BP:

- R. Rovetta, A. Pallavicini and P.S. Ginestra, “Bioprinting process optimization: case study on PVA (Polyvinyl Alcohol) and Graphene Oxide biocompatible hydrogels”, Procedia CIRP, (2022), 145-149, 110(C)
  In this work, the candidate was responsible of the literature search, data collection and organization, and writing and editing of the draft.

- P.S. Ginestra, R. Rovetta, A. Fiorentino and E. Ceretti, “Bioprinting process optimization: evaluation of parameters influence on the extrusion of inorganic polymers”, Procedia CIRP, (2020), 104-109, 89
  In this work, the candidate was responsible of the test campaign, measurements and analysis of the collected data.

- M. Seiti, R. Rovetta, R. M. Ferraro, E. Ferraris and E. Ceretti, “Optimization of the FRESH 3D printing method applied to alginate – cellulose-based hydrogels”
  In this work, the candidate was responsible of the sample measurements, and collaborated in the test campaing.

- G. Gaudenzi, R. Rovetta, E. L. Mazzoldi, S. C. Giliani and P. S. Ginestra, “Bioprinting of Alginate/Gelatin hydrogel: Cell metabolic activity and proliferation response”, under review at Journal of Intelligent Manufacturing
  In this work the candidate was responsible of the samples design and fabrication. Moreover, she designed and carried out the testing. She collaborated in the data organization and analysis. Finally, he contributed to the writing and editing of the draft.

4.1 Bioprinting process optimization: case study on PVA (Polyvinyl Alcohol) and Graphene Oxide biocompatible hydrogels

Scaffolds manufacturing for TE is an elaborate process since to fabricate a functional tissue, the engineered structures have to mimic the extracellular matrix. The key goal is to produce 3D scaffolds composed of macro- and micro- scale structures. The combination of different production technologies, as 3D BP and ES, enables the fabrication of multiscale structures but, above all, the biomaterial choice is crucial to apply these technologies.
Hydrogels based of Polyvinyl alcohol (PVA), a water soluble and biodegradable polymer, are able to create a highly hydrated environment that promotes cell attachment and proliferation, with limited mechanical properties. A good strategy to improve this properties is to incorporate carbon based materials in the hydrogels-matrix such as graphene oxide (GO). GO, due to its particular structure and tailorable biocompatibility, has been widely used in scaffold manufacturing.
The results show that PVA/GO hydrogel can be processed with both ES and 3D BP technologies with a proper process optimization confirming the good dispersion of the GO within the polymer. The aim of this work is to study whether ES and 3D BP can be used with the same material, to produce novel porous structures for biological applications, in particular connective tissues, and thus optimize the biomanufacturing process.

4.1.1 Introduction

A typical TE manufacturing process has three main steps: (i) preprocessing with the manipulation of the data acquired from the medical scans; (ii) processing that involves prototyping 3D model and scaffold production; and (iii) postprocessing that includes all the necessary steps to promote cell proliferation to create the tissue [1].
The manufacturing steps embed two of the most important choices for TE process: the production technology and the biomaterial. TE combines engineering and biology fields to replicate human tissues using BP technology, it could reduce or completely eliminate the organ transplant shortage, giving everyone an equal second chance, with a customized product [2,3]. TE requires 3D scaffolds with well-defined external and internal shapes and structures, which are feasible with the 3D BP [4]. 3D BP process consists of print and pattern of the cells on a substrate or tissue through an automated dispensing system. The position and orientation, the diameter size of extruded filaments, the print path, lay-down pattern, or simply “scaffold design”, affects the mechanical properties. Alongside with the variety in the technology of 3D BP, the selection of biomaterials is related to the application of the end product. The main properties are usually: the morphological properties, due to the production technology, and the biological properties, due to the used biomaterial [5]. The Envisiontec Bioplotter® is especially designed to create physical scaffolds from CAD data [6].
The BP technique used can be described as EBB [7]. The materials that can be used range from thermoplastic polymers to viscous pastes and liquids. Using layered deposition, parallel lines of material are created, resulting in a very fine "mesh" with good mechanical properties and a mathematically well-defined porosity. Several synthetic and natural polymers are involved in BP application to obtain a good realization of tissue substrates [8].
Natural polymers have often been used as scaffolds because of their biocompatibility, bio-functionality and lower cytotoxicity. To enhance the printability of natural polymers crosslinking

is commonly used. Although natural polymers have the advantage of creating specific cellular interactions, they are commonly used in this field but they have limited versatility in relation to their mechanical properties. The most frequently used are: Silk Fibroin; Chitosan; Collagen; Hyaluronic acid; Gelatin; Chitin; Fibrinogen. Numerous synthetic polymers have been applied too. The main advantages of synthetic polymers are their printability, excellent mechanical integrity and cost-effectiveness. They can also be modified with chemical functional groups that can help the growth and the proliferation of cells. PVA is a nontoxic, biodegradable, biocompatible semi-crystalline, highly hydrophilic polymer is used in a wide range of industrial and medical applications due to its great properties such as good thermal stability, good physical properties, water solubility, gas permeability, flexibility and inexpensive cost [9,10].

One of the most interesting kind of biomaterials are hydrogels, because they have a structure like the natural extracellular matrix and are able to create a highly hydrated environment that promotes cell attachment [11]. Hydrogels define the physical-mechanical properties of the bioinks, even if they are not optimal, properties such as elasticity and rigidity can be improved by various strategies. One of the many solutions that can be adopted to solve this problem consists in incorporating nanoparticles in the hydrogels-matrix, in order to improve functionalities and properties. For example, the possibility of incorporating carbon-based materials leads to better thermal and electrical conductivity. Two-dimensional graphene materials, such as Graphene oxide (GO) and Reduced Graphene oxide, have been widely used in various biomedical research areas such as bioelectronics, drug delivery and TE [12–14].

In recent studies, the research is focused on the material extrusion process to produce customize scaffolds to meet the individual needs, with the ability to create complex geometries and high-accuracy features, and the possibility to control pore size and distribution of pores within the scaffold, nowadays this is not obtainable with traditional manufacturing processes: 3D BP shows a low resolution fabrication limits. A subject of great interest is the use of ES production technology with AM principles [15]. With smaller pores and higher surface area than regular fibers, electrospun fibers have been successfully applied in various fields, such as nanocatalysis, TE scaffolds, protective clothing, filtration, biomedical, pharmaceutical, optical electronics, biotechnology, defense, security and environmental engineering. ES, due to the dynamic nature of fiber deposition, is unable to reproduce 3D structures, and the limitations of 3D BP concern to the low resolution of the scaffold internal structure.

The aim of this work is to study whether ES and 3D BP can be used together to produce new porous structures for biological applications, and to optimize a novel hybrid biomanufacturing process [16]. The biocompatible hydrogel based on PVA and GO is a material with interesting properties: the presence of graphene in its structure makes it an efficient platform for the differentiation and growth of cells and stem cells, and the oxygen functional group helps in attaching to molecules or surfaces. In combination with ES fibers and 3D BP structures, it can create scaffolds suitable for TE, in particular connective tissues such as skin, ligament, muscle, and tendon, as well as vascular and neural tissue, regenerative medicine and drug delivery.

4.1.2 Materials and Methods

4.1.2.1 Materials

PVA in powder form (Mw 89.000-98.000, 99+% hydrolyzed) and GO solution (4mg/ml, dispersion in H2O), were purchased from Sigma-Aldrich Chemistry. PVA and GO solution can be both heated up to 120°C in order to be sterilized for biomedical applications.

4.1.2.2 Solution Preparation

The synthesis procedure for the PVA/GO solution was as follow: the PVA powder was slowly added in distilled water with rapid stirring at 90°C, once the solution has been obtained, liquid GO was added, in order to obtain certain concentrations. The solution obtained did not have the hydrogel feature, in fact it was too liquid, with an high amount of air bubbles and a low dispersion of GO. Therefore, to prepare an homogeneous solution to obtain the PVA/GO hydrogels, with the polymer concentrations set at 10 and 30 wt%, PVA powder was directly dissolved in 13 mL of GO aqueous dispersion (4 mg/mL) with rapid stirring under heating at 90 °C for 1h [15].

4.1.2.3 Design of experiments

The aim of this work is to optimize the biomanufacturing process with a specific hydrogel, in particular:

- PVA/GO 10 wt% was electrospun and the sample were then observed under scanning electron microscopy Zeiss LEO 1525 (SEM) to evaluate the fibers deposition.
- PVA/GO 30 wt% was extruded to optimize the 3D BP process analyzing the material printability and relative printing parameters: speed and pressure.

The EnvisionTec 3D Bioplotter® implemented software allows the tuning of the printing parameters through a tool called “Manual Parameter Tuning”. The printed sample were then observed under Mitutoyo optical microscope to defined a range of parameters to obtain the highest printing stability and quality of the product.

4.1.2.4 Experimental Tests

For the ES process was used a stainless steel flat-pointed needle with an internal diameter of 0,8mm (G21). The needle was connected to the positive electrode. The syringe of 10 ml, with the solution, was connected with a pump [17,18]. The nanofibers were collected on a grounded metallic collector, square-shaped covered with aluminium foil. The potential was set from 0 kV to 20 kV and a current intensity from 3 μA to 7 μA was reached. The process parameters investigated are shown in Table 1.

Table 1 ES process parameters designed tests.

Parameters	Flow rate q [mL/h]	Needle-Collector distance D [mm]
Values	0.1; 0.3	60;90;120

It is useful determine the optimal printing parameters for the solution used. In the BP tests, two parameters were fixed throughout the process: the temperature of the printing plate and the

temperature of the solution, assumed to be constant, at room temperature (25°C). The two temperatures were fixed, so it was possible to work on the combination of speed and pressure. In this optimization process it was possible to operate in two ways: keeping the speed fixed and varying the pressure, or varying the speed while keeping the pressure fixed [19]. For each pressure/speed value set, the Bioplotter divided the relevant value into a range of values shown in Table 2 and Table 3. They could be analyze in order to choose the most suitable ones.

Table 2 BP Tuning #1 designed tests.

P [bar]	V [mm/s]	Zoffset [mm]	dneedle [mm]
0.5 ÷ 1.5	5 ÷ 15	0.4; 0.75; 1.1	0.4
V = 10 mm/s	P = 1 bar		

Table 3 BP Tuning #2 designed tests.

P [bar]	V [mm/s]	Zoffset [mm]	dneedle [mm]
0.8 ÷ 1.2	5 ÷ 10	0.75	0.4
V = 7.5 mm/s	P = 1 bar		

4.1.3 Results and Discussion

4.1.3.1 ES tests

The morphology of the samples is reported in Fig. 1. At low distance and minimum flow rate there is electrospray, not ES (a). There has been the creation of clusters of polymer and graphene that have clearly not been transformed into fibers, the graphene phase on PVA is prevalent. A higher flow rate generates more fibers (b), the polymer phase can be compared to the graphene phase. The figure shows fibers connecting the solution droplets, increasing the flow rate from 0.1 mL/h to 0.3 mL/h creates the possibility of producing more filaments. The clusters visible in the figures are probably clusters of graphene oxide, as PVA and graphene have different behavior towards light, if it is darker it is the graphene component that reflects less light due to its conductivity. In the following two samples the distance is increased from 60 mm to 90 mm that helps the formation of fibers.(c). The presence of drops is due to a solution that needs to be optimized, PVA and GO are electrospinnable together, but the number of drops present is significant and affects the quality. These chosen process parameters proved to be the best of all those tested. By increasing the flow rate from 0.1 mL/h to 0.3 mL/h, the crystallization of the solution appears, specifically crystallization of the polymer (d). The possible cause is the evaporation of the aqueous phase, but the effect is unintended and therefore cannot be controlled. The dispersed droplets are dry and appear as polymer agglomerates; this could be due to the conductivity of the solution, by moving away at 90 mm and choosing an excessively high flow rate, led to a deviation of the flow, consequently deflecting the fibers from the collector. The collector received the residues of the solution deposit. In the last two sample the distance increases further from 90 mm to 120 mm and the crystallization of the polymer is still visible (e). These

process parameters not only lead to crystallization but also to a poor mass deposition, as the bottom of the aluminum foil can be seen; this means that there was no mass deposition of fibers. So, to avoid this problem the flow rate is increased to 0.3 mL/h (f), causes bigger agglomerates and scarce deposition. The only distance with a successfully electrospun fibers is 90 mm.

4.1.3.2 BP tests

The BP process optimization starts from the quality evaluation of the printed strands. All the different parameters influence the result in a specific way, in particular pressure and speed produce the most apparent effects. In Fig. 2 is shown the material parameter tuning test: Tuning #1. The strands have different shapes according to pressure and speed values.
The first five filaments are printed with a fixed speed and a variable pressure. Increased pressure causes a higher material amount, values between 1 and 1.5 bar ensure strands with enough material to handle an additional layer. Similarly, the increased speed deposition leads to droplets and not uniform filaments. Specifically, the speeds between 7.5 and 15 mm/s are too high; stretching is excessive, with visible dragging. Instead, the speed of 5 mm/s combined with a pressure of 1 bar produces excessive material deposition. The optimal strands, in this first test, are those obtained at constant speeds of 10 mm/s with pressures of 1 – 1.3 – 1.5 bar. Consequently, the area of optimization is restricted by carrying out a second test with more stringent ranges.

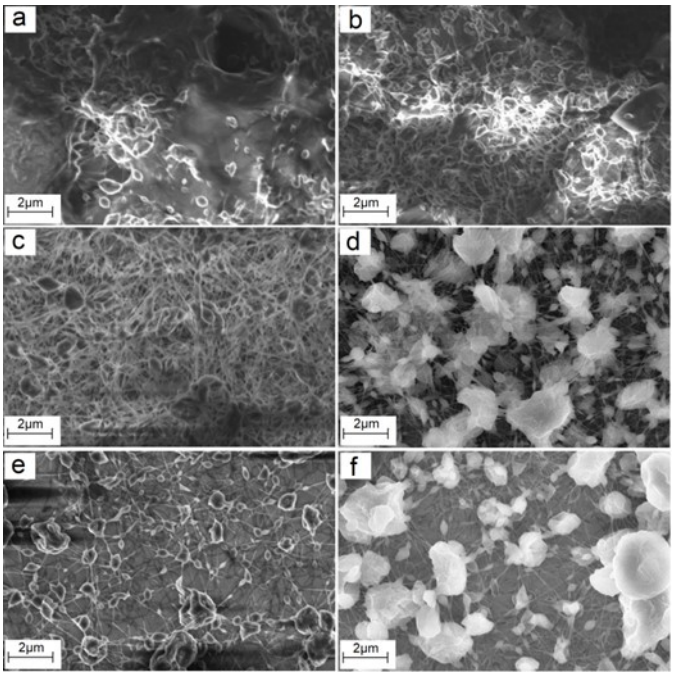

Fig. 1 SEM images of PVA/GO fibers electrospun at needle-collector distance and flow rate as designed:
(a) q=0.1 mL/h, D=60 mm; (b) q=0.3 mL/h, D=60 mm;
(c) q=0.1 mL/h, D=90 mm; (d) q=0.3 mL/h, D=90 mm;
(e) q=0.1 mL/h, D=120 mm; (f) q=0.3 mL/h, D=120 mm.

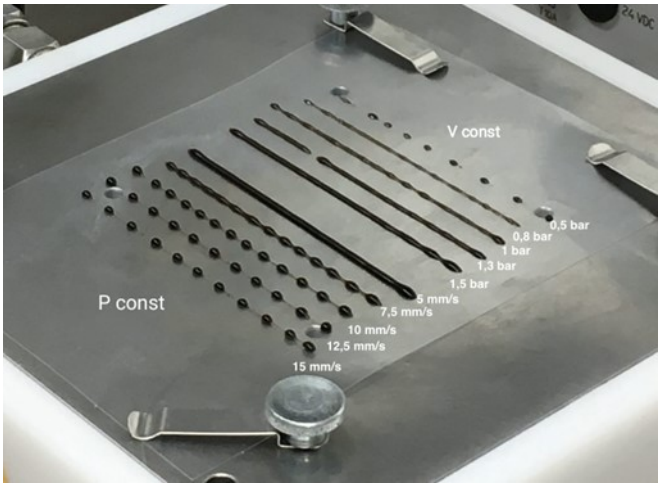

Fig. 2 Platform with strands of the first manual parameter tuning.

The second test shows the best results, the pressure range is narrower, going from 0.8 to 1.2 bar and the speed from 5 to 10 mm/s. So, the speed values from 5 to 7.5 mm/s, and the pressure at 1 – 1.1 – 1.2 bar, represent the optimal area. These values are the most promising and create thinner, dimensionally well-deposited filaments. The improved quality of the strands is demonstrated by the optical analysis in Fig.3.

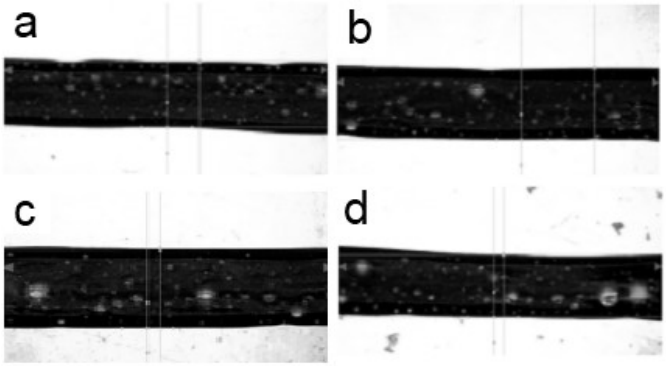

Fig. 3 Optical images of PVA/GO 3D BP strands thikness measurements:
(a) P=1.1 bar, V=7.5 mm/s, d=1.182 mm;
(b) P=1.2 bar, V=7.5 mm/s, d=1.585 mm;
(c) P=1 bar, V=5 mm/s, d=1.890 mm;
(d) P=1 bar, V=7.5 mm/s, d=1.499 mm.

4.1.4 Conclusion

The aim of this work was to optimize the biomanufacturing process of a biocompatible hydrogel based on polyvinyl alcohol and graphene. The production technologies used were ES and 3D BP. In order to identify the optimal parameter to produce, with the same biocompatible material, two different type of structures: micro-scale structures with ES and macro-scale structures with 3D BP were obtained. This multimodal production technology can be used in several biomedical application, in particular TE, to replicate the natural tissue.
ES tests have shown the PVA/GO biomaterial performances for fibers production, in particular with a good degree of incorporated graphene oxide. The most satisfactory parameter combination

was therefore a flow rate set at 0.1 mL/h, needle tip-to-collector distance 90 mm and voltage 20 kV. The solution needs to be optimized and more tests should be carried out in order to have fewer dispersed air bubbles, with narrower ranges, close to the more satisfactory ones described above. BP tests have confirmed the stability of the PVA/GO hydrogel but, in order to achieve a multiple layers deposition, some crucial aspects must be clarified. First of all, the critical points of the material deposition are the first and end points of deposition. In fact the start and stop phases caused material accumulation. This could create difficulties on the continuous deposition in a 3D BP process. Secondly, it could be helpful to cool the printing plate. This will enable the cold to be transferred from the printing plate to the various overlapping layers and guarantee structural strength. Another critical issue is related to the formation of air bubbles. In fact, the solution had to have a certain degree of viscosity and structural strength, so the PVA concentration was increased to 30%. This considerable addition of PVA presented criticalities; the resulting filaments observed under the microscope had too many dispersed air bubbles and therefore defects. The presence of bubbles in the solution was due to the solution preparation. PVA has been added to the GO solution and, despite of the homogeneous mixture obtained, OH-bonds have been broken. In order to overcome this problem of bubbles, a good strategy could be try to dry the solution. In the second test, the filaments obtained at a constant pressure of 1 bar and variable speed of 5 and 6.25 mm/s were thin and uniform, with no interruptions. In particular the possibility of cool down the printing plate to achieve structural resistance of the layers and optimize the composite solution, and the thickness of the deposited strands are going to be studied in order to identify the process stability area needed for multi-layered printing tests.

4.2 Bioprinting process optimization: evaluation of parameters influence on the extrusion of inorganic polymers

BP consists in an innovative approach able to improve the current techniques of bioregeneration in the medical field through the extrusion of cell-loaded bioinks. Its main advantage is the customization to reduce post-operative complications on the patient, as it can be produced from his own cells. The success of BP is determined by the printing parameters but, above all, by the materials. The goal of this work was to define a range of parameters, in order to achieve the highest printing stability, in terms of the quality of the Bioplotter® Silicone TG in relation to process conditions used.

4.2.1 Introduction

3D printers are able to produce physical objects, starting from a 3D model, through the deposition of several layers of material [1–3]. The materials used in 3D printing are mainly plastic, metallic and polymeric, but living cells can also be used to artificially reproduce tissues, blood vessels and organs [4]. Among the several biomanufacturing techniques [5–7], 3D printing technologies faced a rapid expansion of applications in medicine and TE for the fabrication of scaffolds [8–10]; while BP, through the use of biocompatible materials, has been developed for the production of different natural tissues, including skin, cartilage, bone, neural and muscle tissues [11–13].
BP consists in an innovative approach able to improve the current techniques of bioregeneration in the medical field through the extrusion of cell-loaded bioinks.
This innovative approach is improving the current techniques of bioregeneration in the medical field due to the high degree of customization involved, which allows to reduce post-operative complications on the patient, as it can be treated with his own cells or specific stem cells [14,15].
EBB can print a wide range of biomaterials, including solutions, pastes or dispersions but is applicable only to viscous liquids and has limitation on complexity of shapes. The success of the EBB is determined by the technique and the printing parameters but, above all, by the materials. Thus, the optimization of the extrusion process is required to identify the potential applications and performances of a new biocompatible material. One of the most important feature of 3D BP is the bioink, which is the bio-printable material used in the process. This material should be biocompatible, in order to accommodate live cells, and mechanically stable after printing. The biomaterials used, either encapsulating
cells or loaded with cells later on, are generally injected into metal or plastic syringes and extruded with the application of a proper pressure. The Envisiontec 3D Bioplotter® System is a versatile machine tool, mainly used to prototype a great variety of biomaterials from 3D CAD models. The Bioplotter® is a multi-part and multi-material system using an automatic tool changer and multiple print heads, with individual temperature control. A liquid, melt, paste or gel is dispensed from a material cartridge through a needle tip from a 3-axis system to create a 3D object. It is designed for use in a sterile environment within a biosafety cabinet; indeed, the equipment includes built-in particle and sterile filters for the input compressed air [16].
The Envisiontec Bioplotter® is able to print a great variety of biomaterials, but the first material tested with the first 3D-Bioplotter prototype in 2000 was Silicone [17,18].
Silicone has been on the market for many years and is currently used in many processes, both industrial and

domestic. In fact, silicone is a polymer made from silica contained in sand and rocks, and it can be found in solid and liquid form, depending on the length of the chain and their cross-linking degree. Silicon is very versatile, economical and different textures can be tested according to the requirements of the final application, especially in medical fields. This paper is focused on the evaluation of the material characterization methodology developed for the Bioplotter® equipment. More specifically, the goal of this work was to define a range of process parameters, in order to achieve the highest printing stability, in terms of the quality of the 3D-Bioplotter® Silicone in relation to the nozzle dimensions and process conditions used. In particular, the influence of extrusion pressure and speed on precision and uniformity of the produced components was analysed, so to optimize the process and to identify the influence of these parameters on filament formation and deposition too. The realized strands were observed under optical microscope and measured in terms of diameter of the deposited wire. The statistical analysis of the results was carried out to consider the effects of each factor and their interactions on the final geometry to gain a better reproducibility and repeatability of the part. The proposed procedure can be considered a valid approach for the optimization of the process parameters for the extrusion of new developed materials.

4.2.2 Definition of the tuning parameters

In this section, the experimental method for the extrusion process optimization is reported. In particular, different tests were carried out in order to define a promising area for the obtainment of a diameter of the silicon extruded filament in relation to the diameter of the used nozzle. The extruded filaments were produced by the 3D-Bioplotter® printer whose range of process parameters is reported in Table 1. The Bioplotter® printer works as a material extruder where A liquid, melt, paste or gel is dispensed from a material cartridge through a needle tip from a 3-axis system to create a 3D object.
The key feature of the 3D-Bioplotter is the flexibility in the choice of materials. In particular, the Bioplotter®
allows the evaluation of the extrusion properties of new materials and the setting of the processing parameters by using the Material Parameter Tuning procedure. The needle offset defines the starting spacing between the needle tip and the platform at the beginning of the extrusion process. Values between 50% and 100% of the inner diameter of the needle tip can be chosen, dependent on the materials and platform substrate.

Table 1 Bioplotter® manufacturer series parameters.

Process parameter	Range values
Platform temperature (T)	-10°C - 80°C
Heads #	Low: 0°C - 70°C High: 30°C - 250°C
Cartridge sizes	10 - 30 ml
Build volume	150x150x140 mm^3
Speed (V)	0.1-150 mm/s
Pressure (P)	0.1-9.0 bar

The most important parameters that are considered in this work are the extrusion pressure and speed. Under

Pressure Tuning Parameter a fixed speed can be selected, as well as the minimum and maximum pressures. Five strands are printed on the back half of a 100x100 mm surface. Similarly, the Speed Tuning Parameter can be used at a fixed Pressure with Min and Max Speed values. These five strands are printed in the front half of the 100x100 mm surface.
The Technical Grade Silicone (TG, Envisiontech®, Silicone, viscosity=1,900,000mPs) was extruded with the
printer low temperature head to evaluate the process stability.
The parameters of speed, pressure and offset in the Z direction were modified to achieve the optimal printing
conditions considering the deposition and uniformity of the extruded filament. The following tests were performed at room temperature:

- Pressure tuning: speed kept fixed at the intermediate value of the tuning speed range, while the pressure range is divided into 5 values of the imposed range values.
- Speed tuning: pressure kept fixed at the intermediate value of the tuning pressure range, while the speed range is divided into 5 values of the imposed range values.

The tuning configurations imposed were chosen in order to find the optimal value of the offset in the Z direction for this type of material, varying pressure and speed of extrusion (Table 2, 3 and 4). Each tuning is performed by fixing one of the values of the Zoffset (between 0.35 and 0.38 mm) and varying the pressure values at a certain speed (10, 13 and 15 mm/s) or varying the speed values at a certain pressure (2, 2.3 and 2.5 bar)-. At each value of the Zoffest, two tests were carried out: one for the pressure tuning at a fixed speed (i-e. 10mm/s for tuning#1) and one for the speed tuning at a fixed pressure (i.e. 2.3 bar for tuning#1). The first tuning (tuning #1) configuration was imposed according to the material datasheet provided while
the second tuning (tuning#2) was designed to narrow the range of parameters and find the right Zoffset. The third tuning (tuning #3) was then carried out for the optimization of the pressure and speed parameters of the process. Three repetitions were fabricated for each process parameters set.

Table 2 Designed tuning configuration (#1). The pressure values were varied between 0.5 and 4 bars at a fixed speed of 10 mm/s while the speed values were varied between 5 and 15 mm/s at a fixed pressure of 2.3 bar.

Tuning #1		
Pressure [bar]	Speed [mm/s]	Z offset (mm)
from 0.5	from 5	0.35
to 4	to 15	0.36
V=10 mm/s	P=2.3 bar	0.37
		0.38

Table 3 Designed tuning configuration (#2). The pressure values were varied between 2 and 3 bars at a fixed speed of 13 mm/s while the speed values were varied between 12 and 14 mm/s at a fixed pressure of 2.5 bar.

Tuning #2		
Pressure [bar]	Speed [mm/s]	Z offset (mm)
from 2	from 12	0.35
to 3	to 14	0.36
V=13 mm/s	P=2.5 bar	0.37
		0.38

Table 4 Designed tuning configuration (#3). The pressure values were varied between 1.8 and 2.2 bars at a fixed speed of 15 mm/s while the speed values were varied between 14 and 16 mm/s at a fixed pressure of 2 bar.

Tuning #3		
Pressure [bar]	Speed [mm/s]	Z offset (mm)
from 1.8	from 14	0.36
to 2.2	to 16	
V=15 mm/s	P=2 bar	

4.2.3 Extrusion characterization

To understand if the parameters involved in the process reflected our expectations, for each test performed, the diameter of the printed strands was measured, using Mitutoyo microscope, and compared with the diameter of the nozzle used: 0.4 mm. The microscope images were processed with ImageJ software [19] to measure the diameters of the filaments. The measurements were taken on different areas of the strand to consider the uniformity of the extrusion.

4.2.3.1 Tuning #1

The results of the tunings are reported in Fig. 1 and 2 showing the diameters of the extruded filaments that were classified in ranges of values closer to the diameter of the nozzle (d0=0.4mm). The absolute value of the difference between the extruded filament (d) and the nozzle diameter (d0) has been considered. In particular, the green color represents the values nearer to the nozzle diameter which can be considered optimal in terms of quality of the filament ($|d-d0|\leq 0.05$), the yellow dots are considered acceptable values ($0.05<|d-d0|\leq 0.1$), the orange dots represent a bad quality of the extruded filament ($|d-d0|>0.1$) while the red ones are considered points of inapplicability of the printing (i.e. discontinuities, irregular printing, air bubbles).

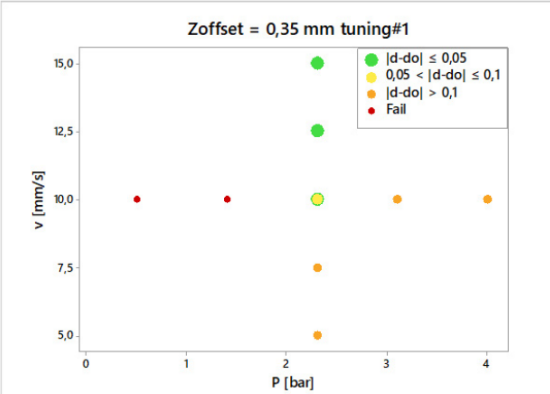

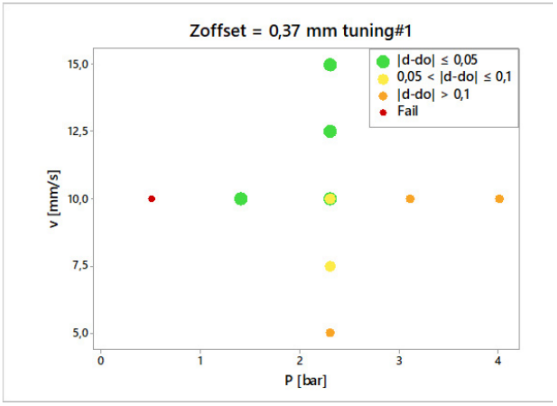

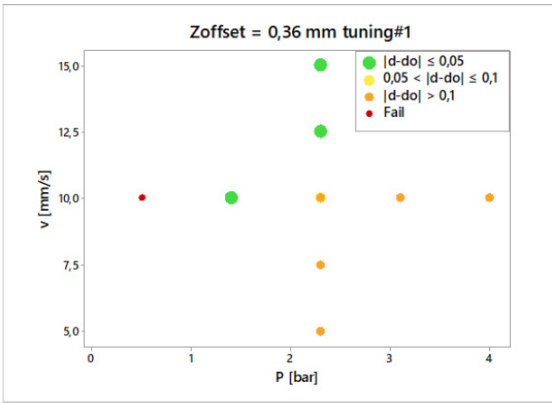

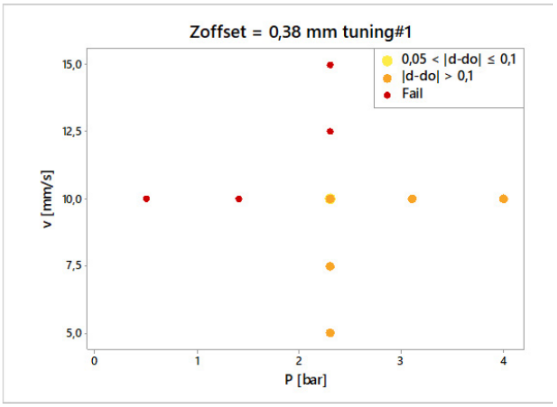

Fig. 1 Results of the tuning#1 considering offset values of 0.35 mm and 0.36 mm. The dots represent the value ranges of the diameter of the filament and each color correspond to a level of acceptation of the filament diameter values. In both cases, the optimal values were found at a pressure of 2.3 bar and a speed ≥ 10 mm/s.

Fig. 2 Results of the tuning#1 considering offset values of 0.37 mm and 0.38 mm. The dots represent the value ranges of the diameter of the filament and each color correspond to a level of acceptation of the filament diameter values. While at a Zoffset of 0.37 mm the optimal values were find at a pressure of 2.3 bar and a speed ≥ 10 mm/s, at a Zoffset of 0.38 mm the diameter of the filament is printed in bad quality or tends to be not printable.

From the results of tuning#1 (Fig. 1 and 2) it can be concluded that as the Zoffset increases, at low values of pressures and high speeds, the precision of the printed strands decreases, making the filament often not uniform, wavy or full of droplets. These tests are represented with red dots, which define the inapplicability of the printing process and consequently the measurement. At lower values of Zoffset (0.35 and 0.36 mm/s), the optimal values of diameter are found at higher values of speed (≥10 mm/s) due to the dragging force that prevent the compression of the filament. This effect is reduced at a Zoffset of 0.37 mm, where acceptable values can be found at lower speeds (≤ 10 mm/s). The same considerations are not valid for a Zoffset equal to 0.38 mm due to the inadequate values of the pressure that are not allowing enough deposition of material. Considering these results, higher values of speed and pressure were selected for the tuning#2 for obtaining filament diameters within the range of 0.4±0.1 mm with a speed higher than 12mm/s and a pressure higher than 2 bar.

4.2.3.2 Tuning #2

The tuning#2 was based on a different range of parameters due to the analysis of the results of tuning#1. In particular, the ranges of both pressure and speed parameters were restricted and the

offset values considered in this case were amplified. From the graphs in Fig. 3 and 4, as from the previous tests carried out, it can be noticed that the offset in the z direction, that allows to get to the most promising results, is 0.37 mm (92% nozzle diameter). Moreover, the diameters are closer to 0.4 with a variability of ±0.05 mm when the pressure is less than 2.25 bar and the speed higher than 12.5 mm/s.

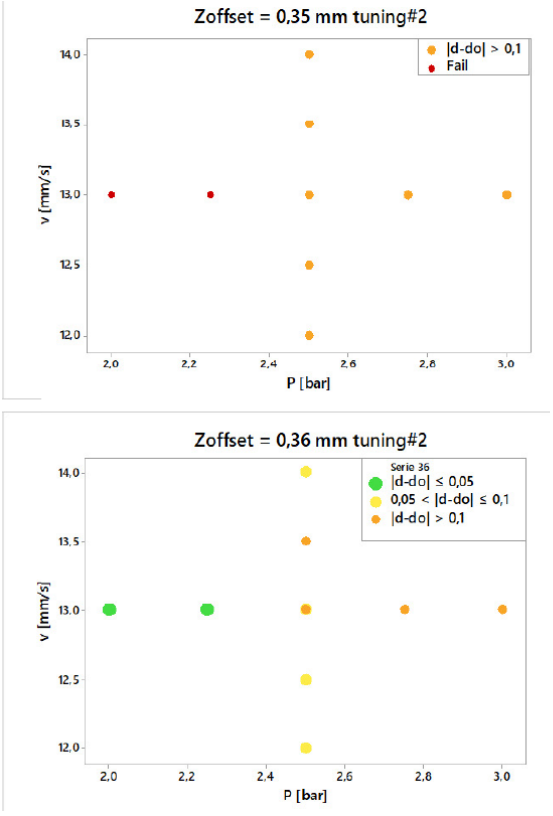

Fig. 3 Results of the tuning#2 considering offset values of 0.35 mm and 0.36 mm. The dots represent the value ranges of the diameter of the filament and each color correspond to a level of acceptation of the filament diameter values. In first case (Zoffset=0.35 mm), the quality of the filament results bad for every parameters combination, in the case of Zoffest=0.36 mm, the optimal values were found at a pressure ≤ 2.3 bar and a speed of 13 mm/s.

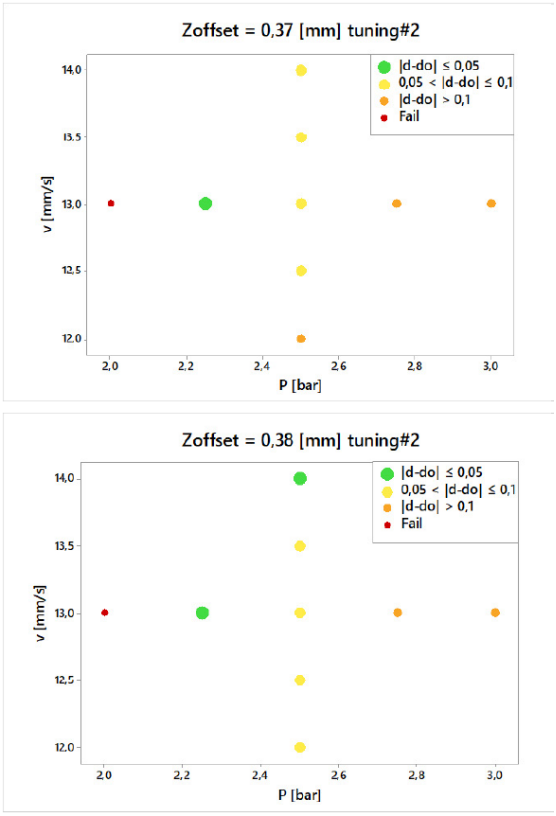

Fig. 4 Results of the tuning#2 considering offset values of 0.37 mm and 0.38 mm. The dots represent the value ranges of the diameter of the filament and each color correspond to a level of acceptation of the filament diameter values. With a Zoffset of 0.37 mm, one optimal value was found at a pressure of 2.3 bar and a speed of 13 mm/s while with a Zoffset of 0.38 mm, two optimal values were found at a pressure of 2.3 bar and speed of 13 mm/s and at a pressure of 2.5 bar and a speed of 14 mm/s.

From the results of tuning#2 (Fig. 3 and 4) it can be concluded that at a Zoffset of 0.35 mm, at low values of pressures, the precision of the printed strands decreases, making the filament often not uniform, wavy or full of droplets. As the pressure is increased, still not acceptable values of the diameters are measured. At higher values of Zoffset (0.37 and 0.38 mm/s), the optimal values of diameter are found at higher values of speed (≥10 mm/s) and pressures between 2.3 and 2.5 bar. This can be explained by the fact that these pressure values assure an adequate deposition of material and the speed values can be increased. The Zoffset of 0.36 mm offers a wider range of optimal values at lower pressures due to the right position of the needle tip in relation to the plate that influences the amount of material deposited. These results confirm the influence of the Zoffset on the parameters tunings to perform a process optimization. In particular, a Zoffset of

0.36 mm was chosen for the final tuning allowing the application of lower pressures values for the obtainment of the optimal filament quality.

4.2.3.3 Tuning #3

Tuning#3 has been carried out considering a fixed value of the Zoffset equal to 0.36 mm taking into account the results of tuning#2. The speed values were increased considering the trending of the diameter values resulted from tuning#1 and tuning#2 that showed an improving of the diameter values at higher speed (Fig. 1,2 and 4). Fig. 5 reports the results of the measurements on the extruded filaments.

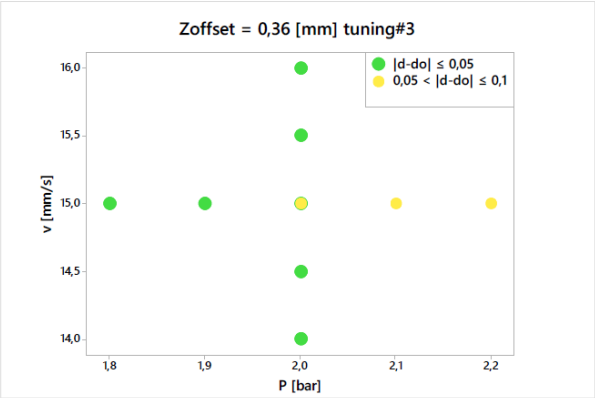

Fig. 5 Results of the tuning#3 considering an offset value of 0.36 mm. The dots represent the value ranges of the diameter of the filament and each color correspond to a level of acceptation of the filament diameter values. In this case, the optimal values were found at a pressure ≤ 2 bar and a speed ≥ 14 mm/s.

From these last results, it can be concluded that the most suitable values to assure a diameter of the filament as closer as possible to the diameter of the selected nozzle are:

- 1.8 bar ≥ Pressure ≤ 2 bar
- Speed ≥ 15 mm/s

Nevertheless, at a speed of 15 mm/s, as the pressure increases, the precision of the printed strand decreases, and it moves increasingly away from the target value of 0.40 mm of the nozzle diameter. To show what was found by the tuning of the parameters, Fig. 6 reports three examples of printed filaments during tuning#3 at fixed speed equal to 15mm/s and increasing pressure from 1.8 bars to 2.2 bar. The filament diameter tends to increase with an increasing of the pressure value.

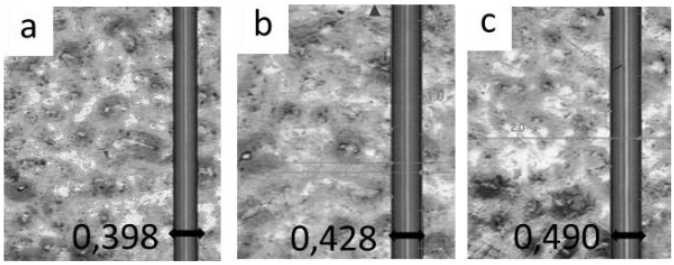

Fig. 6 Optical microscope images 1.5x of the silicon strands produced by the extrusion at a speed of 15mm/s and pressure of 1.8 (a), 2.0 (b) and 2.2 (c) bar.

It can be noticed that all the strands have no interruptions, waves or drops along the deposition area while, when the pressure is increased, the diameters of the strand starts to increase. The results are confirmed by the contour plot and the 3D scatter plot considering all the tunings performed with a Zoffset equal to 0.36 mm (Fig. 7).
These results confirm the advantages offered by the material tuning for the parameters optimization of the
printing process of new materials.

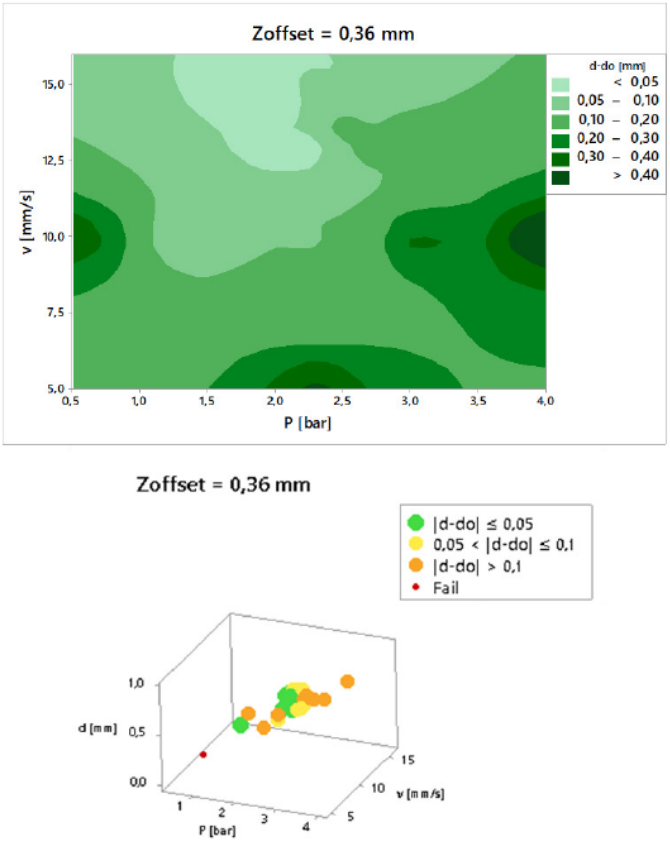

Fig. 7 Contour and scatterplot of d-d0 as a function of different pressure and speed values. The contour plot helps in defining the optimal region of values corresponding to specific combinations of the parameters used for the process optimization (speed and pressure) while the scatterplot defines all the points considered in the analysis to identify the area that has been investigated.

4.2.4 Conclusions

The paper deals with the extrusion characterization of a new generation 3D printer: the 3D-Bioplotter® manufacturer series. The objective was focused on the evaluation of the tunings schemes that can be executed by the equipment for the characterization of a new material that has to be extruded. The process was analyzed by the extrusion of the TG Silicone provided by Envisiontec by using the low temperature head of the printer. In particular, the diameter of the extruded filament was analyzed under optical microscope to measure the variability of the diameter of the extruded silicone strands in relation to the diameter of the selected nozzle. Three

tunings based on different combinations of pressure and speed used during the process were performed.

From the experimental results reported in this work it can be concluded that the offset in z direction influences the extruded diameter within a percentage of 10% while when the offset is kept constant, it is possible to define a process window corresponding to the extrusion stability for the specific analyzed material. In particular, the higher precision of the process is found when a pressure of 2 bars is chosen in relation to a speed between 14 and 16 mm/s. The dispense pressure is dependent on the material flow through the nozzle and must be adjusted to the rate at which the material hardens. A low dispense rate will allow the material to harden while still being affected by the needle tip, resulting in thinner and rounder strands. A dispense rate too fast relative to the hardening speed will result in wide, oval strands flattened by the material during the hardening period. A relatively low pressure ($\leq$2 bars) is allowing the silicone to harden in the right time to lead to filaments with a diameter closer to the nozzle's diameter. The dispense rate must be adjusted to the XY movement speed. A wrong relation between dispense pressure and XY movement speed will cause the formation of defects on the deposited strands. In particular, with a dispense rate too high relative to the XY movement speed, too much material is dispensed and the strand starts to swell. The optimal situation was reached when the material leaves the nozzle and is immediately pressed against the plate (14 mm/s $\leq$V$\leq$16 mm/s). The strand is only slightly deformed due to the type of material that is extruded (Fig. 7) but the strand is not stretched after being dispensed causing a delay in the deposition on the plate that would have led to droplet formation instead of round strands.

The procedure introduced in this work can be considered a valid methodology for the identification of the optimal process parameters for the testing of new materials. More specifically, this approach can be used for the testing of ad hoc designed materials not commercially available that need to be characterized to investigate and then tailor their extrusion process. The future investigations are going to be focused on the analysis of the data dispersion and the influence of the other process parameters such as the printing platform temperature. Moreover, the dimensions of the deposited strands during multi-layered printing tests are going to be studied in order to identify the process stability area and compare it to the one found for the deposition of one single strand.

4.3 Optimization of the FRESH 3D printing method applied to alginate – cellulose-based hydrogels

In recent years, a new AM method for 3D syringe-extrusion (bio)printing of soft hydrogels has been introduced under the name of Freeform Reversible Embedding of Suspended Hydrogels (FRESH). The most common FRESH bath contains gelatin as the main compound and low concentrations of crosslinker(s) (whose nature depends on the hydrogel) for the initiation of an *in-situ* pre-crosslinking process during printing. In the case of sodium alginate (SA)-based hydrogels ionically crosslinked via calcium chloride ($CaCl_2$), the crosslinker percentage in the gelatin bath is equal to ~10 mM, usually combined with a post-crosslinking at higher concentrations. However, according to the best authors' knowledge, no study has ever reported the combined effect of pre- and post-process crosslinker concentrations over printability using the FRESH method. Therefore, this manuscript aims to systematically investigate via a full-factorial design, the printing of two low viscous SA – cellulose-based hydrogels, containing carboxymethylcellulose (CMC) or mi-cro-fibrillated cellulose (mFC). Different concentrations of $CaCl_2$ are selected for the gelatin-based FRESH support bath (10, 30, or 50 mM) and for the post-cross-linking process (0.0, 1.0, or 3.0 w/w%). A printability index *Pr* is chosen as the response of interest and further compared against swelling and water uptake ratios. Eventually, the overall best performances were obtained for SA-CMC at $CaCl_2$ (30 mM + 1.0 w/w%), with a $Pr = 1.021$, swelling and water uptake ratios at 48h equal to 5.99 and 88%, respectively. Therefore, this work offers new insights over the control and optimization of the crosslinker concentration in the FRESH method.

4.3.1 Introduction

In the last decade, the multidisciplinary field of biofabrication drastically expanded due to the development of 3D (3D) bio-architectures (namely scaffolds), which closely resemble the complexity of human tissues for *in-vitro* disease modelling, TE, regenerative and personalized medicine[1]. Among biofabrication technologies, the class of AM techniques has played a central role due to its intrinsic flexibility, versality, wide range of accuracy and repeat-ability, over continuous improvement [2]. Compared to self-assembly biofabrication techniques, AM provides high 3D scaffold hierarchical organization and resolution, with variable stiffness to recapitulate the targeted tissue [3].

The main AM used for biofabrication include light-based technologies, dispending/extrusion (bio)printing, and jet-based printing [4,5]. Among them, syringe EBB is a well-known technique for the extrusion of hydrogels into filaments, with or without encapsulated living cells. Hydrogels are a class of biocompatible polymers with a high water content which can generate polymer networks composed of cross-linked chains, usually obtained with covalent bonds or cleavage reactions [6]. Since their biochemical composition and physical properties (such as viscoelasticity, degradability, etc.) can be controlled and fine-tuned, hydrogels are widely used as scaffolds for cellular seeding or as cell-laden constructs. The printability of such hydrogels is defined by the ability to generate a good 3D construct with high shape fidelity and repeatability [7]. Although soft and low viscous hydrogels are optimal in combination with specific tissues, such as neural and skin lineages, it is difficult to obtain a 3D printed construct without filament collapsing across the printed layers. In order to over-come such issue, several crosslinking approaches have been

proposed in the literature, resulting in photo-, thermo-, or chemical-responsive (bio)inks [8]. However, some of them can generate cytotoxic reactions when in contact with cells, resulting in an in-crease of cellular death or damage, such as DNA damage caused by an ultra-violet (UV) exposition or cellular death induced by photo-initiators.

Therefore, a complementary approach is to engineer an *in-situ* yield-stress support bath in which the print needle is free to move in each direction and the extruded hydrogel is cured when embedded, enabling to maintain its targeted 3D structure, without collapsing [9]. Since 2015, this printing approach is coined as Freeform Reversible Embedding of Suspended Hydrogels (FRESH) method. Such support bath is usually com-posed of a microparticle-based gelatin slurry containing a minimum amount of cross-linker, whose nature depends on the hydrogel chosen. This bath has a solid-like behaviour until its yield stress is reached by the movement of the print needle, thus it trans-lates to a liquid phase, allowing the extrusion of the ink. Afterwards, it returns to its solid state, encapsulating and curing the extruded material. Eventually, the 3D printed scaffold is extracted from the gelatin support by liquefying the latter at 37 °C for ca. 20 mins. Several examples of 3D FRESH printed hydrogels have been reported. Kreimendahl et al. [10] successfully investigated vascularization in 3D FRESH bioprinted fibrin (1.0 w/v%)-hyaluronic acid (0.5 w/v%) constructs with human endothelial cells and human dermal fibroblasts, each one at 3×10^6 cells/mL. The support bath was a commercial FRESH kit by Allevi, containing gelatin Type A, and calcium chloride ($CaCl_2$) at 11 mM and thrombin at 5 U/mL as crosslinkers. Jakub Lewicki et al. [11] 3D FRESH bioprinted human neuroblastoma cells at 1×10^7 cells/mL in a 2.0 w/v% of sodium alginate (SA), with a 83% of cell viability after 7 days, by using the Allevi's support bath with $CaCl_2$ at 10 mM. A post-process crosslinking was also applied with $CaCl_2$ at 10 mM for 20 mins.

However, according to the best authors' knowledge, no study has ever reported the use and effects over printability of gelatin-based FRESH support baths at different concentrations of pre- and post-process crosslinkers. Thus, due to their basic and broad use in several TE branches, this manuscript systematically investigates FRESH support baths at different concentrations of $CaCl_2$ for the 3D syringe-extrusion printing of two low viscous, soft SA – cellulose-based hydrogels. SA was selected as hydrogel base due to its vast use in TE and AM. SAs are natural polysaccharide-based polymers usually extracted from red or brown algae, bacteria, or seaweed. They have easy processability, fast gelation rate, affordable costs, good biocompatibility, good printability, and tunable mechanical properties which are source (or even batch) – dependent [12]. More-over, they contains blocks of (1,4)-linked β-D-mannuronate (M) and α-L-guluronate (G) units and are usually crosslinked with divalent cations (as $CaCl_2$) [13]. As additives, two low cost and easy processable cellulose-based derivates were chosen, that is carboxymethylcellulose (CMC) and micro-fibrillated cellulose (mFC). Cellulose is an abundant natural biopolymer usually obtained from plant source [14] and generally used in TE applications [15]. CMC is an anionic water-soluble polysaccharide derived naturally or through chemical reaction from cellulose, widely exploited in the food and cosmetic industry as rheology modifier [16]. It is a copolymer of β-d-glucopyranose 2-O-(carboxymethyl)-monosodium salt and β-d-glucose, linked by means of β-1,4-glyco-sidic bonds [17]. Instead, mFC is a cellulose-derived biomaterial obtained via a homogenization process and composed from tens of aggregates of long cellulose microfibrils with a diameter range from 20 to 60 nm and a length of several microns. It is formed by both amorphous and crystalline parts [18].

In this work, CMC and mFC are studied as separate additives for the 3D FRESH-printing of SA-based inks. The resulting hydrogels are systematically investigated by means of a design of

experiment (DOE) approach concerning their printing with different $CaCl_2$ concentrations in the bath and post-process crosslinking. As response of interest, a quantitative printability index *Pr* is chosen and further compared with swelling and water uptake ratios. The overall best performances are then reported and discussed. This work offers new interesting insights for the control and optimization of the FRESH method, with respect to the crosslinker concentration, in the vision of a BP process.

4.3.2 Materials and Methods

4.3.2.1 Inks and crosslinker preparation

Two inks were prepared for 3D FRESH print investigation. A low viscosity alginic acid sodium salt (SA, Thermo Fisher Scientific, IT) was dissolved at 8.0 w/w% in MilliQ water, in combination with an additive at 4.0 w/w% between sodium carboxymethyl cellulose (NaCMC) at a molecular weight M_{wNaCMC} = 90'000 Da (Sigma Aldrich, BE) and mFC (Belgium). The ratio selected between SA and the additives was 70:30. The two inks will be further referred as *SA-CMC* and *SA-mFC*, respectively. Each ink was stirred at 4.5 rpm for 40 mins at 70°C and then stored at 4°C. In the presence of aggregates, a spatula was used to mix the solution. Calcium chloride ($CaCl_2$, Thermo Fisher Scientific, IT) was selected as ionic crosslinker agent for SA. $CaCl_2$ was previously dissolved in MilliQ (room temperature) at 1.0 and 3.0 w/w%.

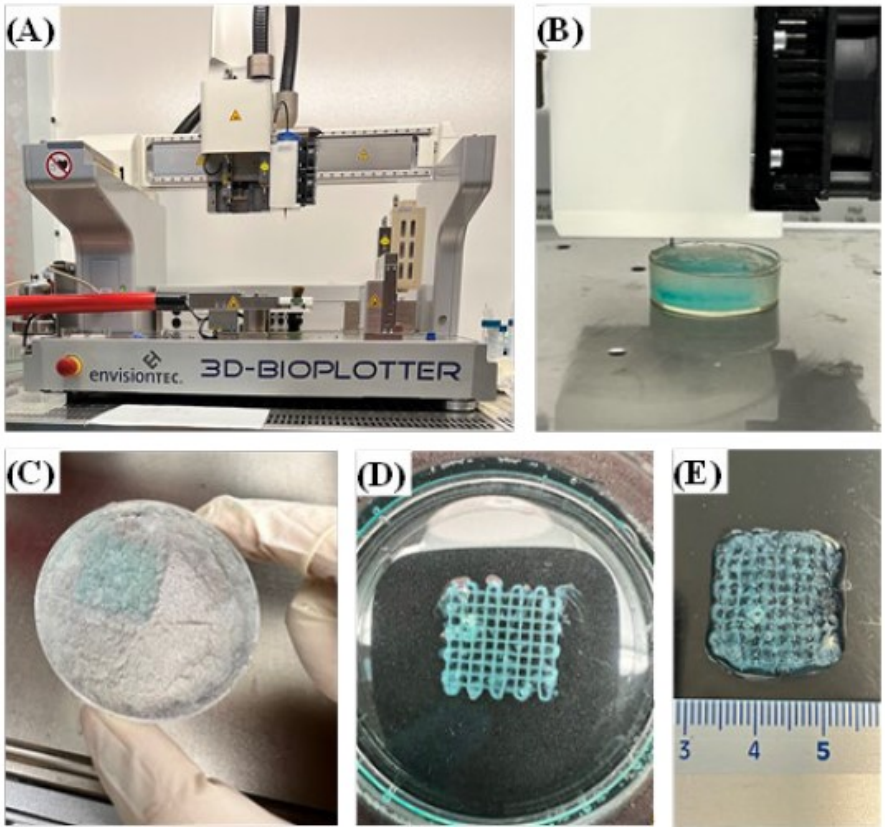

Fig. 1 Representative images of: (a) the 3D-Bioplotter system, (b) the 3D FRESH printing of a cellulose-based hydrogel (colored with blue for visualization) in the gelatin support bath, (c) the post-printing result, (d) the 3D printed construct after the gelatin release at 37 °C for 20 mins, and (e) the final 3D printed hydrogel, before drying.

4.3.2.2 Gelatin support bath preparation for FRESH 3D printing

Briefly, 4.5 w/v% of Gelatin Type A from porcine skin (Sigma-Aldrich, USA), and $CaCl_2$ at different concentrations of 10, 30, or 50 mM were dissolved in MilliQ water, and stirred at 40°C at 4.5 rpm for 20 mins. The solution was kept overnight at 4°C. Afterwards, the jellified mixture was poured in a 3-blade blender jar and filled with the $CaCl_2$ solution till the maximum capacity, and stored for 45 mins at -20°C until ice crystals formations were visible. Consecutively, the mixture was blended for 3 times at 30 s, each pulse with a break of 30 s to avoid heating the gelatin. Subsequently, the mixture was equally poured in 50 ml falcon tubes and centrifuged at 4°C and 3500 rpm for 2 mins for three times, until there was no visible supernatant foam. For each repetition, the supernatant was discarded and every falcon containing the gelatin slurry at the bottom was refilled with cold $CaCl_2$ solution and re-centrifuged. Finally, the gelatin slurry obtained was stored up to 2 weeks at 4°C.

4.3.2.3 Process study

Printing was conducted with a pneumatic extrusion 3D-Bioplotter system equipped with a low temperature print head (EnvisionTEC, Gmbh) (see Fig. 1a).

Table 1 Details of the experimental campaign performed for 3D FRESH printing of cellulose-based hydrogels.

3D FRESH printing parameters			
Parameters	**Values**		
Substrate	Petri dish, Ø 45 mm		
Needle diameter	21-gauge		
Stand-off distance *z* [mm]	0.46		
Print speed *s* [mm/sec]	30		
Control pressure *p* [bar]	1		
Number of layers *n* [#]	11		
Platen temperature *Tp* [°C]	5		
Print head temperature *Th* [°C]	10		
$CaCl_2$ in gelatin support bath [Mm]	10	30	50
Post-printing crosslinking $CaCl_2$ [w/w%]	0	1	3
Sample	Crosshatched mesh 20x20 mm, pore 2x2 mm		
Response	Printability index, *Pr* [#]		

Table 1 reports the experimental campaign executed at room temperature (22°C, 55% rh). A full factorial design of the type 2k ($k > 0$), with $k = 3$, was implemented for both the hydrogels. At least three samples were printed for each condition. The two factors used were the $CaCl_2$ concentrations i) in the gelatine bath (10, 30, or 50 mM) and ii) in the post-crosslinking process (0.0, 1.0, or 3.0 w/w%). The printability index, Pr [#], was chosen as the response of interest (see next section). Statistical analyses were performed using Minitab®. The inks were loaded into the print cartridge equipped with a 21-gauge precision stainless steel needle (Nordson, USA). Petri dishes were selected as reference substrate for print investigation and filled with the gelatin slurry

support bath at different $CaCl_2$ concentrations. The constructs were printed in the gelatin slurry as meshes of 20 x 20 mm, rotated at 90° each print level, with squared pores of 2 x 2 mm (see Fig. 1b and c). Afterwards, each construct embedded in the gelatin support bath was drop-by-drop crosslinked with 1.5 ml of $CaCl_2$, and kept for 20 mins on a stirrer at 40°C in order to allow the gelatin to liquefy, as shown in Fig. 1d and e. Subsequently, the constructs were washed with 1.5 ml of MilliQ water and kept at 4°C.

4.3.2.4 3D printed constructs characterization

Shape fidelity

In order to assess the geometrical accuracy of the printed meshes, optical images were processed with the ImageJ software. The circularity (C) of the pores and Pr were calculated according to the formulas given by Ouyang et al. [7]:

$$Pr = \frac{\pi}{4}\frac{1}{C} = \frac{L^2}{16A}, with\ C = \frac{4\pi A}{L^2} \quad (1)$$

where L [mm] is the perimeter and A [mm^2] the area of the pores, respectively. This means that, in an ideal condition of hydrogel gelation and printability, each pore of the printed mesh is equal to the CAD design (a square of 2 x 2 mm), thus $C = \frac{\pi}{4}$ and $Pr = 1$. In over-gelation or under-gelation conditions, the index will be $Pr > 1$ (irregular shape) or $Pr < 1$ (similar to a circular shape) respectively. For each mesh, the central area of 1 x 1 cm was analyzed by the software ImageJ, for a total of 25 pores each mesh (75 data points for each condition). Afterwards, the average μ [mm] and standard deviation σ values within each print condition were calculated and statistically analyzed.

Swelling ratio and uptake water

3D FRESH printed meshes with a Pr ~ 1 for both hydrogels, that is at $CaCl_2$ (30 mM, 1.0 and 3.0 w/w%), were selected for swelling ratio and water uptake analyses. The meshes were printed with the same parameters reported in Table 1. The resulting meshes were dried at 40 °C overnight in a thermal oven and later at 65 °C for 30 mins. After their dry weight (W_d) was recorded, the samples were incubated at 37 °C in a phosphate buffered saline solution (PBS; pH 7.4, Sigma Aldrich). Each mesh was weighed (W_s) at specific time points (0, 1, 1.5, 24, and 48 h), with the first weight equal to W_d. For every weighing, the swollen meshes were taken out from PBS, laid down on a filter paper for 10 s (in order to absorb the excess of PBS), and then weighed (at least 2 replicas each). The swelling ratio and the water uptake indexes were calculated as follows [19].

$$Swelling\ ratio\ index = \frac{(W_s - W_d)}{W_d} \quad (2)$$

$$Water\ uptake\ index = \frac{(W_s - W_d)}{W_s} \times 100 \quad (3)$$

4.3.3 Result and discussion

Fig. 2 reports optical images of SA-CMC and SA-mFC meshes, 3D FRESH printed at different concentrations of the crosslinker $CaCl_2$ in the gelatin bath (10, 30, and 50 mM) and in the post-printing process (0.0, 1.0, and 3.0 w/w%). In both of the hydrogels, it is clearly noticeable a change in the pore geometry (from undetectable to clogged, till well-defined edges) and size, as the $CaCl_2$ concentration in both the gelatin bath and the post-printing process increases. Indeed, the higher $CaCl_2$ concentration, the higher is the formation of crosslinks between SA and Ca^{2+} ions.

In addition, Fig. 3 and 4 show the *Pr* mean indexes and the main effect plots with respect to *Pr* mean values on SA-CMC and SA-mFC printed hydrogels, respec-tively. For both the hydrogels and in any condition, *Pr* is always < 1.25 (Fig. 3). In the case of SA-CMC, the *Pr* index directly increases with an increment of $CaCl_2$ for both factors (Fig. 4a).

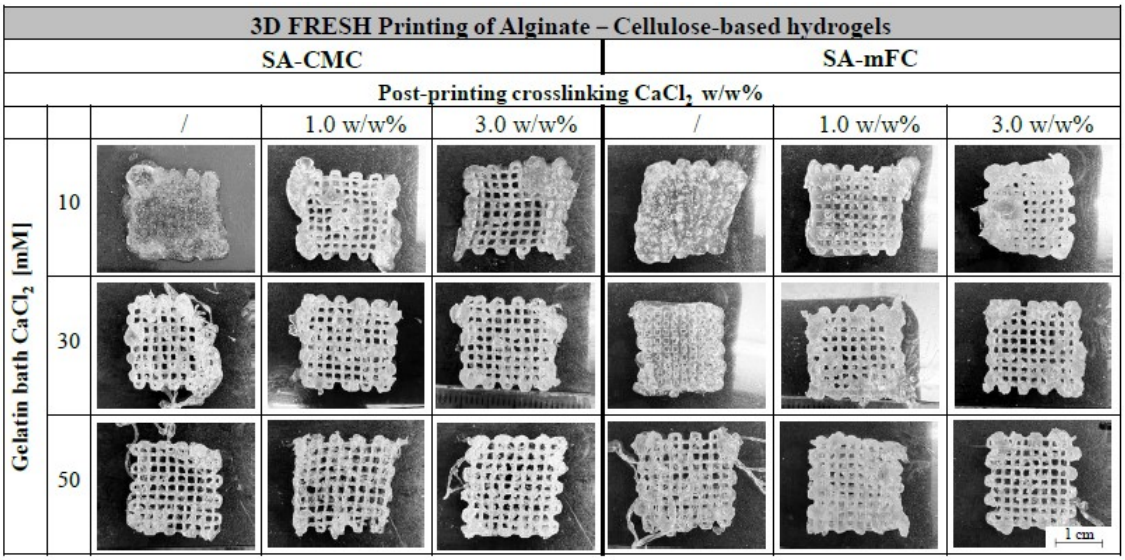

Fig. 2 Representative optical images of alginate – cellulose-based hydrogels (SA-CMC and SA-mFC) fabricated by 3D FRESH printing in a gelatin slurry at 10, 30, or 50 mM of $CaCl_2$ and post-process ionic crosslinking ($CaCl_2$) at 0.0, 1.0, and 3.0 w/w%.

A similar trend is visible for SA-mFC, despite the condition $CaCl_2$ at 3.0 w/w%, which has a general decline of *Pr*, as reported in Fig. 4b. In general, the *Pr* indexes of SA-CMC face more fluctuations, while the ones referred to SA-mFC are more narrowed towards *Pr* = 1. This is probably caused by a better ability of mFC chains to form interpenetrating polymeric networks with SA. It has to be noted that these observations are related to the top visible printed layers, hence more analyses must be performed in the future to validate this statement.

As shown in Fig. 2 and 3, starting from the lowest concentrations of $CaCl_2$ (10 mM + 0.0 w/w%), no pores are detected in both hydrogel compositions, resulting in a *Pr* < 0.45, with a more evident effect on SA-mFC, which does not present any open pore. At $CaCl_2$ (10mM + 1.0 w/w% and 3.0 w/w%), pores start being visible due to the post-crosslinking effect on the SA polymer chains. However, most of the pores are still clogged at random irregular patterns (especially at the edges) for SA-CMC. A *Pr* = 0.776 for $CaCl_2$ (10mM + 1.0 w/w%) and a *Pr* = 1.135 for $CaCl_2$ (10mM +

3.0 w/w%), that is under and over gelation respectively, are indeed obtained (Fig. 3a). Instead, a *Pr* = 0.991 is got at $CaCl_2$ (10mM + 1.0 w/w%) for SA-mFC (Fig. 3b).

At $CaCl_2$ (30 mM + 0.0 w/w%), SA-CMC presents visible pores but also detached filaments, compared to SA-mFC in which even if the geometry of the pores is detectable, they are still clogged. The filaments present in SA-CMC samples are the result of a fast crosslinking of the extruded material into the gelatin slurry, thus not allowing a proper surface attachment between the printed layers. With an increment in the post-process crosslinking treatment, a *Pr* = 1.021 is obtained in the condition $CaCl_2$ (30 mM + 1.0 w/w%) for SA-CMC, while a *Pr* =1.068 at $CaCl_2$ (30 mM + 3.0 w/w%) for SA-mFC (Fig. 3). Being the $CaCl_2$ time of 20 mins considered moderately long, crosslinked sites are indeed allowed to be generated in the core and surface of the printed layers.

Similarly to $CaCl_2$ (30 mM + 0.0 w/w%), detached filaments are visible and randomly present across the printed layers at $CaCl_2$ (50 mM). In these conditions, since the amount of $CaCl_2$ in the bath is almost double than the previous case, the extruded printed layers crosslink too fast, generally resulting in irregular pores (*Pr* > 1). The best *Pr* indexes are detected at $CaCl_2$ (50 mM + 1.0 w/w%), specifically *Pr* = 0.971 for SA-CMC, and *Pr* = 1.033 for SA-mFC (Fig. 3).

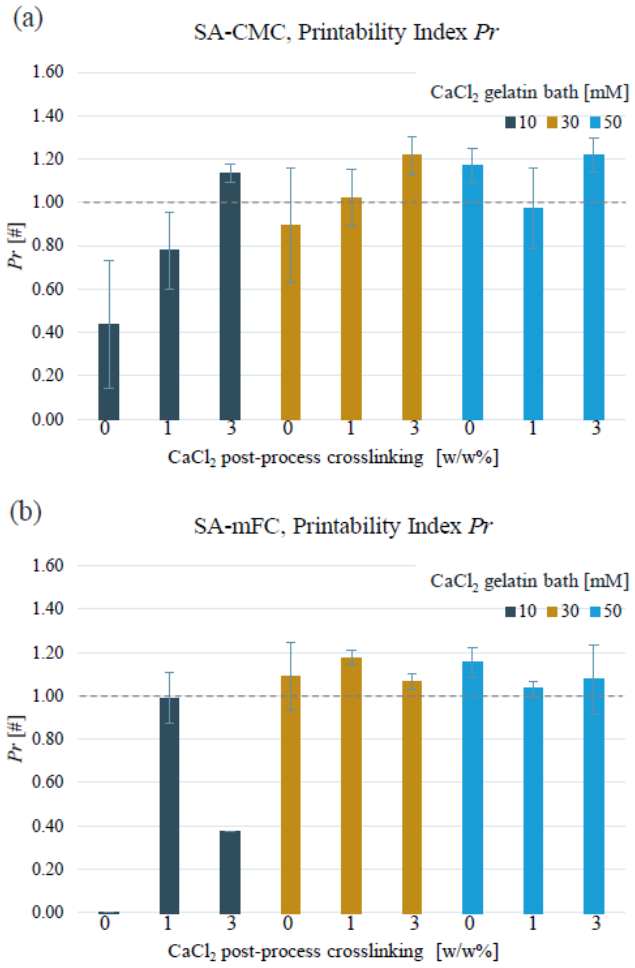

Fig. 3 Printability indexes *Pr* of 3D FRESH printed alginate – cellulose-based hydrogels, that is (a) SA-CMC and (b) SA-mFC, at the different conditions of $CaCl_2$.

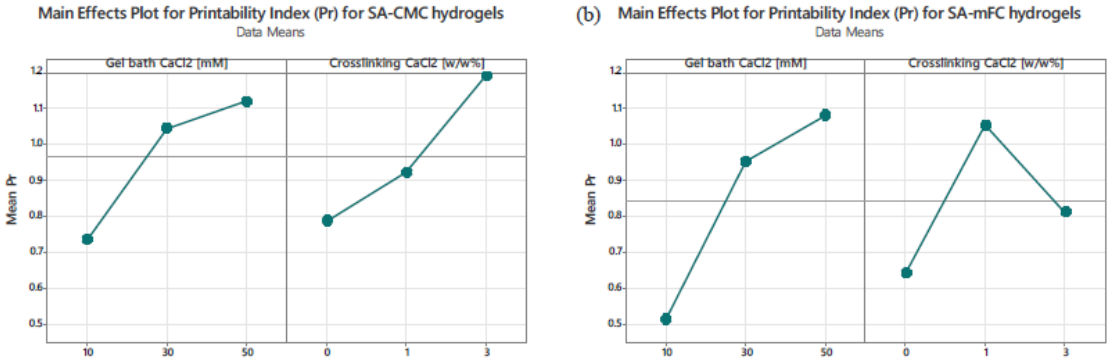

Fig. 4 Main effects plot for printability index *Pr* of 3D FRESH printed (a) SA-CMC and (b) SA-mFC hydrogels, against $CaCl_2$ concentration in the gelatin bath and in the post-crosslinking process.

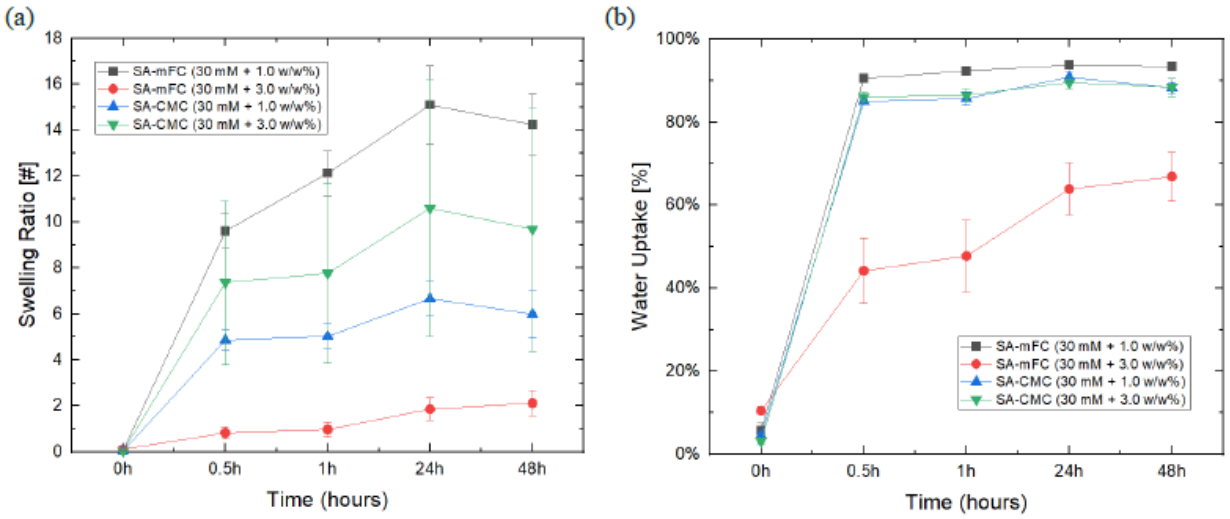

Fig. 5 Swelling ratio and uptake water percentages of 3D FRESH printed cellulose-based hydrogels in a gelatin slurry at 30 mM of $CaCl_2$ and post-process ionic crosslinking ($CaCl_2$) at 1.0, and 3.0 w/w%.

In conclusion, the nearest values of *Pr* to 1 are obtained for SA-CMC at $CaCl_2$ (30 mM + 1.0 w/w%, *Pr* = 1.021), while in multiple conditions for SA-mFC, that is $CaCl_2$ (10 mM + 1.0 w/w%, Pr = 0.991), (30 mM + 3.0 w/w%, *Pr* = 1.068), and (50 mM + 1.0 w/w%, *Pr* = 1.033). For this reason, the conditions $CaCl_2$ (30 mM + 1.0 w/w% and 3.0 w/w%) were selected for swelling ratio (Fig. 5a) and water uptake (Fig. 5b) analyses. As shown in Fig. 5, there are differences in the ratios between the additives CMC and mFC. In general, CMC and mFC are prone to swell due to their hydrophilic surface (high surface area), prompt to water absorption [20]. However, at 48h, SA-mFC (30 mM + 1.0 w/w%) has the highest swelling ratio up to 14.24 and water uptake equal to 93%, while SA-mFC (30 mM + 3.0 w/w%) the lowest one at 2.12, with a water uptake of 67%. In line with the literature [21], the crosslinking degree increases along with an increase in the concentration of $CaCl_2$ (in this case the post-process crosslinking from 1.0 to 3.0 w/w%), allowing the generation of more bonds among the molecules, thus reducing the ability of the printed mesh to swollen up. However, strong crosslinking bonds are also known to reduce cellular migration in a BP process [22]. Therefore, high swelling and water uptake ratios are preferable. A similar trend is pre-sent for SA-CMC meshes (swelling ratios between 5.99 and 9.70 at 48h) although less

evident than SA-mFC, especially for the water uptake indexes (almost 88% in both cases, at 48h). This demonstrates a higher ability of CMC for water retention compared to mFC, due to hydroxyl and carboxyl groups available for the formation of hydrogen bonds with water molecules [23].
Based on all the investigations performed of *Pr*, swelling ratio and water uptake, SA-CMC (30 mM + 1.0 w/w%) shows the overall best performances. A trade-off among the indexes must be taken for SA-mFC, favoring the condition SA-mFC (30 mM + 3.0 w/w%) for the Pr index, while SA-mFC (30 mM + 1.0 w/w%) for the others.

4.3.4 Conclusion and Future perspectives

3D FRESH printing is an emerging technique of the syringe-extrusion type, for the (bio)printing of soft hydrogels, which could not otherwise withstand their shape during printing. This technique can be used with any soft hydrogel which can be chemically crosslinked, provided there is no chemical and physical reaction with the gelatin bath.
The present study investigated the 3D FRESH printing in a gelatin bath for alginate–cellulose-based hydrogels. Particularly, two cellulose derivates, that is CMC and mFC, are combined with SA and systematically investigated at different conditions of $CaCl_2$ concentration in the bath (10, 30 and 50 mM) and in the post-crosslinking process (0.0, 1.0, and 3.0 w/w%), according to a full-factorial design. To the best authors' knowledge, this is the first paper which studies and analyses different and combined pre-crosslinking and post-process crosslinking conditions using a 3D FRESH printing method. A printability index *Pr* is chosen as the response of interest in order to quantitively analyze the printed samples, and further compared with the results of swelling and water uptake ratios. The selected *Pr* considers the gelation and printability of the samples based on the pore shape, with the ideal condition equal to a square shape, that is $Pr = 1$. Results obtained show the best overall performances for SA-CMC at $CaCl_2$ (30 mM + 1.0 w/w%), with a $Pr = 1.021$, swelling ratio and water uptake at 48h equal to 5.99 and 88%, respectively. Instead, a trade-off among the indexes must be considered for SA-mFC, which resulted in multiple optimal conditions for the *Pr* index, while $CaCl_2$ (30 mM + 1.0 w/w%, Pr = 1.177) for the others, with a swelling ratio and water uptake at 48h equal to 14.24 and 93%, respectively. A more comprehensive variable than *Pr*, which also includes the uniformity of the printed filaments of the meshes in the x and y directions and their CAD fidelity, will be part of future investigations. Future studies will also focus on mechanical characterization of the printed meshes, along with cellular adhesion and proliferation analyses.

4.4 Bioprinting of Alginate/Gelatin hydrogel: Cell metabolic activity and proliferation response

TE has had a huge development in the last years, especially due to AM technologies, and the combination of biomaterials and cells, that constitute 3D cell printing. This powerful technology makes it possible to create complex structures, with different components and characteristics, to be used in biomedical applications. Nevertheless, there are still several challenges to overcome for adequate 3D printed structures, in particular the optimization of the biomaterial according to biocompatibility and printability requirements. Hydrogels are among the most interesting biomaterials, because they mimic the natural extracellular matrix and can create a highly hydrated environment, promoting cell attachment and proliferation; however, they have weak mechanical properties that are hard to control, making it challenging to print a proper 3D structure. In this research, hydrogels based on alginate and gelatin are tested due to the osmotic requirements of the cells for their viability, and the possibility to combine temperature and chemical crosslinking. Different compositions (%w/v) are tested (8% gel-7% alg, 4% gel-4% alg, 4% gel-2% alg), in order to obtain a hydrogel able to produce a 3D structure up to 10.3 ± 1.4 mm; after loading with MS5 cells, cell viability is evaluated by implementing the live/dead staining with the analysis of the cellular metabolic activity through ATP assay. The goal of this paper is to develop a biomaterial that combines printability and the ability to encapsulate cells, while also maintaining cell viability after the printing phase.

4.4.1 Introduction

BP is a pioneering technology for the fabrication of biomimetic tissue constructs, expected to provide an effective solution to the long-standing shortage of tissues/organs for transplants [1,2]. This technique is also used to produce devices loaded with cells in order to study their behaviour in certain scenarios, such as their reaction to drugs [3,4].

Two-dimensional models do not reproduce human physiological conditions faithfully; therefore, it is preferable to use 3D tissue models to provide cells with mechanical stimuli, derived from cell-to-cell and cell-to-matrix contact. Among the available technologies to produce structures for 3D cell cultures, 3D cell printing is one of the most innovative. 3D printing mainly consists of four different techniques: laser-assisted, stereolithography-based, jetting-based, and extrusion printing systems [5]. Extrusion-based cell printing exploits a syringe filled with a cell-loaded hydrogel, usually a hydrogel. Encapsulating cellular components in flowable and biocompatible hydrogel also allows to prevent cellular damage from shear forces during the extrusion process [6–9]. The printing head movements in x, y and z allow the deposition of the hydrogel along a 3D structure. Although the resolution of extrusion-based cell printing is lower than laser or inkjet-based cell printing (~200 μm), this method can produce 3D tissue-mimetic structures easily and very quickly, with limited damage to cell viability or functionality. Moreover, this technique allows the extrusion of a wide range of hydrogel, or hydrogels, with different viscosities [10].

When producing a cell-laden printable hydrogel, some important aspects are to be considered: biocompatibility, printability, and mechanical and structural integrity [5,11]. Hydrogels with high printability generally have a high viscosity or crosslinking density, which can lead to reduced biological properties. Moreover, hydrogels with good biofunctionality (*i.e.*, excellent cell

proliferation, differentiation, and maturation) can lead to less printability potential. The optimal result is a hydrogel capable to keep the printed shape and to promote biological activity [12].
Thermoplastic polymers, along with other materials, have been widely applied to fabricate supporting frameworks to engineer clinically relevant and mechanically robust tissues, including bone and cartilage [10]. Both synthetic and natural polymers are widely used to produce hydrogels. Although synthetic hydrogels show high mechanical stability and fast polymerisation, they are not suitable to host cells because of the lack of cell-binding moieties. On the other hand, natural polymers cannot keep a 3D shape without crosslinking. Among natural polymers, Gelatin and Alginate are the most commonly used to produce hydrogels [13–15].Gelatin is a natural polymer, which has been widely used in the field of biomedical applications due to its biomimicking and biodegradable properties [16]; it is derived from collagen via acidic (type A) or basic (type B) hydrolysis, thus it is relatively easy to obtain in large quantities from animal sources (*e.g.*, bones, tendons, or skin) as compared to pure collagen. This material has a thermo-reversible gelation behaviour in response to the surrounding temperature, which makes it particularly attractive as a hydrogel. Due to this property, cell-laden gelatin can easily build up the desired 3D structure by regulating temperature and concentration. In addition, gelatin has cell-responsive properties, such as the arginine-glycine-aspartate (RGD) peptide as a cell binding motif and matrix metalloproteinase (MMP) recognition sequences for degradation. However, while gelatin is advantageous for BP, it offers insufficient structural stability due to its low mechanical strength and high temperature sensitivity. Chemical cross-linking (*e.g.*, methacrylation, resulting in cross-linking via UV) can overcome these limitations and support fabricated structures for a long time under various physiological conditions [12]. An interesting discovery, found in literature, shows that gelatin-based scaffolds can increase the retention of transplanted cells in the ischemic myocardium and improve cardiac function [16], validating the use of such material in biological applications. However, the weak mechanical strength of gelatin needs to be improved by adding other polymers to form composite hydrogels.
Alginate, which is refined from brown seaweed [17], is one of the most preferable natural polymers to produce hydrogels, owing to its relatively low toxicity, relatively low price, and wide applicability in various printing techniques [12]. In nature, this material forms tough but flexible structures and can create a hydrogel: due to these characteristics, it is common knowledge that it can be used to thicken and stabilise mixtures [17]. Alginate-based hydrogels have been applied to engineer a variety of tissues, such as bone, cartilage, and adipose tissues. To facilitate tissue formation, it has been widely used as a hydrogel for EBB because it can be instantly polymerized by mixing it with multivalent cations during the printing process [5]. This material, unlike gelatin, lacks cell-responsive properties, so cells tend to aggregate in clusters when only alginate is used as scaffold [17]. Usually, alginate is blended with other polymers to ensure its biological functionality. Another approach is the introduction of bioactive molecules (*e.g.*, peptides) into the alginate backbone before printing, to improve its functionality. In addition, to further improve mechanical properties and structural stability, chemical cross-linking (such as methacrylation and thiolation) is also used [12]. On the other hand, alginate biodegrades when in contact with bodily fluids, due to the exchange reaction with monovalent cations: this feature makes it appealing in TE, because it makes possible to control the degradation rate [17].
The blend of alginate and gelatin to create a hydrogel is considered a good scaffold for 3D cell culture because of its non-toxicity, biodegradability, and biocompatibility; furthermore, this kind of hydrogel is a good option for 3D printing at room temperature [18].

Generally, in literature cell viability after 3D printing is estimated using only the live-dead imaging staining [10,11,13,19–24]. Conversely, the use of different methods in parallel, which take in consideration different cell properties (*i.e.*, morphology, metabolic activity, proliferative capacity, etc.), would hopefully provide a more accurate description of 3D structures and of their impact on cell survival and behavior, as described in [25].
The present work aims at the production of a cell-laden printed gelatin/alginate composite hydrogel to be evaluated by different biocompatibility tests to obtain a 3D structure that assures a good level of cell activity during and after printing. To do this, hydrogels produced using gelatin and alginate have been investigated in terms of both printability and biocompatibility; the percentages (w/v) of the two natural polymers, in this work, were kept similar in each hydrogel because previous studies concluded that, by doing so, the printing stability resulted better than the one observed for of hydrogels with higher percentages differences in the amounts of alginate and gelatin [26]; moreover, in literature [14,27–29], similar hydrogels were considered but cell viability was estimated only qualitatively. Generally, to study cell behavior in 3D, low heights are considered; in this paper, structures up to 10.3 ± 1.4 mm have been produced, and cell viability has been evaluated by implementing the classical live/dead staining with cell morphology assessment and with the quantitation of the cellular metabolic activity through the adenosine triphosphate (ATP) assay, an integrative approach that is often lacking in the literature on the topic. In this study, a dependency between medium viscosity and cell metabolic activity, buy not viability, was also highlighted.

4.4.2 Materials and Methods

4.4.2.1 Hydrogel preparation

Gelatin (Gelatin from porcine skin type A, 300 Bloom, Sigma Aldrich, Saint Louis, MO), alginate (Alginic sodium salt, 120,000-190,000 g/mol, Sigma Aldrich), distilled water (milliQ), and Iscove's Modified Dulbecco's Medium (IMDM powder, Gibco™, Thermo Fisher Scientific, Waltham, MA) were combined to produce the hydrogels. Specifically, milliQ water and alginate were added and mixed in a graduated cylinder; gelatin was then added and mixed to the other components. The cylinder has then been autoclaved at 121°C for 30 minutes, in order to make the mix homogenous and sterile. Finally, 5 mL of IMDM 10X and a proper amount of milliQ water were added when the temperature decreased, to reach the volume of 50 mL. At that point, the hydrogel was ready to be transferred into syringes for the printing tests. The tested compositions (%w/v), listed in Table 1, were G8A7 (8% gelatin 7% alginate), G4A4 (4% gelatin 4% alginate), G4A2 (4% gelatin 2% alginate).

Table 1 Percentages of gelatin and alginate in each hydrogel and tested process parameters.

	Gel	**Alg**	**P (bar)**	**V (mm/s)**	**Printing T (°C)**
G8A7	8%	7%	0.7-1.8	10-30	20
G4A4	4%	4%	0.8-1	20-30	10
G4A2	4%	2%	0.8-1	20-30	10

4.4.2.2 Preliminary test

The printing protocol followed for the printability tests was carried out on hydrogels without cells and consist of three phases: best ink composition investigation (Fig. 1a and as illustrated in [26]), crosslinking method definition (Fig. 1b), and 3D structures printing (Fig. 1c).
The 3D BIOPLOTTER (Envisiontec ©, Gladbeck, Germany) was used to perform the printing. Printing parameters (i.e.: speed, pressure, temperature) (Fig. 1a), and crosslinking methods (Fig. 1b) were varied in the process. A set of experiments of single filament printing was carried out to determine the ideal hydrogel composition. Single filament printing enables a qualitative and quantitative evaluation of the printability, leading to the definition of the optimum parameters. The experiments involved parameter tuning by printing filaments at various pressure, speed, and temperature values.
Following the filaments printing, different grids consisting of a 30 mm x 30 mm square, with 6 mm of distance between the long parallel lines, were printed to test two crosslinking procedures. The grids replica used for this evaluation were printed with the following parameters: pressure of 2.3 bar, offset of 0.45 mm, nozzle diameter of 0.61 mm, and speed of 30 mm/s. In the first scenario, the crosslinking took place during the printing process, in a bath of 3% $CaCl_2$ solution, while in the second one the same solution was spread on the hydrogel after printing and left on for three minutes. While printing, in both cases, the hydrogel was combined with a blue edible dye in order to make the printed geometry visible (Fig. 2 a,b).

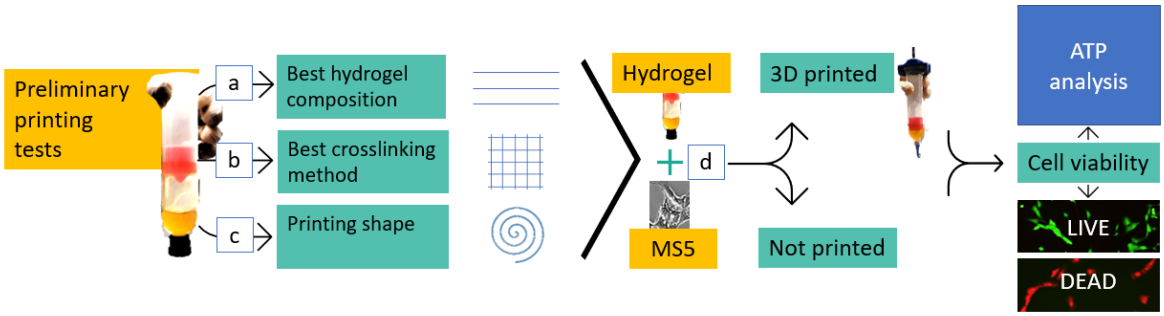

Fig. 1 Workflow. Once the hydrogel was produced, three main preliminary printing tests were carried out to define the best ink composition, the best crosslinking method, and if it was possible to print a shape with the investigated hydrogels. The next step consisted in combining the hydrogel with cells (MS5). The mixtures were analysed plane (not printed) and after the 3D cell printing process. Cell morphology was assessed, and cell viability was tested by using both the live/dead staining and the ATP assay.

Subsequently, a more complex shape (Fig. 1c) was printed, with the aim of building a stable 3D structure. The chosen geometry was a spiral, designed as 3.5 revolutions inscribed in a 20 mm diameter circumference (Fig. 2g), with thickness and height of 0.5 and 10 mm, respectively. The spiral shape was chosen to evaluate both the hydrogel printability, since it is a 3D complex geometry, and the biocompatibility. Since the main aim of this experiment was to guarantee cellular survival after printing, such geometry, with a higher surface ratio, can assure a bigger exchange of nutrients, oxygen, and other supplements to maintain cell viability and functionality. The parameters investigated were speed (20-40 mm/s), pressure (0.7-1.8 bar) and temperature (10-25°C), with offset set at 0.35 mm and a nozzle diameter of 0.41 mm. The spirals printing (Fig. 1c) took place using different temperatures: 20°C for G8A7, and 10°C for G4A4 and G4A2;

details about the other tested parameters are presented in Table 1. The structure was considered stable and acceptable when reaching 15 layers without collapsing.

4.4.2.3 Viscosity analyses

Viscosity analyses were carried out, using the VISCOTM 6800 (ATAGO CO., LTD. Tokyo, Japan). Spindle (A1, A2, A3) and beaker (small S) were selected for each experiment, according to the measurable range. All the samples were heated to a temperature of 45°C and then cooled down to 23°C, then poured in the beaker, avoiding air inclusion. Once the hydrogel reached 20°C, the measurement process started. The data were collected using the software Tera Term (Tera Term Project). For each angular velocity, the 10 central measurements were considered for G8A7 and the 20 central measurements for G4A4 and G4A2. More details about the parameters used in each test are presented in Table 2. The tests were carried out at room temperature.

Table 2 Parameters set in viscosity tests.

	Spindle-beaker	**RPM**
G8A7	A3S	0.2-0.5-2-2.5-3-4-5
G4A4	A2S	3-4-5-6-10-12-20
G4A2	A1S	30-50-60-100-150-200-250

The viscometer registers a viscosity value (mPa*s) at each turn. The standard deviation was calculated for each speed value. Given the beaker inner diameter (DB), the spindle external diameter (DS), and the angular speed in radiant (ω), the shear rate is obtained thanks to the below-reported function:

$$Shear\ rate\ [s^{-1}] = 2\frac{D_B^2}{D_B^2 - D_s^2} * \omega$$

4.4.2.4 Cell preparations for hydrogel loading

MS5 murine stromal cells were cultured in DMEM medium (Euroclone, Milan, Italy), supplemented with 10% fetal bovine serum (FBS, Euroclone), 1% penicillin/streptomycin (Euroclone), and 1% L-glutamine (Euroclone), at 37°C, 5% CO2 in a humidified incubator. When reaching confluence, cells were detached using trypsin-EDTA (Euroclone).
For the incorporation in the hydrogel at a density of 4x105 cells/mL, cells were counted and centrifuged in a sterile tube.
The pellet was dried and dislodged; then, the hydrogel mixture was gently added to the dry pellet by making it slide down the side of the tube. The cell suspension was homogeneously mixed by gently inverting the tube, and briefly spun down in a centrifuge.
Part of the cell-loaded hydrogel was poured in the 3D BIOPLOTTER (Envisiontec ©, Gladbeck, Germany) with a sterile cartridge OPTIMUM CLASS VI, 30 cc (Nordson, Westlake, OH); the printing of cell-laden hydrogels was carried out using pressure values below 1 bar (0.8 bar) to preserve cell viability.
To set the non-printed control, part of the cell-loaded hydrogel was aliquoted in the wells of a 24-well plate, 500 µL/well, crosslinked with 3% $CaCl_2$ for 3 min, and washed twice with DMEM to

remove all the traces of $CaCl_2$. As a further control, an equal number of cells was seeded in a 24-well plate in the traditional 2D culture conditions. Both printed and non-printed cell-loaded hydrogels, as well as 2D culture cells, have been maintained in culture in DMEM medium supplemented as described before. Cells were observed and pictures were taken with an inverted optical microscope (EVOS™ XL, Thermo Fisher Scientific) to assess cell morphology.

4.4.2.5 Biocompatibility

Cell viability was assessed by two different assays: Live/Dead assay and ATP cell viability luciferase assay [30–33].

For the Live/Dead assay, the LIVE/DEAD™ cell imaging kit (488/570) by Thermo Fisher Scientific was used. The kit consists of two components: Calcein AM stains live cells in green, while BOBO-3 iodide stains dead cells in red. The vial with dried BOBO-3 iodide must be resuspended with the vial with calcein AM to obtain a 2X mix. A small slice of both printed and non-printed hydrogels was cut with a sterile scalpel and moved into a centrifuge tube, where it was incubated with complete DMEM and Live/Dead in 1:1 proportion for 15 min at room temperature in the dark. The assay robustness was verified on a control of dead cells (MS5 cells fixed in 100% ethanol for 2 minutes) and a control of live cells (unfixed MS5 cells), that appeared red and green, respectively.

The hydrogel slice was then flattened between a glass coverslip and a microscope slide and observed under a fluorescence microscope (Olympus IX70, Olympus, Tokyo, Japan). Images from at least 5 fields were taken using Image-Pro Plus software v7.0 (Media Cybernetics, Rockville, MD).

For the ATP cell viability luciferase assay, the CellTiter Glo® 3D cell viability assay (Promega, Madison, WI) was used. The assay takes advantage of the ATP produced by living, metabolically active cells to catalyze luciferase-mediated luciferin oxidation, which results in photon emission. After culture medium removal, cell-loaded printed and non-printed hydrogels (500 µL/specimen) were incubated with 500 µL of the kit substrate for 20 min at room temperature in the dark. During the incubation, the hydrogel was mechanically broken by repeated pipetting and smashing with a syringe plunger to allow cell lysis; the substrate itself contained a lysing reagent optimized for 3D structures. As a positive and a negative control, cells in 2D cultures and the hydrogel without cells were assayed as well. A standard curve was prepared by standard ATP serial dilutions. After the incubation, the mix was moved to a black 96-well plate (BRAND, Wertheim and Großostheim, Germany) for the analysis: for each sample, three replicate wells were set (150 µL/well). After an additional 10 min incubation for bubble removal, the luminescence signal was acquired with a M200 microplate reader (Tecan, Männedorf Switzerland). The analyzed timepoints were: t0 (non-printed only), 3h, 24h, 72h, and 7 days. The mean was calculated from the three replicate wells, the signal from the empty hydrogel was subtracted, and the absolute ATP concentration was calculated from the standard curve equation. Data were expressed as percentages of the signal from cells in 2D culture at t0.

4.4.2.6 Statistical analysis

The statistical tests were carried out for all data presented. Specifically:

- to verify if the different percentages of gelatin and alginate had any effect on the measurements of diameter and z height of the samples, single-factor analysis of variance (ANOVA) tests were performed. This analysis was used to confirm any statistical

significance within samples and to determine repeatability. Statistical analysis was conducted at α = 0.05 using Minitab 18® (MINITAB, Brandon Court Unit E1-E2, Progress Way, Coventry CV3 2TE, UK).

- GraphPad Prism (San Diego, CA) was used to perform comparisons between groups by Student's t-test for data from biological experimental replicates. The number of experimental replicates and the p-values are reported in the individual figure legends.

All presented data are expressed as mean ± standard deviation, and *p*-values < 0.05 were considered statistically significant.

4.4.3 Result and discussion

4.4.3.1 Preliminary printability tests

The first step of the printability tests was to produce well defined filaments, essential to have the final shape fidelity [34]. The results demonstrated that the G8A7 showed the best printability in comparison to the other hydrogels. The filaments were well defined and with smooth surfaces but on the other hand, needed higher pressure to be extruded. The G4A4 and G4A2 produced defined filaments with a not entirely smooth surfaces, but requiring lower pressure values, more suitable for the 3D cell printing applications.

The comparison between the crosslinking in bath (Fig. 2a) and post printing (Fig. 2b) reveals that, when printed in the bath, the grid's hydrogel filaments showed poor adhesion, as visible from Fig. 2a. This effect is caused by the presence of alginate that immediately crosslinks with the $CaCl_2$, thus the crosslinked filament surface does not stick to the printing substrate.

So, to allow the correct filament deposition (layer-by-layer, with shape fidelity), the chosen method was printing on a dry slide with a fixed temperature and crosslinking after printing. Gelatin sets under 25°C, so the temperature control allows the gelation of the hydrogel during the printing phase, also for the hydrogel with a reduce amount of gelatin.

The previous step demonstrated that the printing of complex geometries with this type of hydrogels was feasible on a dry surface, so a new shape was considered: a spiral-shaped structure. During the experimental tests, this geometry showed geometric stability when printing, as a result of continuous filament printing opposed to the traditional start-and-stop geometry of grids with different patterns. In fact, in the case of grids printing, due to the many stops and starts, the filaments are not continuous, and the resulting layers are uneven, affecting the final geometry. The discontinuities inside the layer are also crucial for cell survival because they can interfere with the nutrients exchange surface, as explained above.

Fig. 2f shows a representation of the printed spirals; the set parameters were pressure 1.8 bar and speed 20 mm/s at 20°C for G8A7; pressure 1 bar and speed 20 mm/s at 10°C for G4A4; pressure 0.8 bar and speed 20 mm/s at 10°C for G4A2. The offset was kept at 0.35 mm for all the spirals represented in Fig. 2. The measurements of z height and diameter showed how the amount of gelatin affects the stability during the printing phase (Fig. 2c, d, and e). G8A7 has higher percentage of gelatin, so it is printable at higher temperatures then the other hydrogels with lower amount of this component, 4% w/v. This condition guarantees higher stability of the sample; in particular, the number of layers can rise, and the z too. The trend of the diameter is inversely proportional to the gelatin percentage. G4A2 and G4A4 hydrogels were more soft during the printing phase, so the diameter of the printed structures tends to widen due to the load of the upper printed layers.

The results indicate that the G8A7 hydrogel can be printed more successfully in terms of structural integrity, but in order to be used in 3D cell printing, the hydrogel needs to combine certain rheological and biological properties. In this regard, hydrogels G4A4 and G4A2 showed better features, as viscosity analysis and biocompatibility tests can demonstrate.

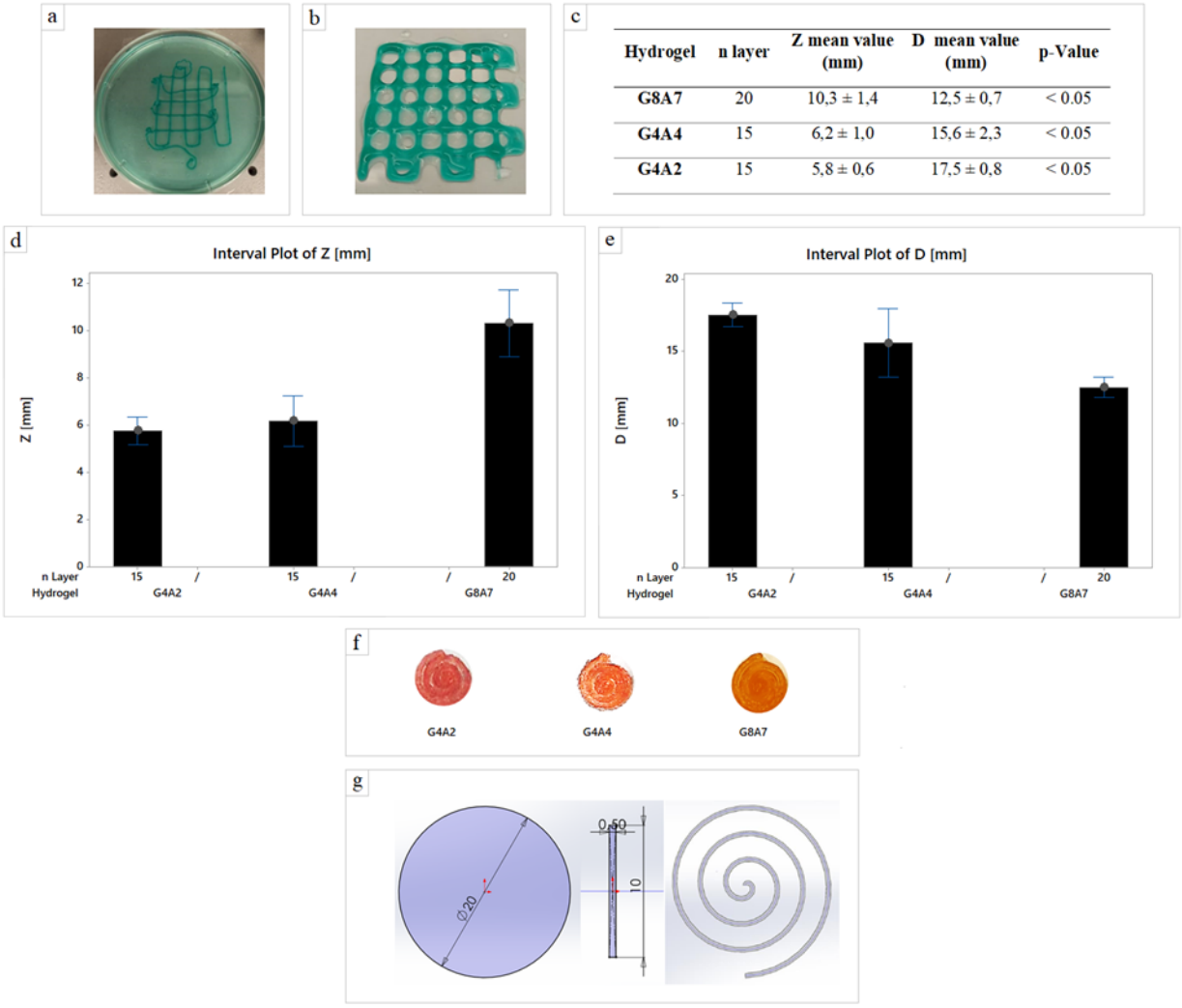

Fig. 2 (a) Grids printed in bath and (b) on a dry surface, pressure 2.3 bar, offset 0.45 mm, and speed 30 mm/s. (c) Summary table: *z* and diameters measurements, and statistical evaluation of the printed structures. (d) *z* measurements for the samples: G8A7 – 20 layers, G4A4 – 15 layers, and G4A2 – 15 layers. (e) Diameter measurements for the samples: G8A7 – 20 layers, G4A4 – 15 layers, and G4A2 – 15 layers. (f) Top view of the best stability results for each hydrogel. G8A7: pressure 1.8 bar, speed 20 mm/s, offset 0.35 mm – 20 layers. G4A4: temperature 10°C, speed 20 mm/s, pressure 1 bar – 15 layers. G4A2: head temperature 10°C, plate temperature 5°C, speed 20 mm/s, pressure 0.8 bar – 15 layers. (g) Spiral CAD specifications: images of the spiral drawing process in Solidworks (Dassault Systèmes, France). Its external limit is set by drawing a 20 mm diameter circumference; the spiral was made starting from a rectangular sketch with a thickness of 0.5 mm and an indicative (since it changes in the printing process, depending on the number of deposited layers) height of 10 mm. The distance between a wall and the next is 2.86 mm.

4.4.3.2 Viscosity analysis

The main results about viscosity as function of the shear rate are collected in Fig. 3.
The viscosity magnitude order is:

- 10^3 Pa*s for G8A7 when the shear rate is lower than 0.57 s^{-1} and 10^2 for bigger shear rate values;
- 10^1 Pa*s for G4A4 for shear rate values between 0.85 and 8.62 s^{-1};
- 10^{-1} Pa*s for G4A2 for shear rate values between 14.24 and 118.69 s^{-1}.

Indeed, for common shear rate values (in the range between 0.85 and 1.73 s^{-1}), a difference of one order of magnitude in viscosity is noticed for G8A7 and G4A4.
The viscosity values recorded for G4A4 are comparable to the ones found in literature for similar hydrogels [14,27–29].

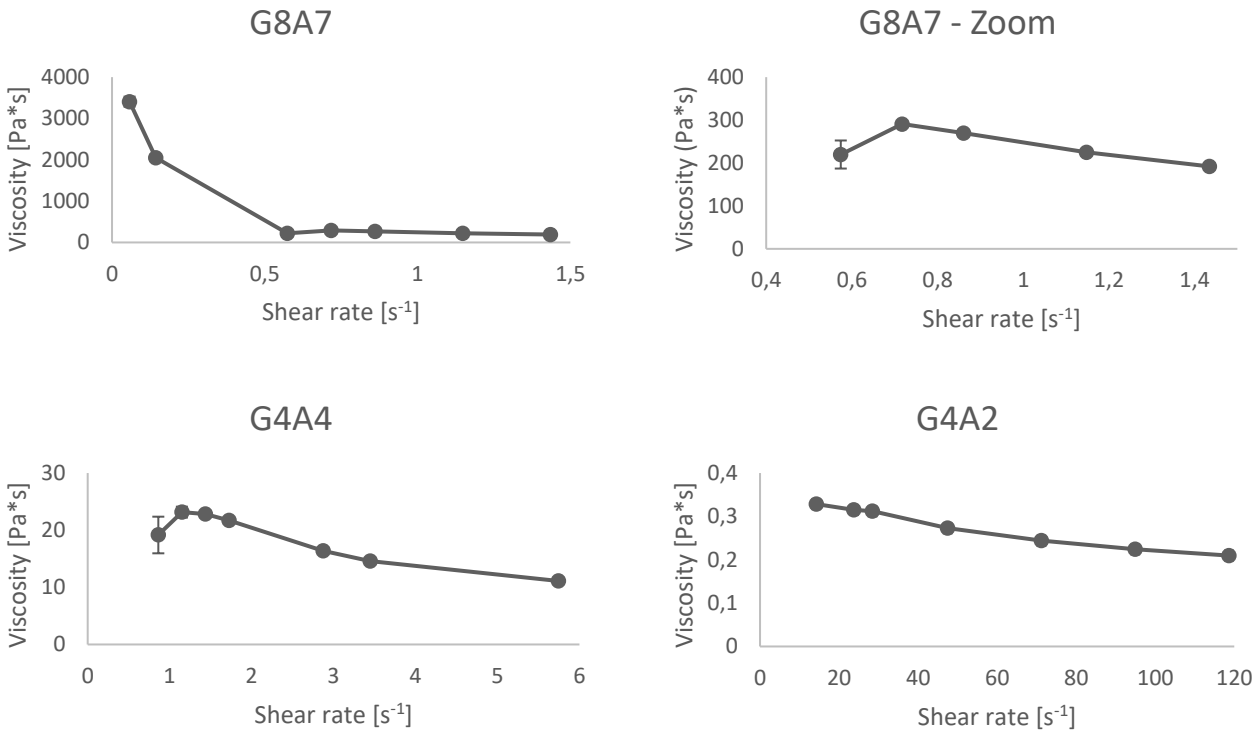

Fig. 3 Viscosity as shear rate's function. Resulting trends for G8A7, G4A4, G4A2.

The viscosity order of magnitude reported in [28] for the 4% (w/v) alginate and 4%(w/v) gelatin (type B) hydrogel is the same recorded by the authors for G4A4. Although these two hydrogels (G4A4 and 4% alginate and 4% gelatin in [28]) share the same order of magnitude, some differences are observed in the values, which can be attributed to the use of different material types (gelatin type A vs type B [28]).
Viscosity values around zero were registered in [27] for shear rate values bigger than 20 s^{-1} for the hydrogel with the following composition: 3% (w/v) gelatin (type B) and 4% (w/v) sodium alginate (50000 Da), mixed within a 0.45% saline solution. So, the 10^{-1} order of magnitude obtained in this work for G4A2 can be considered fair.
Finally, the maximum viscosity obtained in [14] for a 15% (w/v) gelatin and 8% (w/v) alginate (80000-120000 g/mol vs 120000-190000 g/mol used by the authors in this work) is near 10^2 Pa*s.

Hence, according to [14] and observing that, in accordance with [22] and [35], the alginate can be considered more significant than gelatin for the viscosity values, [35] the results here reported for G8A7 (orders of 10^2 and 10^3 Pa*s depending on the shear rate) are consistent.

4.4.3.3 Biocompatibility

G8A7, G4A4, and G4A2 cell-loaded hydrogels have been tested for their biocompatibility both as non-printed hydrogels and after 3D cell printing.

Cells were clearly visible in the G8A7 hydrogel, both printed and non-printed, under microscope inspection; however, they appeared round-shaped also many days after hydrogel incorporation, meaning that cells were not able to spread and to assume their usual morphology, probably because they could not move inside the medium due to its excessive stiffness and difficulty in matrix degradation and rearrangement (Fig. 4a).

Printed and non-printed cell-loaded G8A7 hydrogels were subjected to live/dead staining. Both presented a vast majority of green spots at all the analyzed timepoints, even the later ones. The red spots were very rare or even undetectable, meaning that almost all the cells were alive (Fig. 4b).

On the contrary, ATP test revealed that metabolic activity was very poor: indeed, ATP content was always under 15% of 2D culture control in non-printed hydrogels. The trend was of strong reduction at 3h, probably as a consequence of adaptation to the new culture environment, followed by a slight increase at 24h and 72h; again, the signal was highly reduced at day 7. Nonetheless, the observed differences among timepoints are not statistically significant, due to high variability among replicates. The situation was even worse in the printed hydrogels: at 3h after incorporation (immediately after printing was completed), the metabolic activity was around 0.6% of 2D culture control, and it dropped down to overlap the empty hydrogel at 24h. To this reason, it was not worth going on with later timepoints (Fig. 4c).

The poor metabolic activity may be a consequence of the fact that the formulation resulted highly viscous (see *Viscosity analyses* paragraph) and difficult to handle, since it stayed fluid just within a small temperature window. In addition, the reproducibility of the results was negatively influenced by the difficulty to pipet precise volumes; moreover, the specimens were hardly and not completely disaggregated for ATP test.

The other two investigated hydrogels were characterized by lower gelatin and alginate concentrations.

Similarly, to G8A7 hydrogel, the G4A4 hydrogel did not allow cell spreading. Indeed, cells appeared round-shaped at microscopic inspection also with this formulation (Fig. 5a).

Live/dead staining revealed again that almost all the cells were green (*i.e.*, alive) in both printed and non-printed hydrogels (Fig. 5b). An interesting observation is that the green spots appeared bigger in the non-printed hydrogel, suggesting that cells presented a wider cytoplasm and thus were healthier.

Nonetheless, ATP test revealed poor metabolic activity in the non-printed hydrogel and even worse in the printed one. However, the non-printed hydrogel situation was slightly better in comparison to the G8A7 hydrogel: indeed, the ATP content at t0 was around 16% of MS5 cells in 2D culture conditions. The trend was similar to the previously tested hydrogel: at 3h, ATP signal dropped down and starting from 24h increased again, reaching 17%. The viability remained quite stable for the subsequent timepoints, reaching a peak at day 7, around 25% of 2D culture. The

differences between t0 and 3h and between 3h and 24h are statistically significant, while no significance was recorded between 24h and 72h and between 72h and 7 days.
In the printed hydrogel, 3h after incorporation (immediately after printing was completed), the metabolic activity was comparable to the non-printed counterpart. However, it dramatically decreased at 24h, since the signal was comparable to the empty hydrogel. Nonetheless, it started increasing again, but it settled on 1.4-1.9% at 72h-7 days, meaning that cells failed the adaptation process (Fig. 5c).
The better results in the non-printed hydrogel may be accounted to the fact that the G4A4 hydrogel was much less viscous (as demonstrated above) and easier to handle, and it could maintain its fluidity within a broader temperature window. Nonetheless, the shear stress related to the printing process was enough to prevent cells to survive and proliferate.
Even if the G4A2 hydrogel resulted the less viscous, similarly to the previously tested formulations, did not allow cell spreading. Indeed, also with this formulation cells appeared round-shaped at microscopic inspection (Fig. 6a).
Live/dead staining revealed again that almost all the cells were alive. Moreover, the green spots appeared bigger, with a wider cytoplasm, especially in the non-printed specimens and at later timepoints (Fig. 6b).
The ATP test revealed that the present formulation was the best among the tested ones; however, the metabolic activity barely reached 50% of MS5 in traditional culture conditions in plastic vessels. Indeed, at t0 the non-printed hydrogel showed an ATP content around 25% of 2D culture. It was soon halved at 3h, to significantly increase again at 24h, reaching 37%. Between 24h and 7 days, ATP content was maintained stable, around 40-50% of 2D culture. Regarding the printed hydrogel, the ATP content was about 10% of 2D culture immediately after printing, displaying no significant difference with the non-printed one, but it started increasing at 24h (35%). It increased again at 72h, yet not significantly, while it started slightly decreasing at day 7. It is interesting to notice that at 24h and at 72h no significant difference between printed and non-printed samples was observed (Fig. 6c).
Since the percentage of alginate was brought to 2%, while the percentage of gelatin was maintained constant at 4%, the better results in terms of cell survival and proliferation also in the printed scaffolds may be related to the reduced shear stress on cells while printing, due to the reduced viscosity of the medium (10^{-1} Pa*s vs 10^{1} Pa*s and 10^{2}-10^{3} Pa*s for G4A4 and G8A7, respectively, as reported in the paragraph *Viscosity analyses*). Indeed, it has been previously reported that alginate determines the major effect on viscosity [22,35]; moreover, alginate is the main responsible for cell toxicity in this kind of inks, since it is the substrate of the crosslinking agent, *i.e.*, $CaCl_2$.
The reproducibility of results was also increased: indeed, the G4A2 could be easily pipetted and then disaggregated to perform ATP test. The pipetted volumes were much more accurate than when dealing with hydrogels G8A7 and G4A4.
In Table 3, a direct comparison between cell viability at day 7 and the hydrogel registered viscosity order of magnitude is presented.

Table 3 Direct comparison between hydrogels' cell viability at 7 days and viscosity order of magnitude. Cell viability is reported as % of metabolic activity, compared to the 2D culture. Viscosity is reported in Pa*s.

	Cell viability at 7d (%)		Viscosity's order of magnitude (Pa*s)
	PRINTED	**NOT PRINTED**	
G8A7	N.A.	4.91	10^2-10^3
G4A4	1.87	24.74	10^1
G4A2	35.76	50.57	10^{-1}

A clear relation between viscosity and cell viability is observed. This relation can be attributed both to a higher shear stress on the cells in the syringe when loaded in a hydrogel with higher viscosity, and to the environment cells have to survive and move in. As shown, low viscosity values allow higher cell viability, probably due to a better exchange of nutrients and higher cell motility.

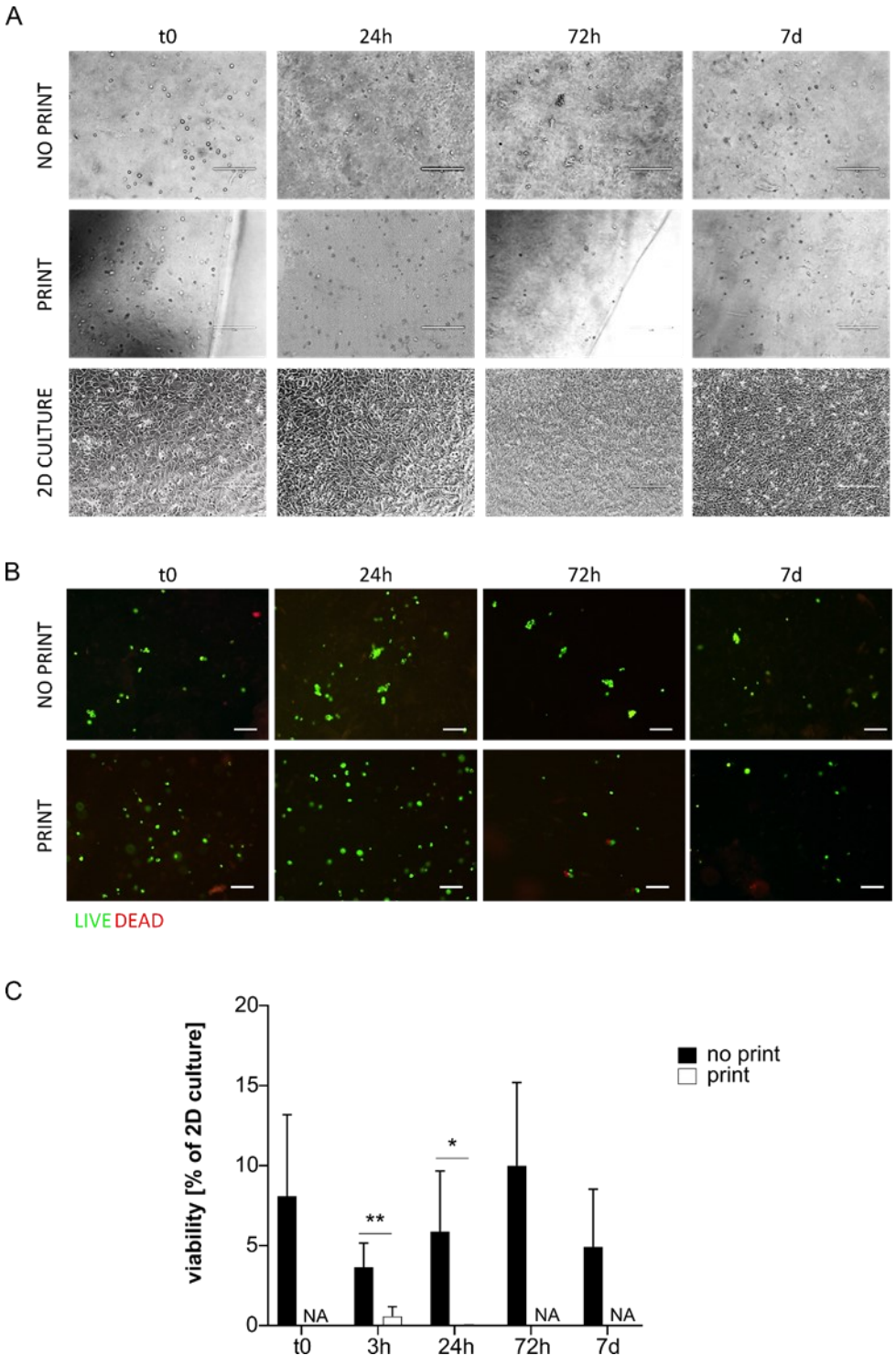

Fig. 4 A) Representative pictures of MS5 cells in non-printed and printed G8A7 and in 2D culture at day 0, 24h, 72h, and 7 days. Scale bar 200 µm. B) Live/Dead assay on cell-loaded G8A7 hydrogel (both non-printed and printed) at t0, 24h, 72h, and 7 days. Representative pictures are shown. Scale bar: 100 µm. C) ATP concentration measurement, expressed as percentage of MS5 cells in 2D culture at t0, in cell-loaded G8A7 hydrogel (both non-printed and printed) at t0, 3h, 24h, 72h, and 7 days. Results are expressed as mean ± standard deviation (N=3 print; N=4 no print); * $p<0.05$, ** $p<0.01$ print vs no print, Student's t-test. NA= not available.

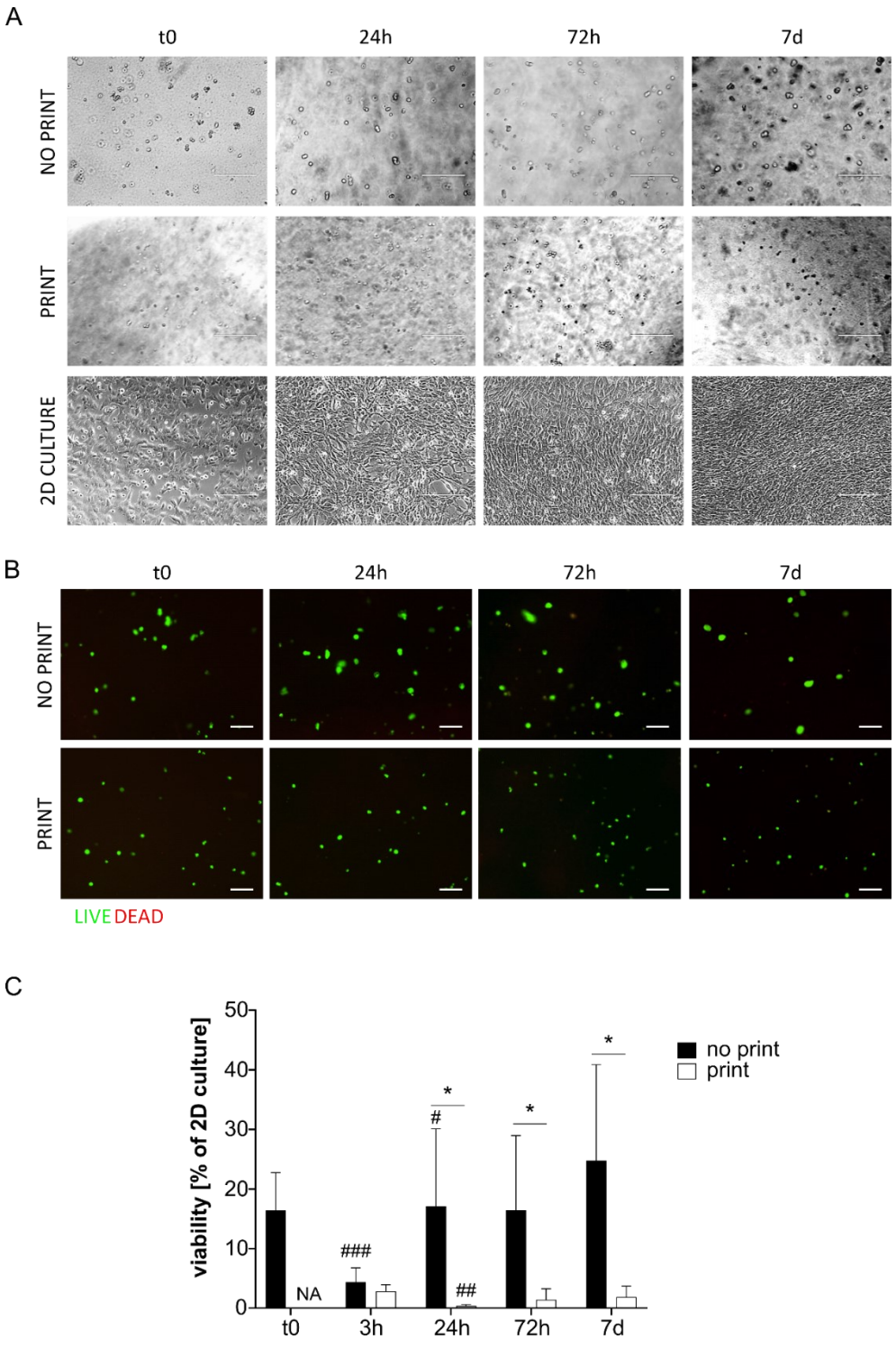

Fig. 5 A) Representative pictures of MS5 cells in non-printed and printed G4A4 gelatin and in 2D culture at day 0, 24h, 72h, and 7 days. Scale bar 200 µm. B) Live/Dead assay on cell-loaded G4A4 hydrogel (both non-printed and printed) at t0, 24h, 72h, and 7 days. Representative pictures are shown. Scale bar: 100 µm. C) ATP concentration measurement, expressed as percentage of MS5 cells in 2D culture a t0, in cell-loaded hydrogel G4A4 (both non-printed and printed) at t0, 3h, 24h, 72h, and 7 days. Results are expressed as mean ± standard deviation (N=7 no print, N=4 print); * $p<0.05$ print vs no print; # $p<0.05$, ## $p<0.01$, ### $p<0.001$ vs previous timepoint, Student's t-test. NA= not available.

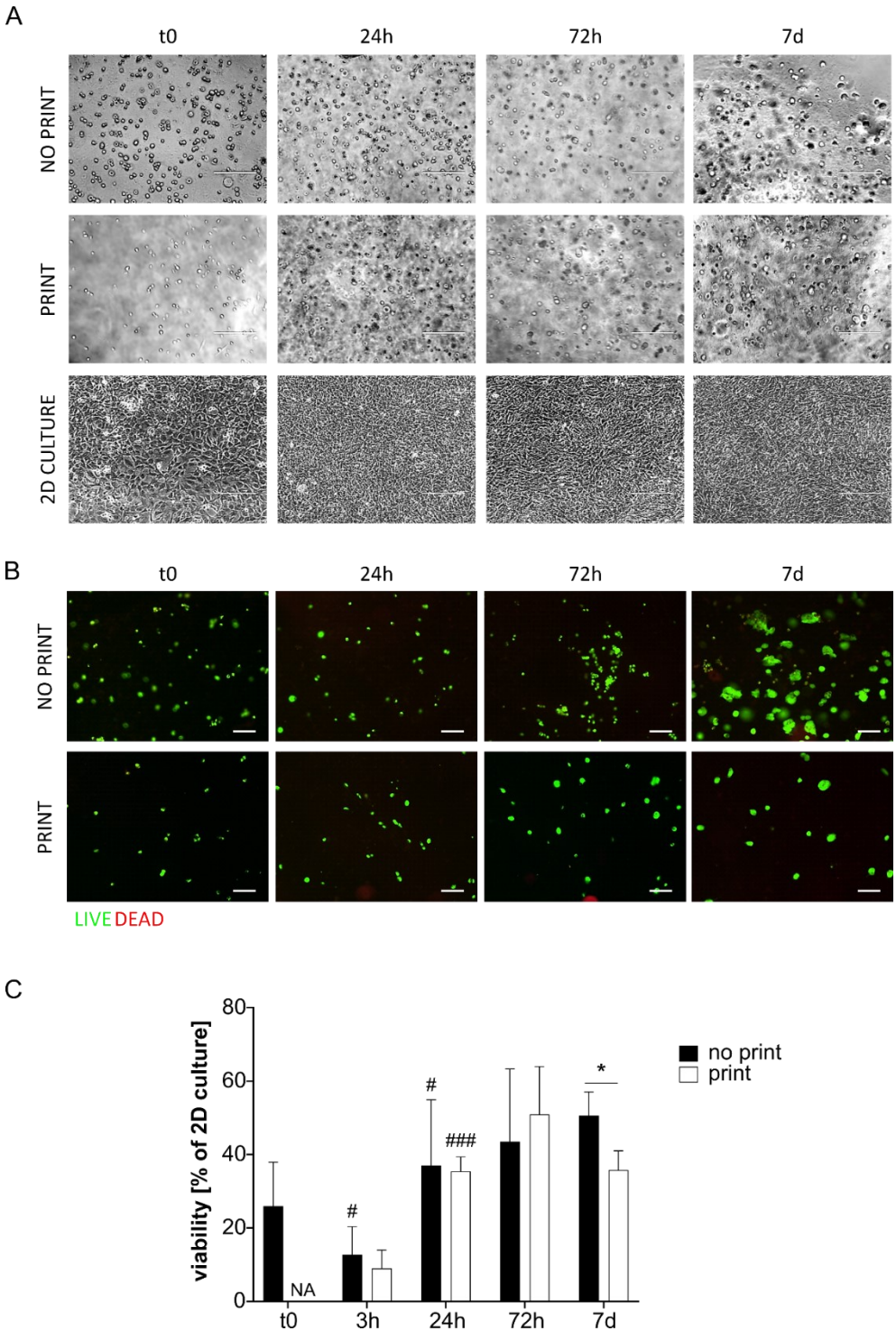

Fig. 6 A) Representative pictures of MS5 cells in non-printed and printed G4A2 and in 2D culture at day 0, 24h, 72h, and 7 days. Scale bar 200 µm. B) Live/Dead assay on cell-loaded G4A2 hydrogel (both non-printed and printed) at t0, 24h, 72h, and 7 days. Representative pictures are shown. Scale bar: 100 µm. C) ATP concentration measurement, expressed as percentage of MS5 cells in 2D culture a t0, in cell-loaded G4A2 hydrogel (both non-printed and printed) at t0, 3h, 24h, 72h, and 7 days. Results are expressed as mean ± standard deviation (N=4 no-print, n=3 print); * $p<0.05$ print vs no print; # $p<0.05$, ### $p<0.001$ vs previous timepoint, Student's t-test. NA= not available.

4.4.4 Conclusions

The aim of this work was to produce a hydrogel suitable to contain cells and to allow their survival, proliferation, and function. However, the production of hydrogels that could guarantee structural stability and cell survival at the same time is complex; indeed, the production processes of such materials are hardly repeatable and cell viability depends on a huge number of factors (crosslinking, shear stress during the extrusion through the nozzle, hydrogel viscosity, printing parameters: pressure, speed, head temperature, bed temperature, presence of the so-called binding sites, use of natural polymers). To reach this goal, it was necessary to consider printability and to test cell viability for the produced hydrogels.

The experiments showed results in accordance with literature:

- The crosslinking in bath (3% $CaCl_2$ in milliQ water) was not suitable to print 3D structures, due to poor adhesion to the substrate, which could be caused by a high crosslinking rate.
- High viscosity values guaranteed more defined structures. This result is due to the higher amounts of alginate and gelatin, which contribute to the structure stability, while increasing the shear stress on cells during the printing process.

The results of this work can also be considered beyond the state of the art:

- The G8A7 hydrogel could be printed in a stable 3D structure; cells seemed alive using the live/dead kit, but the ATP analysis showed poor metabolic activity.
- Differences in cell viability are evident moving from an hydrogel viscosity of 10^{-1} to a viscosity of 10^{2} Pa*s.
- Low viscosity values allow higher cell viability; as a result, the G4A2 hydrogel resulted promising in terms of metabolic activity.
- Live/Dead staining and ATP analysis do not provide the same results in terms of cell viability: the two assays provide complementary pieces of information regarding cell survival, metabolic activity, and proliferation.

From these points it can be concluded that the results on hydrogel biocompatibility reported in the majority of literature on BP should be precisely evaluated, since the mostly used assay to assess cell viability is the Live/Dead staining for imaging, often limited to early timepoints (t0, 24h). In addition, cells are usually 3D-printed at a density of millions of cells/mL [36,37]. Surely, such a strategy could guarantee a better survival of the cell population, however, the actual cells percentage of the tissue that is meant to be reproduced should be considered to validate each bioprinted model. Further research will investigate other hydrogel compositions, in order to obtain a hydrogel that allows and supports cell viability, also in terms of metabolic activity. Moreover, other crosslinking baths will be developed to improve and support the 3D structure stability according to the Freeform Reversible Embedding of Suspended Hydrogels (FRESH) method [38,39], that exploits processed gelatin as a support both during the printing and the crosslinking phases and promotes this last process.

Chapter 5

3D printing Case Studies for tissue engineering: Laser Powder Bed Fusion

Based on the studies mentioned earlier, once the technique of scaffold printing has been optimised, its cell biocompatibility is the key aspect. Research on biocompatibility has been conducted since before the introduction of 3D BP. It is important to note that orthopaedic implants and prostheses are made from materials that do not enclose cells. Instead, they must seamlessly integrate with the surrounding environment and avoid causing infection or rejection.
The surface of the items to be implanted plays a crucial function.
Recently, the manufacturing of implants has shifted away from traditional methods and adopted AM, specifically 3D printing. The analysis of surfaces produced through 3D printing presents significant challenges because to their inherent variability, which is influenced by the printing conditions. This variability surpasses that observed in conventional production methods.
This chapter will provide a case study that examines cellular interaction. The study focuses on the surface level interaction of metal components printed in 3D:

- R. Rovetta, P.S. Ginestra, R. M. Ferraro, K. Zohar-Hauber, S. C. Giliani and E. Ceretti, "Building Orientation and Post Processing of Ti6Al4V Produced by Laser Powder Bed Fusion Process", J. Manuf. Mater. Process. 2023, Volume 7, Issue 1, 43
  In this work, the candidate was responsible of the literature search, data collection and organization, and writing and editing of the draft.

5.1 Building Orientation and Post Processing of Ti6Al4V Produced by Laser Powder Bed Fusion Process

LPBF, particularly the SLM, is an AM technology used to produce near-net shape engineering components for biomedical applications, especially in orthopaedics. Ti6Al4V is commonly used for product orthopaedic im-plants using SLM because has excellent mechanical qualities, a high level of biocompatibility, and corrosion resistance. However, the main problem associated with this process are the surface properties: it has to be able to promote cells attachment but, at the same time, avoid bacteria colonization. Surface modification is used as a post-processing technique to provide items unique qualities that can improve their functionality and performance in particular working conditions. The goal of this work was to produce and analyse Ti6Al4V samples fabricated by SLM with different building directions in relation to the building plate (0° and 45°) and post-processed by anodization and passivation. The results demonstrated how the production and post processes had an impact on osteoblast attachment, mineralization, and osseointegration over an extended period of time: anodization treatment result cytotoxic, but the biocompatibility of as-built specimens and specimens after passivation treatment was confirmed. In addition, it was discovered that effective post-processing increases the mineralization of these types of 3D-printed surfaces.

5.1.1 Introduction

The demand of orthopaedic implants is estimated to increase rapidly over the decade. In order to support damaged tissues and bones and improve patient comfort, researchers in the field of orthopaedic implant production have developed a variety of solutions [1,2]. Numerous advantages come with these orthopaedic implants solutions, including relatively low cost, less discomfort, and quick recovery. In the future years, the worldwide orthopaedic implants demand will move towards less invasive and more affordable techniques for joint replacement surgery. In order to satisfy this demand, use of new production technologies is crucial [3–6].

AM is one of the most modern and continuously evolving technologies. AM, better known as 3D printing, has been empowering re-searchers to make parts directly from digital designs. AM has made it easier to make new 3D parts in low to medium volumes than before. Because of the ability of AM to produce highly customized products, the use of different AM technologies has grown significantly in the biomedical field, especially orthopaedics [7,8]. An integral part of using this technology is choosing the most suitable materials as well as the most suitable AM techniques [9,10]. The mechanical qualities of titanium and its alloys, particularly those provided by the surface such corrosion resistance and bioactivity, make them ideal materials for orthopaedic implants [11]. Ti6Al4V alloy, in particular, is frequently utilised for bone replacement due to its qualities that improve the adhesion between native tissue and the implanted material [12–17].

Printing titanium alloys has been successfully accomplished using SLM, one of the most widely used AM techniques [18]. In SLM process, metallic powders are uniformly spreaded across the build plate using a roller or wiper and fused together selectively according to the CAD model by a high energy laser beam in a protective atmosphere [19,20]. SLM offers a great chance to create sophisticated bespoke implants with the desired inner structure and surface morphology [21–23]. The final properties of the product depend not only on the source file, typically a CAD scanned

by the patient, but also on the process parameters. This study [24] summarize that in the manufacturing of Ti6Al4V with SLM process, factors such as laser power, scanning speed, and powder bed temperature have a substantial impact on product quality and produce varying degrees of confidence. More precisely, in terms of the macro-scale, the process parameters have limited impact on geometry, compared to how they are crucial for the micro-scale properties, particularly the sur-face quality, crucial for the biomedical applications [25–27].
There is typically insufficient osteointegration between the implant and host bone tissue as a result of the product surface. In fact, one of the most important issue with the in-vivo implant is a weak cellular adhesion against bacterial proliferation [28–30]. According to this interesting perspective, implants with a certain surface topography have a high potential for improving osseointegration [31]. Surface micro/nanostructures can therefore be created by surface modification to improve the interaction between the implant and the cell colonization, such as migration, proliferation, and differentiation [32,33]. Many surface modification approaches may be used to increase Ti6Al4V bioactivity and bone-implant compatibility [34–36]. First and foremost, process parameter optimization with the tunability of the building angle followed by chemical and physical modification with anodization and passivation, i.e. etching, in the post-processing phase [37–39].
The orientation of the built in relation to the printing plate plays a key role in the surface porosity. In particular, 0° orientation produce a greater degree of porosity than higher angle. On the opposite, 45° show better mechanical feature, such as tensile and fatigue properties [24]. In this study [40], the effect of the building angle on osseoingration was examined. The higher contact angles of the SLM surfaces are encouraging cell attachment. In comparison to the same gene expression on samples with a 45° orientation, the short-term osseointegration of SLM specimens created at 0° may be expedited.
Electrochemical anodization process that permits the generation of an oxide layer with tubes structures on the surface. The setup involved a counter electrode of Ti flat foil and Ti 3D implant immersed in ethylene glycol electrolyte, and NH4F. A constant voltage was applied. The main technological advantage of anodizing titanium is functionalization of medical implants for better bonding with tissue and enhance cell growth on the implant [41,42].
The etching process involves in removing the surface layer of SLM parts by an acid attack. This treatment is widely used to obtain a uniform and clean surface which can be hostile to bacteria but accommodating to host cells. Furthermore, it is attractive due to its simplicity, cost-effectiveness, and potential for large-scale manufacture [43–45].
The key goal of this paper is to combine two different surface modification approaches on the 3D printed Ti6Al4V implants. The combination of building angle effect and post-process treatments creates a specific surface topography challenging for biomedical applications.
The building angle chosen for this study were 0° and 45°, according with previous study [40].
Two different post-processing treatments were designed for the modification of the samples taking the original 3D printing features into consideration: anodization and passivation. In vitro cell experiments were performed to study the effects on cell adhesion, proliferation, and MC3T3-E1 differentiation.

5.1.2 Materials and Methods

5.1.2.1 Fabrication of the Ti6Al4V Samples

SLM process allows to set the angle for the laser building strategy in relation to the building plate. Here, the orientations chosen to produce the implant models were 0° and 45°.

Cubical samples (10 × 10 × 10 mm3) were fabricated by SLM using an EOS M290 (EOS, Robert-Stirling-Ring 1, D-82152 Krailling Germany) with Ti6Al4V (Ti64) in-ert-gas atomized powder (ARCAM Ti64Al4V powders and EOS Titanium Ti6Al4V). The relevant properties of the used Ti6Al4V powders are reported in Table 1 according to the required datasheets according to ASTM B214, B215, B212, F2924 and F1472 [46–48].

Table 1 SLM Ti64 powders properties and compositions. Data were gathered in accordance with the relevant international ASTM standards.

Particle size analysis[1]			Powder density[2]	Chemical Composition[3]				
(μm)			(g/cm3)	(wt %)				
d10	d50	d90	2.31	Al	V	O	Fe	Ti
27.79	38.18	54.45		5.92	4.04	0.13	0.20	Bal.

[1] ASTM B214 and B215 [46]. [2] Apparent density, ASTM B212 [47]. [3] ASTM F2924 and F1472 [48]. Bal., balance.

The SLM samples were produced with these manufacturing parameters: laser focus diameter 70 μm, laser power 340 W, hatch spacing 40 μm, slice thickness 30 μm, scanning speed 1250 mm/s. Specifically, a scanning strategy with alternating angle between layers was used, the variation was set at 67°. Controlled atmosphere was used for the manufacturing to minimize oxygen pick-up to <0.1% with argon gas.
The SLM process requires the building of support structures to guarantee the stability of the samples. The parameters used were: laser power 100 W and scanning speed 600 mm/s.
The support structures were removed from the site at the conclusion of the manufacturing process. The standard cleaning methodology used for the samples was sonication in acetone and isopropanol, followed by air drying.

5.1.2.2 Post-Processing of the Ti6Al4V Samples

Anodization

Titanium 3D samples were cleaned using ultra-sonication in ethanol to remove surface debris. An oxide layer was fabricated using an electrochemical anodization setup. The setup involved a counter electrode of Ti flat foil and Ti 3D implant im-mersed in ethylene glycol electrolyte, containing 1% water (υ/v) and 0.3% NH4F (ω/v), maintained at 25 °C, on a magnetic stirrer. A constant voltage of 60 V was applied for 20 min. Post-anodization, the prepared TNT 3D samples were washed with deionized water and dried in cool air.

Etching

The SLM specimens were ultrasonically cleaned in ethanol for 20 minutes to shake off any trapped powders and clean the samples. Afterwards, the specimens were etched in Kroll reagent (3 mL 48 vol. % HF, 6 mL 70 vol. % HNO3 and 100 mL water) at room temperature for 10 min. Then, all specimens were cleaned in distilled water and ethanol, ultrasonically and air dried.

5.1.2.3 Characterization of the Ti6Al4V Samples

Surface Wettability

Attension Theta Lite optical tensiometer (KSV NIMA Biolin Scientific, Hängpils-gatan 7 426 77 Västra Frölunda, Sweden) was used to obtain the contact angle measurements.

The measurement was carried out at room temperature and the SLM samples were placed on the bottom flat surface, subsequently a droplet of deionized water (5–10 μL) was pipetted into the center of the top surface (different building angles were considered). The images of the contact angle were captured following the horizontal plane of the droplet for 30 s after application. To obtain the inner angle between the surface and air/water interface the OneAttension software converts the images to 8-bit grayscale.

Optical Microscopy: Three-Dimensional Surface Reconstruction and Roughness Analysis
Wyko NT1100 3D Optical profilometer (Veeco, One Terminal Drive. Plainview, NY 11803. USA) at 2.5x magnification was used to perform the optical imaging of the SLM samples, at different building angles and with different post-processing treatement. The scanning was execute between the maximum and minimum focusing points of the z height of the samples surfaces. At the central point of the surface was selected a scanning size of 0.92 × 1.2 mm2 with a sampling of 1.65 μm. Vision Veeco Module (Veeco, One Terminal Drive. Plainview, NY 11803. USA) was used to evaluate and analyze the roughness parameter (Sa).

Scanning Electron Microscopy: Surface Topography Analysis
Inspect™ environmental SEM (FEI, NSS-II Bldg 4F. 13-34 Kohnan 2-chome. Tokyo, Minato-ku. 108-0075 JPN), operating at 20 kV, was used to observe Ti64Al4V SLM as-built and post-processed specimens. To obtain the topographical imaging, the samples were fixed with double-adhesive carbon tabs at the aluminum stubs. To evaluate the cross-section and examine the surface profile the samples were embedded in cold resin epoxy and then polished.

Statistical analysis
The statistical tests were carried out to verify if the building angle and the post-processing treatment had any effect on the contact angle and roughness of the samples. Single-factor analysis of variance (ANOVA) tests were performed to confirm any statistical significance within samples and to determine repeatability.
Statistical analysis was conducted at $\alpha = 0.05$ using Minitab 18® (MINITAB, Brandon Court Unit E1-E2, Progress Way, Coventry CV3 2TE UK).

5.1.2.4 Biocompatibility test, and Mineralization assay
Cell Line
MC3T3-E1 Subclone 4 cells (BS CL 181, IZSLER, A. Bianchi Street, 7/9, Brescia, 25124, Italy) from passage 39 were cultured at 37 °C and 5% CO2, as previously de-scribed [40]. Briefly, the preferential medium to sustain the MC3T3-E1 proliferation is composed by Alpha Minimum Essential Media (α-MEM) with sodium bicarbonate, ribonucleosides, and deoxyribonucleosides (BioConcept, Paradiesrain Street 14, Allschwil, 4123, Switzerland) supplemented with 10% FCS (Euroclone, Figino Street, 20/22, Pero, Milan, 20016 Italy) and 100 units/mL pen/strep (Euroclone, Figino Street, 20/22, Pero, Milan, 20016 Italy). To promote the MC3T3-E1 mineralization the basal medium was enriched by adding 50 μg mL−1 ascorbic acid (Sigma-Aldrich), 10 mM β-glycerophosphate (Sigma-Aldrich,3050 Spruce Street, St. Louis, Missouri, 63103, USA), and 100 nM dexamethasone. The mineralization medium was changed every 3 days.
For all assays 5 x 104 cells/cm2 were seeded in a proper volume of medium on the titanium substrates andon plastic dish as positive control.

Prior to each in vitro experiment, titanium samples were washed in PBS for 1 hour on an orbital shaker, further sterilized in an autoclave at 121°C for 20 minutes, and put into 12-well plates with a sterile tweezer.

Biocompatibility tests: direct and indirect ATP cell viability assay

CellTiter -Glo 3D Cell Viability (rATP) assay kit (Promega, 2800 Woods Hollow Road, Madison, Wisconsis, 53711, USA) is an enzymatic assay that utilizes the adenosintriphosphat (ATP) produced by the cells to convert luciferin into oxyluciferin, which generates a light signal that is proportional to the number of metabolically active cells in culture. A reduced luminescence can be due by either cell death or metabolic quiescence for over-confluence or medium consumption. For the direct rATP assay, MC3T3-E1 were enzymatically detached and centrifuged at 1300 rpm for 4 minutes in order to obtain a single cells suspension in fresh medium. The supernatant was removed and MC3T3-E1 were seeded at a cellular density of 5 x 104 cells/cm2 on the samples. A concentrated cell suspension was deposited onto each support and incubated for 20 minutes before filling each well with a proper volume of medium. The same concentration of MC3T3-E1 were seeded on plastic dish as positive control. Cells were maintained at 37 °C in a saturated humidity atmosphere containing 95% air and 5% CO2. After 24, 48, and 96 hours, the substrates were shifted into new culture plates in order to not consider into the analysis the cells fallen down from the titanium substrates and grown on the plastic dish. Then, residual adherent cells were lysed on the samples using the CellTiter-Glo 3D Reagent and after 25 minutes of incubation in the dark the total volume was transferred into an opaque-walled 96-well plate and the luminescence was recorded using a Tecan Infinite® M200 microplate reader (Tecan, Männedorf, Switzerland). Parallelly, an ATP standard curve (range of 10 □M to 10nM) was generated using rATP disodium salt (Promega cat. P1132) to compare the samples luminescence to the standard ones in order to determine the correct ATP concentration. Hence, the ATP concentration recorded from each sample was calculated and plotted. At each time point, unpaired t-test was conducted on results derived from three different experiments (n=3) to determine if the different surface treatments significantly modified the metabolic activity in comparison to the control samples cultured on plastic dish.

For the indirect rATP assay titanium supports were placed in a 12-well plate and let to release any potential cytotoxic components into 2 mL of complete α-MEM for 5 days in a humidified incubator at 37°C and in 5% CO2 atmosphere. As reference, the same volume of medium was poured in an empty dish and placed in the incubator at the same conditions. The day before the test, MC3T3-E1 were seeded in flat bottom 24-well plates (5 × 104 cells/well). The day after, cell supernatant was removed and re-placed by either titanium sample conditioned medium or control medium. After 24, 48, and 96 h the cells seeded in the 24- well plates were lysed using the CellTiter-Glo 3D Reagent and the rATP assay was performed as described before for the direct test.

Mineralization evaluation by osteogenic gene expression analysis

The mineralization process was analyzed collecting the total RNA from the cells adhered to the scaffolds after 30 days of culture. The RNA extraction, RNA ret-ro-transcription into complementary DNA (c-DNA), and the gene expression analysis by quantitative Real time PCR (qPCR) were performed as previously described [40]. The relative quantification of target genes (*Bsp, Ocn, Opn*, and *Mepe*) was calculated by the $2^{-\Delta\Delta Ct}$ method, using *Gapdh* as housekeeping gene for normalization of the data and the constitutive gene expression of the same markers from MC3T3-E1 cells cultured in basal medium without mineralization as calibrator.

5.1.3 Results

5.1.3.1 Surface Topography of the Titanium Samples

The scanning electron micrographs analysis shows the surface condition of samples produced with SLM at various building angles and then processed to modify their surface characteristics (Fig. 1).

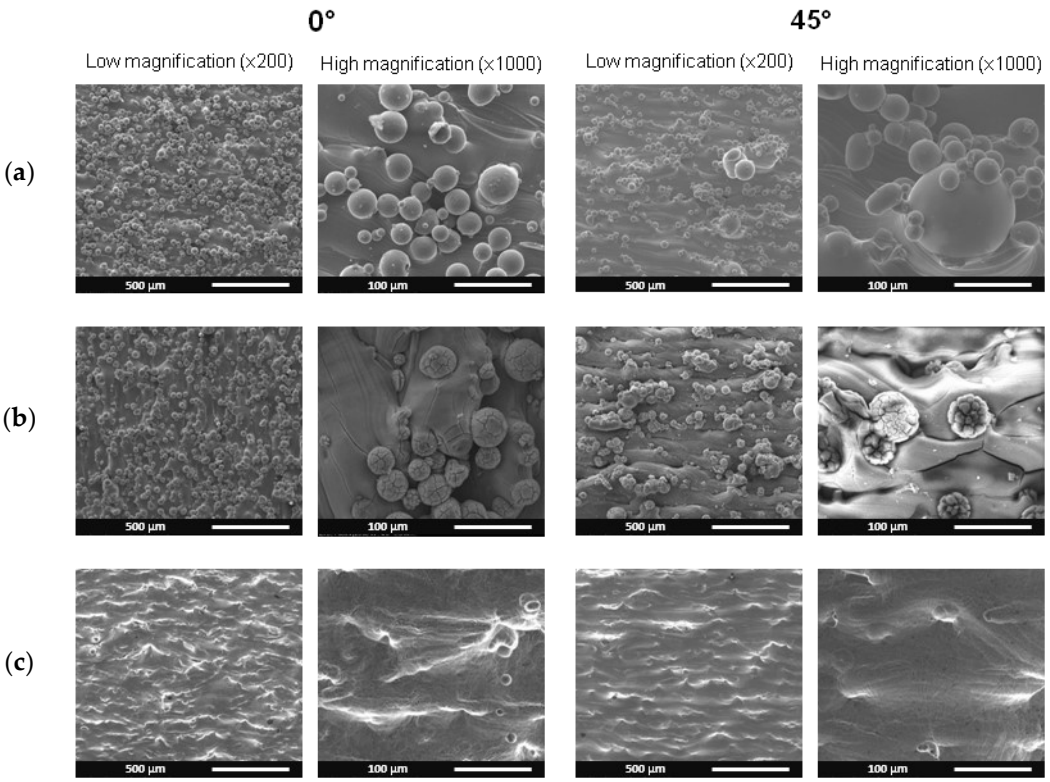

Fig. 1 Micrographs illustrating the surface topography of the Ti6Al4V samples manufactured by SLM at 0° and 45°: as-built (a), with post-processing treatments anodization (b) and etching (c).

A distinct distribution of spherical partially melted powder particles is observed in the as-built samples. Particularly for samples with a 0° building angle, particles are uniformly distributed over the surface; however, when the building angle is increased to 45°, the particles have a diameter comparable to the 0° sample, ranging from 30-50µm, but have a less homogeneous distribution, with the formation of clusters on the order of 130µm in diameter (Fig. 1).

The anodization treatment causes no considerable morphological alterations to the sample surface at 0° building angle, in fact the same uniformity of particles distribution is observed. The 45° degree samples, on the other hand, exhibit considerable morphological alterations. Cracks appear on the spherical surface of the particles and the number and dimension of the clusters increase.

However, the significant surface alteration is due to the etching treatment. The acid attack has totally smoothed the surface of the specimens, regardless of the building angle. Particles are almost absent, only roughness ridges and a few craters are visible, probably caused by the detachment of clusters or particles with bigger diameters.

Table 2 CA measurements and statistical evaluation of the samples as-built, anodized and etched.

Angle SLM	Mean Value [°]			P-Value
	As-Built	Anodized	Etched	
0°	129.64 ± 5.32	75.48 ± 5.31	70.64 ± 5.70	0.003
45°	120.91 ± 2.32	38.8 ± 24.1	108.48 ± 0.993	0.018

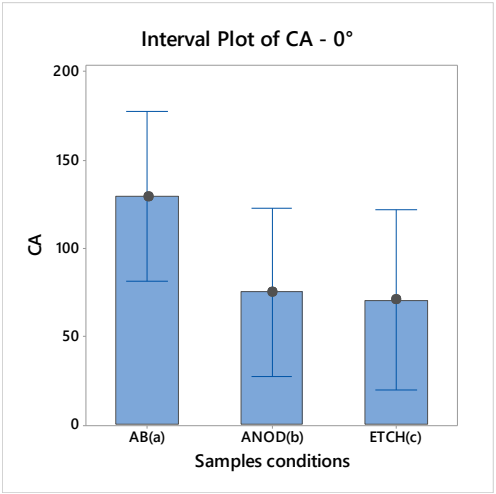

(a)

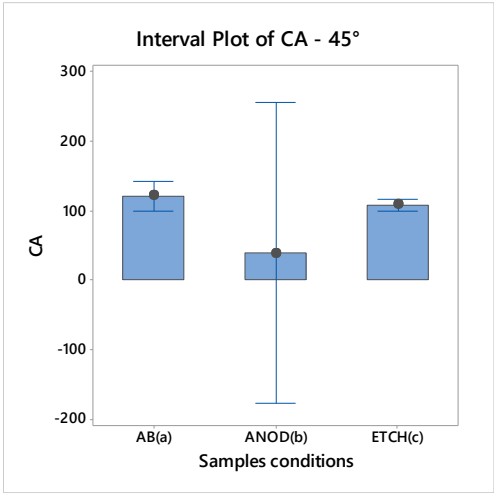

(b)

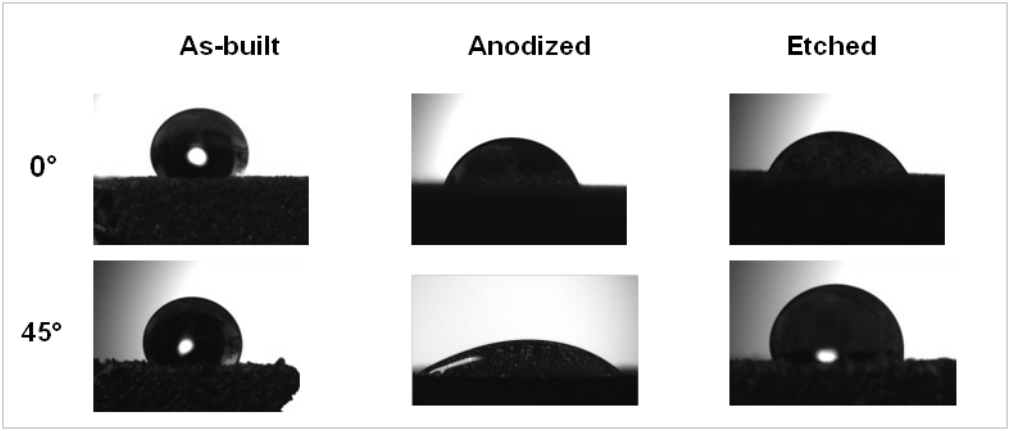

(c)

Fig. 2 CA measurements for the samples: (**a**) 0° building angle individual samples (**b**) 45° building angle individual samples; (**c**) images of the water droplets on the top surfaces at different building angles and treatments.

Table 3 Sa measurements and statistical evaluation of the samples as-built, anodized and etched.

Angle SLM	Mean Value [°]			P-Value
	As-Built	Anodized	Etched	
0°	17.84 ± 4.76	6.29 ± 0.399	2.307 ± 0.326	0.001
45°	20.40 ± 5.02	6.35 ± 2.71	2.200 ± 0.416	0.001

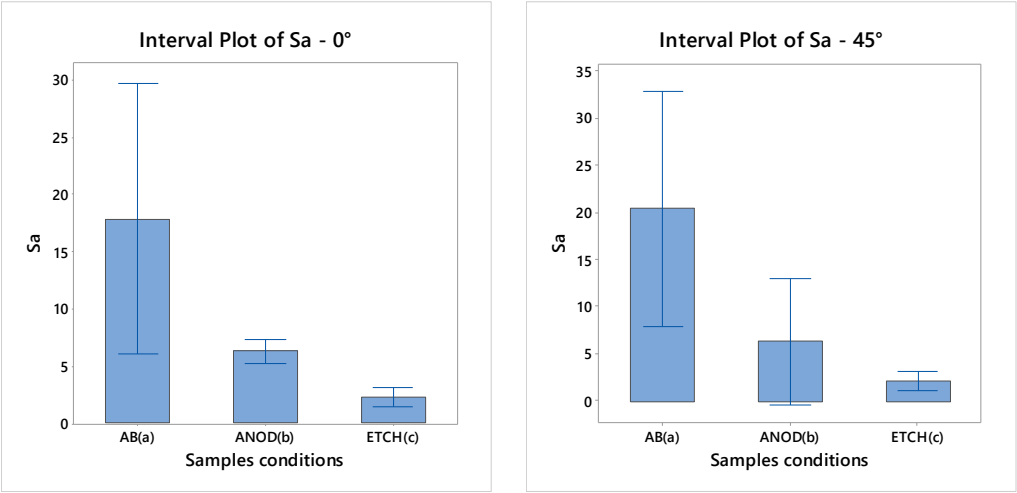

(**a**) (**b**)

Fig. 3 Sa measurements for the samples: (**a**) 0° building angle individual samples (**b**) 0° building angle individual samples.

The surface roughness Sa is measured to evaluate the sample surface finishing in relation to the manufacturing operations. For each measurement, three were used and results were elaborated with one-way ANOVA test. The results demonstrate the influence of the building strategy, in particular the building angle, and post-processing treatments. The Sa roughness increases with increasing angle, despite being comparable in magnitude. This difference is consistent due to the presence of clusters and the irregular dispersion of particles as observed in the scanning electron micrograph.

The roughness is greatly reduced by the anodizing procedure, which also equalizes the differences between 0° and 45° samples, making the values comparable to the micrometer. The etching procedure significantly reduces surface roughness. The Sa values demonstrate the surface's full smoothness, as shown in the micrographs. Moreover, there are no appreciable differences between the samples with various building angle.

The samples production strategy has low impact on roughness if samples are subjected to post-processing treatments like anodization or etching. Statistical significance and value trends are shown in Table 3 and in Fig. 3.

The SEM metallographic cross-section samples show the surface profile of the top surfaces of the different printed parts (Fig. 4): as-built, anodized and etched.

The profiles along the cross-sections of the samples reveal a varied trend at different building angles and post-processing treatments. The as-built samples exhibit surface features that were created as a result of the powder on the top layer partially melting. In particular, as the angle increases also the superficial structure increase in number and dimensions. The surface aspect is highly dependent on post-processing treatment. The anodized samples show surfaces with protruding structures, that be-came more sever when the building angle increases, with an irregular and roughened profile. The partial melting particles are still present. Instead, the etched

samples show a smoothen surfaces without significant differences due to the building angle and without any residual particles typical of a SLM manufacturing process.

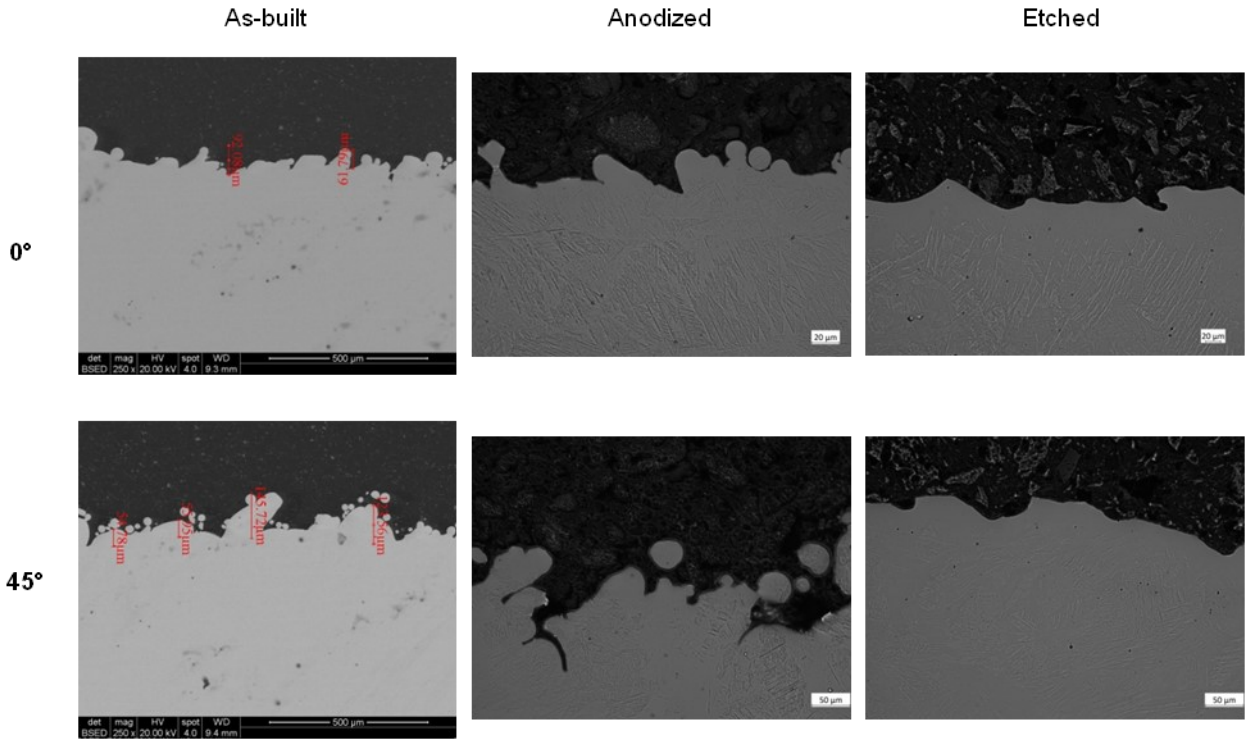

Fig. 4 Micrographs illustrating the surface profile of the cross-sections of the samples built at different building angles and with different treatments.

5.1.3.2 Biocompatibility of Titanium Scaffolds

Direct rATP assay

The application of biocompatible materials is essential to promote and sustain the metabolic activities of the seeded cells. In particular, the substrate chosen should guarantee the cellular surviving and the metabolism. The environment, the so called "biological niche" is full of stimuli for the cellular growing, differentiation and maturation. Cells in an unfavorable environment to replicate, arrest their cell cycle into a quiescent phase, while remaining viable. rATP assay detects the ATP produced by the cells and allow to analyses the biocompatibility of a material studying the metabolic activity of cells cultured on it. MC3T3-E1 cells were seeded onto SLM As-Built, Anodized and Etched (0° and 45°) scaffolds and analyzed after 24, 48, and 96 hours in culture. Fig. 5 shows ATP (μM) concentrations at different time points of MC3T3-E1 cultured onto plastic, as internal control, and on each scaffold typology.

A positive growth trend of proliferation is observed for MC3T3-E1 on the plastic well plate, unlike cells grown on the titanium substrates that show a variable behavior. Cells on the SLM As-Built scaffolds confirmed the biocompatibility already shown previously [40]. The cellular viability of MC3T3-E1 on SLM Etched is reduced for both angles of fabrication in comparison to the plastic dish, with significant differences. By contrast, Anodized samples show a strong statistical significant decrease in metabolic activity, evident already after 24 hours from cells seeding (p value < 0.0001).

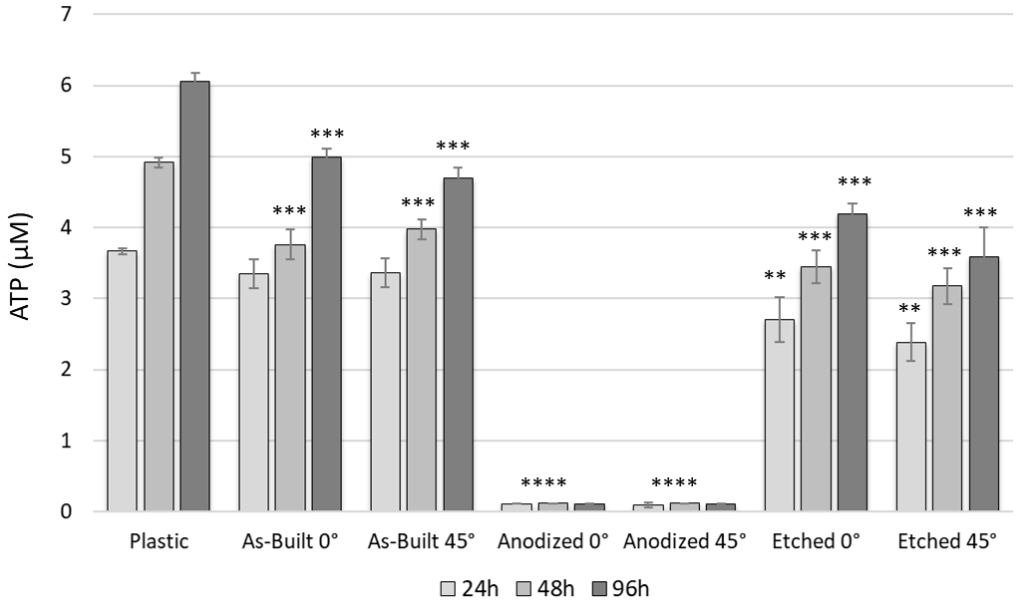

Fig. 5 ATP (µm) concentrations of MC3T3-E1 cells cultured on titanium SLM As-Built, Anodized and Etched 0° and 45° scaffolds and on a plastic dish after 24h, 48h, and 96h. Unpaired t-test was applied to discriminate differences between MC3T3-E1 cultured on a plastic dish and on each scaffold considering a value of $p < 0.05$ statistically significant (*$p < 0.05$, ** $p < 0.01$, ***$p < 0.001$, ****$p < 0.0001$).

Indirect rATP assay

In order to understand if the absence of cellular metabolic activity observed for the Anodized samples is related to a not biocompatibility of the material or to a cellu-lar adhesion problem that has caused the loss of all the cells on the substrates, an indi-rect rATP assay was performed. Specifically, the analysis included the ATP concentra-tion derived from MC3T3-E1 cultured in conditioned medium (medium collected from dishes containing each typology of titanium substrate for 5 days in incubator), and in control medium (medium put in an empty well and kept at the same conditions) as experimental positive control. With this kind of test, it is possible to bypass any differ-ences in terms of cell adhesion potential of each substrate and consider only the bio-compatibility of the material. Fig. 6 shows the result of the indirect rATP assay at three times point (24, 48, 96h). Medium collected from Anodized substrates results in drastic high levels of cytotoxicity already at 24 h, showing no cellular survival (p value < 0.0001). By contrast, medium collected from others titanium scaffolds shows a bio-compatible potential: the cell viability trend is comparable to the control medium with no statistical significant differences between angles of fabrication or treatment.

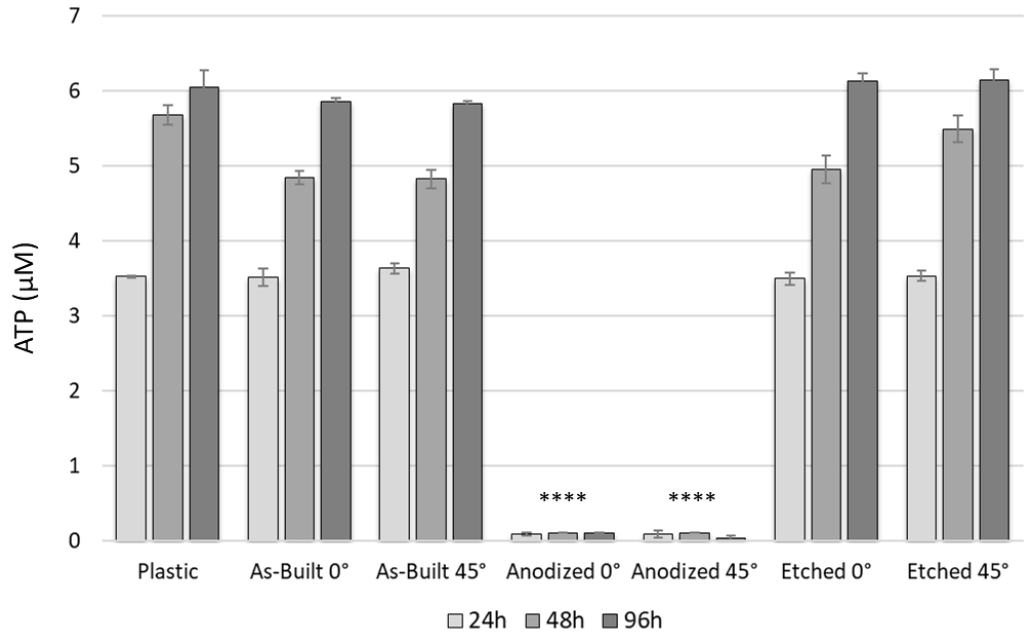

Fig. 6 ATP (µm) concentrations of MC3T3-E1 cells cultured in conditioned and in control medium at different time points (24h, 48h, and 96 h). Unpaired *t*-test was applied to discriminate differences between MC3T3-E1 cultured on a plastic dish and on each scaffold considering a value of $p < 0.05$ statistically significant (*$p < 0.05$, ** $p < 0.01$, ***$p < 0.001$, ****$p < 0.0001$).

Osteogenic Differentiation and Mineralization on Titanium Scaffolds

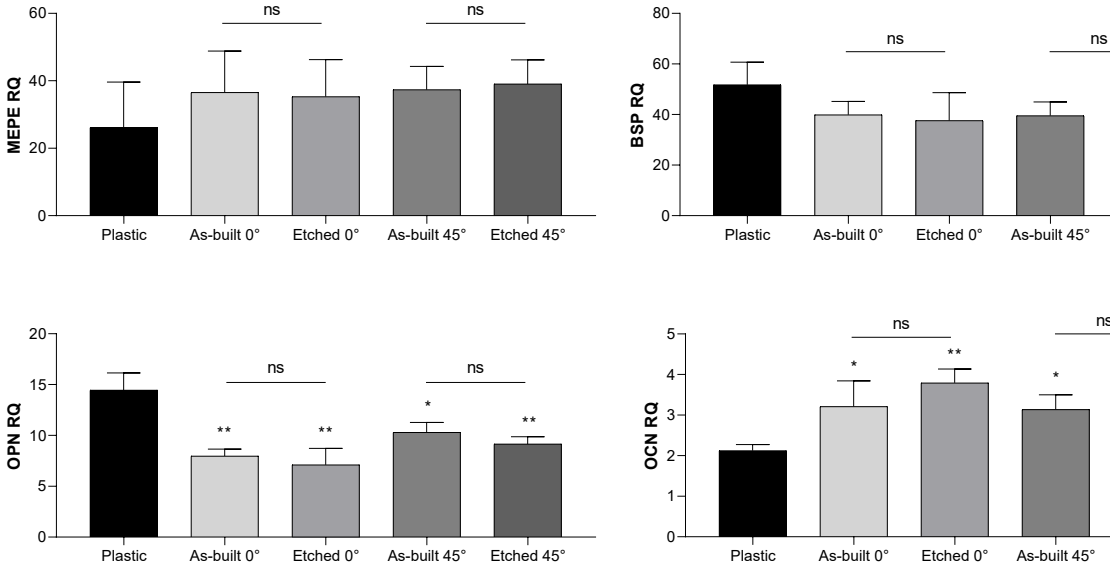

Fig. 7 Gene expressions evaluation of MC3T3-E1 cells cultured in mineralization medium after 30 days on titanium SLM As-Built, Etched (0° and 45°) scaffolds and on a plastic well plate. Unpaired *t*-test was applied to discriminate differences between plastic dish and each scaffold considering a value of $p < 0.05$ statistically significant (*$p < 0.05$, ** $p < 0.01$, ***$p < 0.001$, ****$p < 0.0001$). Unpaired t-test was used also to compare As-built substrates and relative Etched scaffolds ("ns" indicates not significant, $p > 0.05$).

The biological characterization of the titanium supports described in this work was deepen only for the Etching treatment, as the Anodizing ones were found to be not biocompatible. In particular,

the mineralization potential of Etched titanium scaffolds at 0° and 45° angles of fabrication was investigated in comparison to previously validated [40] as-built scaffolds and plastic control. To analysed the osteogenic differenti-ation of pre-osteoblastic MC3T3-E1 cell line cultured for 30 days in the mineralization medium, total RNA was collected from cells adhered on each substrate. Then, gene ex-pression of several markers involved in osteogenesis (Mepe, Bsp, Opn, and Ocn) was determined performing quantitative real-time RT-PCR (qPCR)

The relative quantification (RQ) of osteogenic target genes was calculated by the $2-\Delta\Delta Ct$ method, using the constitutive gene expression of the same markers obtained from cells cultured in basal medium as calibrator (RQ calibrator = 1). Fig. 7 shows the RQ results as mean of three different experiments (n=3) for plastic dish (positive control) and As-built and Etched scaffolds (both 0° and 45° angles of fabrication). All the genes tested are induced in all samples in comparison to the basal level expression (RQ = 1), sign that a positive mineralization process occurred. No statistically signifi-cant differences are detected for Mepe and Bsp gene expression between control and titanium substrates. An opposite trend is observed for the Opn and Ocn gene expres-sion: these markers show statistically significant dissimilar expression in cells collected from titanium scaffolds in comparison to the ones collected from plastic dish.

Specifically, the Ocn gene expression on As-built and Etched substrates shows a significant increase with respect to the control group, more evident for the Etched sub-strates with higher angle of fabrication (p-value < 0.001). On the contrary, the Opn gene expression on the scaffold groups is significantly reduced in comparison to the control group (p-value < 0.05). Since it is known in literature that Ocn is a late-stage marker of osteoblastic differentiation, typical of mature osteoblasts, whereas Opn is commonly defined as early markers of osteogenic differentiation [49], the gene expres-sion trend observed, reflects and confirms an accelerating in the mineralization pro-cess of the MC3T3-E1 cells grown on titanium scaffolds versus cells cultured in plastic well [40]. Finally, the statistical analysis comparing the gene expression of the cells grown on the As-built substrates and on the ones treated does not show any significant difference in terms of mineralization potential for any angles of fabrication.

5.1.4 Discussion

Surface modification of a scaffold for biological application can be done using different techniques and approaches [50–52]. The manufacturing process analyzed in this paper includes some critical aspect because a particular production technology, SLM technique, is integrated with two different post-process treatments, anodization and passivation, i.e. acid etching. All the powder bed fusion techniques results in com-plex thermal properties and significant temperature gradients that make the products surface conditions difficult to optimize, moreover, the treatments add variables to the process. Due to this reason, it is challenging to guarantee the uniformity of the product characteristics and the repeatability of the whole process, essential aspects to adopt metal AM methods as industrial processes.

The transformation of the microstructure carried on by the combination of the SLM process parameters, specifically the building angle, followed by chemical and physical modification with anodization and etching in the post-processing phase, generates relevant outcomes [39].

The surface microstructure of as-built SLM samples shows how the building an-gles used had an impact on their attributes, in fact several studies have shown how, in a metal part, mechanical and chemical surface properties can be significantly altered by the building angle of a melting process [30,37]. But the key to enhance the product's surface characteristics for biomedical applications

is adding post-process treatments. The two processes that are most frequently used to modify AM metal implants are anodization and acid etching. To determine the relationship between the manufacturing process and the post-process treatments, two building angles (0° and 45°) were studied according to previous research [40].

The surfaces of the SLM as-built samples, at two distinct building angles, appears macroscopically identical when compared to each other, and both show the presence of partially melted particles seen across the whole surface area of the top faces. Particularly, according to this study [24] the surfaces of the parts with a building angle at 0° exhibit equally distributed particles, whereas the surfaces of the parts with a building angle at 45° exhibit less uniform distribution and the presence of larger-sized agglomerates of particles (Fig. 1). This surface condition is supported by the measurement of roughness; in fact, the Sa value of the parts with a 45° building angle is higher com-pared to the other samples with a lower building angle (Table 3). For both the building angles, the CA measurements highlight the hydrophobicity of the SLM as-built samples, and the values result comparable (Table 2). Due to these similarities, there hasn't been any significant difference in the viability values of MC3T3-E1 cells between the SLM as-built samples for either building angle (Fig. 5). The biocompatibility previously demonstrated [40] was verified by cells on the SLM as-built scaffolds.

The impact of surface modification on biological performance is most noticeable on samples that have been treated. In general, similar amounts of cellular metabolic activity are evaluated for SLM as-built and etched samples, but for the anodized scaffolds, a undeniable contrast between the plastic control and the cells metabolic activity is seen (Fig. 6).

The anodized samples have a adequate uniform particle distribution for the 0° samples, but when the angle is increased to 45°, the particle distribution becomes random with the formation of clusters and the appearance of cracks on the surface of the particles (Fig. 1). This is also demonstrated by the hydrophobicity, which is significantly reduced compared to the samples as-built, notably for the 45° angle (Table 2). Compared to the as-built samples, the roughness is comparable for both building angles and is decreased (Table 3).

In contrast, the etched scaffolds exhibit a morphological surface that is smooth, with roughness and hydrophobicity values that are lower when compared to anodized samples built at 0° but higher when built at 45° (Table 2), according to this study [39] where is highlighted that the ideal implant surface have to be smooth to avoid bacterial proliferation, but at the same time with uniform micro-structure to promote cell adhesion.

The application of post-process treatments is not affected by the building angle of the specimen. In fact, it is not possible to find a direct relation between build angle and the other parameter used to describe the surface, mainly because the application of post-process treatments creates a strong alteration of the surface that makes the effect of the building angle irrelevant. Roughness decreases with treatments, but when evaluating the values in relation to the build angles, it has an opposite trend depending on the treatment applied (Fig. 3). Also the CA values has no significant relation with the building angle (Fig. 2). For a more functional evaluation of surface performance for biomedical applications, cell viability studies are necessary. Titanium substrates biocompatibility has been analyzed using an rATP assay kit that measure the number of metabolically active and viable cells in culture. The rATP test has been performed in a direct way (cells were seeded directly on the sterilized titanium substrates) and in an indirect way (autoclaved titanium substrates were placed in medium for 5 days, then the conditioned medium was used to grow cells). In both conditions, the results of the rATP assay showed a robust decrease of cellular viability for the anodized samples. No cells alive were in fact detected in culture already after 24

hours (Fig. 5 and 6). Conversely, biocompatibility of as-built specimens and specimens after acid etching treatment was confirmed (Fig. 5 and 6). Taking in account the high cellular mortal-ity showed also with the indirect rATP assay is plausible that the cellular death is not related to an adhesion problem to the scaffold but to some cytotoxic agents probably derived from the post-processing of the samples, resistant to the autoclaving, that are released in the medium culture from the anodized substrates' surface. The post-processing for the Anodized Titanium 3D samples consist in the fabrication of an oxide layer using an electrochemical anodization setup composed by a counter electrode of Ti flat foil and Ti 3D implant immersed in ethylene glycol electrolyte, contain-ing 1% water and 0.3% NH4F. Further studies are needed to identify which reagent of this treatment can be toxic.
Finally, it is shown that there is an acceleration in the mineralization process of the MC3T3-E1 cells grown on titanium scaffolds versus cells cultured in plastic well (Fig. 7). At the present time it is difficult to properly compare the approaches utilised for the surface treatment of 3D printed implants intended to promote cell adhesion and mineralization [53]. The chemical and physical characteristics of the surfaces also play a significant role in maintaining the viability of the osteoblasts, many aspects of these interactions require more investigation to resolve areas of uncertainty on the interaction between the treated surfaces and the cells. To completely comprehend these linkages, research needs to focus on diverse design aspects using various combination of manufacturing processes and surface treatments.

5.1.5 Conclusions

In this paper, the examination of AM properties on the bio-compatibility of Ti6Al4V parts is reported. The porosity and surface conditions of an implant can be tuned in order to facilitate and promote osteointegration. This is especially true of parts that can be produced utilizing the PBF process and the SLM technique. The discontinuous melting of the powder during the building process, which results in uncontrolled and partially melted particles on the surface and conditions the surface area of the scaffold, is one of the main drawbacks of these methods. A lot of research have focused on changing the process parameter and including post-process treatments as a result of these aspects. The examined solutions focus on changing the building angle during SLM operations (0° and 45°) and two treatments, anodizing and acid etching, to regulate and customize the surface properties of the metal parts. Due to the initial identical surface topography, it was discovered that the building angle has little effects on the trends of cell attachment and differentiation ($p > 0.05$). The key finding of this study is based on osteoblast metabolic activity and differentiation data, which show a clear distinction between samples after acid etching and anodization. In particular, it was discovered that SLM as-built samples are more biocompatible than post-processed ones. In comparison to the control on plastic, the cell viability on SLM Etched is lower ($p < 0.05$; Fig. 5). The metabolic activity on the anodized samples significantly decreases, leading to substantial levels of cytotoxicity with no cellular survival as a result (p value < 0.0001; Fig. 5 and Fig. 6). A successful mineralization process took place on the as-built and etched scaffolds. In particular, when com-paring cells cultured in plastic wells with cells grown on titanium scaffolds, the gene expression trend observed reflects and validates an acceleration of the mineralization process, for any manufacturing angle (Fig. 7). This issue needs to be examined in more detail in order to optimize the procedure and produce results that are more tar-geted to biological applications. In fact, it could be seen as a benefit for the osseointegration of intricate components in a custom implant. Additionally, mineralization can be advantageous for the

majority of orthopedic implants, but it could be detrimental for short-term removable components. The study of the findings of this research on bacterial adhesion [54], a crucial factor for this application, will be taken into account in future investigations.
In conclusion, in relation to the SLM design technique utilized in production, post-processing treatments have a significant impact on the characteristics of 3D printed implants.

Conclusions

This thesis focused on examining several biomanufacturing technologies in order to optimize the manufacture of 3D scaffolds for TE applications. The study centred around three distinct additive manufacturing techniques: ES, EBB, and LPBF; used alongside materials of contrasting compositions, such as inorganic polymers, synthetic and natural hydrogels, and metal alloys, specifically: TG Silicone, inorganic polymer; PVA-based synthetic hydrogels with GO as additive; Alginate-based natural hydrogels with CMC and mFC as additives; Alginate/Gelatine-based bioinks with PBS and IMD as solvents; Ti6Al4V, metal alloy.

To enhance the efficiency of biomanufacturing procedures, the research focused primarily on identifying process parameters that would have an equivalent impact on the material's printability and the process's biocompatibility. This approach allowed for the creation of a geometrically pleasing structure through the printing process.
The use of synthetic or natural hydrogels, inorganic polymers, and metal alloys has facilitated the investigation of printing factors that significantly impact the structural quality and geometry.
Conversely, the utilisation of bioinks and cellular material has enabled research into the printing of cells and the bicompatibility of the structures themselves, as in the case of cell seeding; these are the parameters that have the greatest impact on cell viability while ensuring a minimum degree of geometric stability.

The study of different manufacturing techniques has facilitated an understanding of their respective limitations and compatibility, as well as the assessment of potential multimodal applications, such as employing both ES and EBB processing for the same material.
To determine the most suitable parameter for producing two different types of structures, micro-scale structures with ES and macro-scale structures with 3D BP were created using the same hydrogel. This versatile production process can be utilised in several biological applications, specifically TE, in order to replicate native tissue.
ES studies have demonstrated the efficacy of the PVA/GO hydrogel for fibre production, particularly with a high level of GO integration. The optimal parameter combination was a flow rate of 0.1 mL/h, a needle tip-to-collector distance of 90 mm, and a voltage of 20 kV.
BP experiments demonstrated the stability of the PVA/GO hydrogel, however, to realise the deposition of many layers, it was essential to clarify several important factors. It is important to consider the start and end points of material deposition in a 3D BP process, as the start and end stages can lead to material build-up, which can interrupt continuous deposition. Cooling the printing plate can ensure both the durability of its structure and the efficient transfer of cold to the overlapping layers. In addition, the presence of air bubbles is a significant problem, as an increase in PVA concentration to 30 per cent resulted in filament defects. To solve this problem, one potential approach would be to consider the use of a solution drying technique. Filaments produced at constant pressure (1 bar) and variable speed (5÷6.25 mm/s) show a thin and consistent nature, highlighting the need to cool the printing plate to improve structural durability and optimise the composite solution.

It became evident during the initial print tests that the Envisiontec 3D-Bioplotter®, which was utilised to implement the EBB technology, required an optimisation procedure for printing novel materials, especially ad hoc designed materials that were not commercially available.
Analysed the TG Silicone given by Envisiontec utilising the low temperature head of the printer during the extrusion process. An optical microscope was used to analyse the diameter of the extruded filament in order to assess the variability of the diameter of the extruded silicone strands in relation to the diameter of the chosen nozzle. Three tunings were conducted using varying combinations of pressure and speed. The experimental results demonstrated that the displacement in the z-axis has a significant impact on the extruded diameter, with a variation of up to 10%. Optimal precision was achieved by using a pressure of 2 bars and a speed ranging from 14 to 16 mm/s. The dispensing pressure should be calibrated to match the hardening rate of the material, since a low rate will produce thinner and more circular strands, while a rapid rate will result in wider and more oval-shaped strands. The optimal condition was attained when the material exits from the nozzle and immediately comes into contact with the plate. This significantly impacts the dimensions of the filaments deposited during multi-layer printing experiments and alters the stability area of the employed material.

The analysis of several 3D printing procedures to ensure the stability of self-supporting products, even using soft materials, proved to be the most challenging aspect of the study, in fact the research progressed to focus on the hydrogel, which is considered the most biologically interesting type of material.
This category of materials necessitates both the optimisation of the BP stage and a further post-processing stage to ensure that the moulded structures maintain their intended shape.
Initially, it was recognised that the addition of a crosslinking phase was necessary in order to enable the material to undergo gelation or solidification, while maintaining the required shape throughout and after the BP process.
The use of temperature was essential in achieving precise control over the printing process of Gelatin-based hydrogels (or bioinks). By carefully manipulating the temperature during the BP phase, it was possible to establish a certain range within which the material could be successfully printed. The crosslinking procedure posed significant practical challenges in the case of Alginate-based hydrogels. The integration of the 3D FRESH printing method enabled the implementation of a technique that would permit the crosslinker ($CaCl_2$) to function during the printing phase of Alginate-based hydrogels.
The investigation was conducted on the use of 3D FRESH printing in a Gelatin-based bath for the production of Alginate-Cellulose-based hydrogels. The hydrogels were composed of CMC and mFC, combined with SA. The study of various crosslinker ($CaCl_2$) concentration in the bath and post-crosslinking process was a challenging task.
The printability index Pr was used as a measure to evaluate the printed samples and to compare them with the ratios of swelling and water uptake. The most exceptional overall results were observed for SA-CMC at $CaCl_2$ (30 mM + 1.0 w/w%), with a Pr value of 1.021. The swelling ratio and water uptake after 48 hours were 5.99 and 88%, respectively.

After optimising different printing methods, the research concentrated on creating a bioink that could efficiently sustain cell survival, growth, and function. The production of these bioinks was intricate and hinged on various factors, such as cross-linking, shear stress, hydrogel viscosity, and printing circumstances. In order to achieve this objective, various bioinks were examined to

evaluate their ability to be printed and the viability of the cells within them. The findings suggest that rapid crosslinking rates are unsuitable for the development of 3D structures incorporating cells, either because of the presence of crosslinkers or the high proportion of alginate and gelatin. The most effective bioinks are those that have a low viscosity, allowing them to be gelled only by temperature during the printing process and requiring just brief periods of post-process crosslinking. Thoroughly assessing the biocompatibility of the hydrogel in bioprinting is crucial. The conventional Live/Dead staining method for imaging is typically effective only in the initial stages. To obtain a more comprehensive evaluation, the ATP test was performed, which measures the actual metabolic activity.
To ensure the precision of each bioprinted model, it is essential to consider the quantity of cells placed, as this significantly influences their ability to proliferate effectively.

The optimisation of biomanufacturing technologies is primarily hindered by the challenge of achieving biocompatibility.
One aspect of the research focused on investigating how the features of AM affect the biocompatibility of Ti6Al4V components. One can modify the porosity and surface characteristics of implants to enhance osteointegration, especially for components manufactured utilising the LPBF method and SLM technique. Nevertheless, the occurrence of intermittent powder melting throughout the construction process can result in unregulated particles appearing on the surface, so impacting the surface area of the scaffold. The findings indicate that altering the building angle in SLM operations and employing anodizing and acid etching procedures can effectively control and tailor the surface characteristics of the metal components. The as-built samples exhibited greater biocompatibility compared to the post-processed samples, as seen by lower cell survival and decreased metabolic activity. Mineralization was achieved successfully on both the original and treated scaffolds, as evidenced by gene expression patterns that indicated a hastening of the process.

In conclusion, the research suggests that by further investigating and refining the biomanufacturing procedures and materials, it is possible to achieve the goal of developing a 3D scaffold with bioink for tissue replication. However, additional study is needed to improve the methodology and obtain more accurate results for biological applications:

- mineralization can be beneficial for most orthopaedic implants, but it may have negative consequences on detachable components in the near future, studying bacterial adhesion is essential for ensuring the effective manufacturing of implants;
- post-processing techniques exert a substantial influence on the properties of 3D printed implants;
- 3D scaffolds composed of bioink require examinations to evaluating the mechanical characteristics of printed meshes and analysing the adhesion and proliferation of cells.

Additionally, further investigations will analyse alternative hydrogels compositions and cross-linking techniques in order to enhance the longevity of the 3D framework and enhance cell viability.

References

Chapter 1 – 2 – 3

[1] M.A. Rabalo, E.M. Rubio, B. Agustina, A.M. Camacho, Hybrid additive and subtractive manufacturing: evolution of the concept and last trends in research and industry, Procedia CIRP 118 (2023) 741–746. https://doi.org/10.1016/j.procir.2023.06.127.

[2] S. Park, W. Shou, L. Makatura, W. Matusik, K. (Kelvin) Fu, 3D printing of polymer composites: Materials, processes, and applications, Matter 5 (2022) 43–76. https://doi.org/10.1016/j.matt.2021.10.018.

[3] R. Krishna, M. Manjaiah, C.B. Mohan, Developments in additive manufacturing, in: Addit Manuf, Elsevier, 2021: pp. 37–62. https://doi.org/10.1016/B978-0-12-822056-6.00002-3.

[4] T.D. Ngo, A. Kashani, G. Imbalzano, K.T.Q. Nguyen, D. Hui, Additive manufacturing (3D printing): A review of materials, methods, applications and challenges, Compos B Eng 143 (2018) 172–196. https://doi.org/10.1016/j.compositesb.2018.02.012.

[5] Y.-H.P. Zhang, J. Sun, Y. Ma, Biomanufacturing: history and perspective, J Ind Microbiol Biotechnol 44 (2017) 773–784. https://doi.org/10.1007/s10295-016-1863-2.

[6] J.L. Olson, A. Atala, J.J. Yoo, Tissue Engineering: Current Strategies and Future Directions, Chonnam Med J 47 (2011) 1. https://doi.org/10.4068/cmj.2011.47.1.1.

[7] C. Jensen, Y. Teng, Is It Time to Start Transitioning From 2D to 3D Cell Culture?, Front Mol Biosci 7 (2020). https://doi.org/10.3389/fmolb.2020.00033.

[8] R. Langer, J.P. Vacanti, Tissue Engineering, Science (1979) 260 (1993) 920–926. https://doi.org/10.1126/science.8493529.

[9] V. Mironov, N. Reis, B. Derby, Review: Bioprinting: A Beginning, Tissue Eng 12 (2006) 631–634. https://doi.org/10.1089/ten.2006.12.631.

[10] Z. Gu, J. Fu, H. Lin, Y. He, Development of 3D bioprinting: From printing methods to biomedical applications, Asian J Pharm Sci 15 (2020) 529–557. https://doi.org/10.1016/j.ajps.2019.11.003.

[11] V. Mironov, R.P. Visconti, V. Kasyanov, G. Forgacs, C.J. Drake, R.R. Markwald, Organ printing: Tissue spheroids as building blocks, Biomaterials 30 (2009) 2164–2174. https://doi.org/10.1016/j.biomaterials.2008.12.084.

[12] S. Tripathi, S.S. Mandal, S. Bauri, P. Maiti, 3D bioprinting and its innovative approach for biomedical applications, MedComm (Beijing) 4 (2023). https://doi.org/10.1002/mco2.194.

[13] M.M. Farag, Recent trends on biomaterials for tissue regeneration applications: review, J Mater Sci 58 (2023) 527–558. https://doi.org/10.1007/s10853-022-08102-x.

[14] N. Liu, X. Zhang, Q. Guo, T. Wu, Y. Wang, 3D Bioprinted Scaffolds for Tissue Repair and Regeneration, Front Mater 9 (2022). https://doi.org/10.3389/fmats.2022.925321.

[15] J. Chen, D. Zhang, L.-P. Wu, M. Zhao, Current Strategies for Engineered Vascular Grafts and Vascularized Tissue Engineering, Polymers (Basel) 15 (2023) 2015. https://doi.org/10.3390/polym15092015.

[16] M. Mitsuishi, J. Cao, P. Bártolo, D. Friedrich, A.J. Shih, K. Rajurkar, N. Sugita, K. Harada, Biomanufacturing, CIRP Annals 62 (2013) 585–606. https://doi.org/10.1016/j.cirp.2013.05.001.

[17] I.M. Adel, M.F. ElMeligy, N.A. Elkasabgy, Conventional and Recent Trends of Scaffolds Fabrication: A Superior Mode for Tissue Engineering, Pharmaceutics 14 (2022) 306. https://doi.org/10.3390/pharmaceutics14020306.

[18] S. Rouf, A. Malik, N. Singh, A. Raina, N. Naveed, M.I.H. Siddiqui, M.I.U. Haq, Additive manufacturing technologies: Industrial and medical applications, Sustainable Operations and Computers 3 (2022) 258–274. https://doi.org/10.1016/j.susoc.2022.05.001.

[19] S.I. Abd Razak, I.F. Wahab, F. Fadil, F.N. Dahli, A.Z. Md Khudzari, H. Adeli, A Review of Electrospun Conductive Polyaniline Based Nanofiber Composites and Blends: Processing Features, Applications, and Future Directions, Advances in Materials Science and Engineering 2015 (2015) 1–19. https://doi.org/10.1155/2015/356286.

[20] P. Ginestra, E. Ceretti, A. Fiorentino, Electrospinning of Poly-caprolactone for Scaffold Manufacturing: Experimental Investigation on the Process Parameters Influence, Procedia CIRP 49 (2016) 8–13. https://doi.org/10.1016/j.procir.2015.07.020.

[21] M. Tahir, S. Vicini, A. Sionkowska, Electrospun Materials Based on Polymer and Biopolymer Blends—A Review, Polymers (Basel) 15 (2023) 1654. https://doi.org/10.3390/polym15071654.

[22] M.Z.A. Zulkifli, D. Nordin, N. Shaari, S.K. Kamarudin, Overview of Electrospinning for Tissue Engineering Applications, Polymers (Basel) 15 (2023) 2418. https://doi.org/10.3390/polym15112418.

[23] P. Ginestra, L. Riva, A. Fiorentino, D. Zappa, E. Comini, E. Ceretti, Electrospinning of Poly(vinyl alcohol)-Graphene oxide aligned fibers, Procedia CIRP 89 (2020) 110–115. https://doi.org/10.1016/j.procir.2020.05.126.

[24] X.-X. Wang, G.-F. Yu, J. Zhang, M. Yu, S. Ramakrishna, Y.-Z. Long, Conductive polymer ultrafine fibers via electrospinning: Preparation, physical properties and applications, Prog Mater Sci 115 (2021) 100704. https://doi.org/10.1016/j.pmatsci.2020.100704.

[25] A. Bachs-Herrera, O. Yousefzade, L.J. del Valle, J. Puiggali, Melt Electrospinning of Polymers: Blends, Nanocomposites, Additives and Applications, Applied Sciences 11 (2021) 1808. https://doi.org/10.3390/app11041808.

[26] Z. Xie, M. Gao, A.O. Lobo, T.J. Webster, 3D Bioprinting in Tissue Engineering for Medical Applications: The Classic and the Hybrid, Polymers (Basel) 12 (2020) 1717. https://doi.org/10.3390/polym12081717.

[27] E.S. Bishop, S. Mostafa, M. Pakvasa, H.H. Luu, M.J. Lee, J.M. Wolf, G.A. Ameer, T.-C. He, R.R. Reid, 3-D bioprinting technologies in tissue engineering and regenerative medicine: Current and future trends, Genes Dis 4 (2017) 185–195. https://doi.org/10.1016/j.gendis.2017.10.002.

[28] F. Liu, R. Quan, C. Vyas, E. Aslan, Hybrid biomanufacturing systems applied in tissue regeneration, Int J Bioprint 9 (2022) 646. https://doi.org/10.18063/ijb.v9i1.646.

[29] S. Tian, H. Zhao, N. Lewinski, Key parameters and applications of extrusion-based bioprinting, Bioprinting 23 (2021) e00156. https://doi.org/10.1016/j.bprint.2021.e00156.

[30] G. Gillispie, P. Prim, J. Copus, J. Fisher, A.G. Mikos, J.J. Yoo, A. Atala, S.J. Lee, Assessment methodologies for extrusion-based bioink printability, Biofabrication 12 (2020) 022003. https://doi.org/10.1088/1758-5090/ab6f0d.

[31] M. Xie, J. Su, S. Zhou, J. Li, K. Zhang, Application of Hydrogels as Three-Dimensional Bioprinting Ink for Tissue Engineering, Gels 9 (2023) 88. https://doi.org/10.3390/gels9020088.

[32] S.L. Sing, W.Y. Yeong, Laser powder bed fusion for metal additive manufacturing: perspectives on recent developments, Virtual Phys Prototyp 15 (2020) 359–370. https://doi.org/10.1080/17452759.2020.1779999.
[33] C.Y. Yap, C.K. Chua, Z.L. Dong, Z.H. Liu, D.Q. Zhang, L.E. Loh, S.L. Sing, Review of selective laser melting: Materials and applications, Appl Phys Rev 2 (2015). https://doi.org/10.1063/1.4935926.
[34] P. Ninpetch, P. Kowitwarangkul, S. Mahathanabodee, P. Chalermkarnnon, P. Ratanadecho, A review of computer simulations of metal 3D printing, in: 2020: p. 050002. https://doi.org/10.1063/5.0022974.
[35] W. Wei, W. Wu, S. Fan, X. Duan, In-situ laser additive manufacturing of Ti6Al4V matrix composites by gas–liquid reaction in dilute nitrogen gas atmospheres, Mater Des 202 (2021) 109578. https://doi.org/10.1016/j.matdes.2021.109578.
[36] R. Pal, A. Basak, Linking Powder Properties, Printing Parameters, Post-Processing Methods, and Fatigue Properties in Additive Manufacturing of AlSi10Mg, Alloys 1 (2022) 149–179. https://doi.org/10.3390/alloys1020010.
[37] L.E. Murr, Metallurgy principles applied to powder bed fusion 3D printing/additive manufacturing of personalized and optimized metal and alloy biomedical implants: an overview, Journal of Materials Research and Technology 9 (2020) 1087–1103. https://doi.org/10.1016/j.jmrt.2019.12.015.
[38] J. Guan, Q. Wang, Laser Powder Bed Fusion of Dissimilar Metal Materials: A Review, Materials 16 (2023) 2757. https://doi.org/10.3390/ma16072757.
[39] K. Tappa, U. Jammalamadaka, Novel Biomaterials Used in Medical 3D Printing Techniques, J Funct Biomater 9 (2018) 17. https://doi.org/10.3390/jfb9010017.
[40] V. Mironov, Printing technology to produce living tissue, Expert Opin Biol Ther 3 (2003) 701–704. https://doi.org/10.1517/14712598.3.5.701.
[41] J. Groll, J.A. Burdick, D.-W. Cho, B. Derby, M. Gelinsky, S.C. Heilshorn, T. Jüngst, J. Malda, V.A. Mironov, K. Nakayama, A. Ovsianikov, W. Sun, S. Takeuchi, J.J. Yoo, T.B.F. Woodfield, A definition of bioinks and their distinction from biomaterial inks, Biofabrication 11 (2018) 013001. https://doi.org/10.1088/1758-5090/aaec52.
[42] A.M. Smith, S. Moxon, G.A. Morris, Biopolymers as wound healing materials, in: Wound Healing Biomaterials, Elsevier, 2016: pp. 261–287. https://doi.org/10.1016/B978-1-78242-456-7.00013-1.
[43] M. Yang, Z. Wang, M. Li, Z. Yin, H.A. Butt, The synthesis, mechanisms, and additives for bio-compatible polyvinyl alcohol hydrogels: A review on current advances, trends, and future outlook, Journal of Vinyl and Additive Technology 29 (2023) 939–959. https://doi.org/10.1002/vnl.21962.
[44] O. Frent, L. Vicas, N. Duteanu, C. Morgovan, T. Jurca, A. Pallag, M. Muresan, S. Filip, R.-L. Lucaciu, E. Marian, Sodium Alginate—Natural Microencapsulation Material of Polymeric Microparticles, Int J Mol Sci 23 (2022) 12108. https://doi.org/10.3390/ijms232012108.
[45] S.Lj. Tomić, M.M. Babić Radić, J.S. Vuković, V. V. Filipović, J. Nikodinovic-Runic, M. Vukomanović, Alginate-Based Hydrogels and Scaffolds for Biomedical Applications, Mar Drugs 21 (2023) 177. https://doi.org/10.3390/md21030177.
[46] H. Andriamanantoanina, M. Rinaudo, Relationship between the molecular structure of alginates and their gelation in acidic conditions, Polym Int 59 (2010) 1531–1541. https://doi.org/10.1002/pi.2943.

[47] K.Y. Lee, D.J. Mooney, Alginate: Properties and biomedical applications, Prog Polym Sci 37 (2012) 106–126. https://doi.org/10.1016/j.progpolymsci.2011.06.003.
[48] H.H. Tønnesen, J. Karlsen, Alginate in Drug Delivery Systems, Drug Dev Ind Pharm 28 (2002) 621–630. https://doi.org/10.1081/DDC-120003853.
[49] N. Devina, Y.K. Eriwati, A.S. Santosa, The purity and viscosity of sodium alginate extracted from *Sargassum* brown seaweed species as a basic ingredient in dental alginate impression material, J Phys Conf Ser 1073 (2018) 052012. https://doi.org/10.1088/1742-6596/1073/5/052012.
[50] S. Masri, M. Maarof, I.A. Aziz, R. Idrus, M.B. Fauzi, Performance of hybrid gelatin-PVA bioinks integrated with genipin through extrusionbased 3D bioprinting: An in vitro evaluation using human dermal fibroblasts, Int J Bioprint 9 (2023) 677. https://doi.org/10.18063/ijb.677.
[51] C.-Y. Huang, K.-H. Hu, Z.-H. Wei, Comparison of cell behavior on pva/pva-gelatin electrospun nanofibers with random and aligned configuration, Sci Rep 6 (2016) 37960. https://doi.org/10.1038/srep37960.
[52] J. Poppe, Gelatin, in: Thickening and Gelling Agents for Food, Springer US, Boston, MA, 1992: pp. 98–123. https://doi.org/10.1007/978-1-4615-3552-2_5.
[53] K.B. Djagny, Z. Wang, S. Xu, Gelatin: A Valuable Protein for Food and Pharmaceutical Industries: Review, Crit Rev Food Sci Nutr 41 (2001) 481–492. https://doi.org/10.1080/20014091091904.
[54] F. Mushtaq, Z.A. Raza, S.R. Batool, M. Zahid, O.C. Onder, A. Rafique, M.A. Nazeer, Preparation, properties, and applications of gelatin-based hydrogels (GHs) in the environmental, technological, and biomedical sectors, Int J Biol Macromol 218 (2022) 601–633. https://doi.org/10.1016/j.ijbiomac.2022.07.168.
[55] P. Jaipan, A. Nguyen, R.J. Narayan, Gelatin-based hydrogels for biomedical applications, MRS Commun 7 (2017) 416–426. https://doi.org/10.1557/mrc.2017.92.
[56] C.F. Mok, Y.C. Ching, F. Muhamad, N.A. Abu Osman, N.D. Hai, C.R. Che Hassan, Adsorption of Dyes Using Poly(vinyl alcohol) (PVA) and PVA-Based Polymer Composite Adsorbents: A Review, J Polym Environ 28 (2020) 775–793. https://doi.org/10.1007/s10924-020-01656-4.
[57] Y. He, F. Yang, H. Zhao, Q. Gao, B. Xia, J. Fu, Research on the printability of hydrogels in 3D bioprinting, Sci Rep 6 (2016) 29977. https://doi.org/10.1038/srep29977.
[58] S. Naghieh, X. Chen, Printability–A key issue in extrusion-based bioprinting, J Pharm Anal 11 (2021) 564–579. https://doi.org/10.1016/j.jpha.2021.02.001.
[59] F. You, X. Wu, X. Chen, 3D printing of porous alginate/gelatin hydrogel scaffolds and their mechanical property characterization, International Journal of Polymeric Materials and Polymeric Biomaterials 66 (2017) 299–306. https://doi.org/10.1080/00914037.2016.1201830.
[60] X.B. Chen, A. Fazel Anvari-Yazdi, X. Duan, A. Zimmerling, R. Gharraei, N.K. Sharma, S. Sweilem, L. Ning, Biomaterials / bioinks and extrusion bioprinting, Bioact Mater 28 (2023) 511–536. https://doi.org/10.1016/j.bioactmat.2023.06.006.
[61] S. Bom, R. Ribeiro, H.M. Ribeiro, C. Santos, J. Marto, On the progress of hydrogel-based 3D printing: Correlating rheological properties with printing behaviour, Int J Pharm 615 (2022) 121506. https://doi.org/10.1016/j.ijpharm.2022.121506.

[62] A. Ahmadi Soufivand, J. Faber, J. Hinrichsen, S. Budday, Multilayer 3D bioprinting and complex mechanical properties of alginate-gelatin mesostructures, Sci Rep 13 (2023) 11253. https://doi.org/10.1038/s41598-023-38323-2.

[63] S.F. bt Ibrahim, N.A.N. Mohd Azam, K.A. Mat Amin, Sodium alginate film: the effect of crosslinker on physical and mechanical properties, IOP Conf Ser Mater Sci Eng 509 (2019) 012063. https://doi.org/10.1088/1757-899X/509/1/012063.

[64] L. Aguero, S. Alpdagtas, E. Ilhan, D. Zaldivar-Silva, O. Gunduz, Functional role of crosslinking in alginate scaffold for drug delivery and tissue engineering: A review, Eur Polym J 160 (2021) 110807. https://doi.org/10.1016/j.eurpolymj.2021.110807.

[65] T.J. Hinton, Q. Jallerat, R.N. Palchesko, J.H. Park, M.S. Grodzicki, H.-J. Shue, M.H. Ramadan, A.R. Hudson, A.W. Feinberg, Three-dimensional printing of complex biological structures by freeform reversible embedding of suspended hydrogels, Sci Adv 1 (2015). https://doi.org/10.1126/sciadv.1500758.

[66] M. Janmaleki, J. Liu, M. Kamkar, M. Azarmanesh, U. Sundararaj, A.S. Nezhad, Role of temperature on bio-printability of gelatin methacryloyl bioink in two-step cross-linking strategy for tissue engineering applications, Biomedical Materials 16 (2021) 015021. https://doi.org/10.1088/1748-605X/abbcc9.

[67] L. Xiang, W. Cui, Biomedical application of photo-crosslinked gelatin hydrogels, Journal of Leather Science and Engineering 3 (2021) 3. https://doi.org/10.1186/s42825-020-00043-y.

[68] A. Zennifer, S. Manivannan, S. Sethuraman, S.G. Kumbar, D. Sundaramurthi, 3D bioprinting and photocrosslinking: emerging strategies & future perspectives, Biomaterials Advances 134 (2022) 112576. https://doi.org/10.1016/j.msec.2021.112576.

[69] J. Saroia, W. Yanen, Q. Wei, K. Zhang, T. Lu, B. Zhang, A review on biocompatibility nature of hydrogels with 3D printing techniques, tissue engineering application and its future prospective, Biodes Manuf 1 (2018) 265–279. https://doi.org/10.1007/s42242-018-0029-7.

[70] S.M. Hull, L.G. Brunel, S.C. Heilshorn, 3D Bioprinting of Cell-Laden Hydrogels for Improved Biological Functionality, Advanced Materials 34 (2022). https://doi.org/10.1002/adma.202103691.

[71] P. Bartolo, A. Malshe, E. Ferraris, B. Koc, 3D bioprinting: Materials, processes, and applications, CIRP Annals 71 (2022) 577–597. https://doi.org/10.1016/j.cirp.2022.06.001.

[72] D. Maiti, X. Tong, X. Mou, K. Yang, Carbon-Based Nanomaterials for Biomedical Applications: A Recent Study, Front Pharmacol 9 (2019). https://doi.org/10.3389/fphar.2018.01401.

[73] L.E. Mulko, E.A. Cuello, R. Baumann, A.R. Ramuglia, I.M. Weidinger, D.F. Acevedo, C.A. Barbero, M. Molina, A.F. Lasagni, On the design and development of foamed GO-hydrogel nanocomposite surfaces by ultra-short laser processing, Nanotechnology 34 (2023) 245701. https://doi.org/10.1088/1361-6528/acbeb4.

[74] S.H. Ku, M. Lee, C.B. Park, Carbon-Based Nanomaterials for Tissue Engineering, Adv Healthc Mater 2 (2013) 244–260. https://doi.org/10.1002/adhm.201200307.

[75] Y.-R. He, S.-C. Li, X.-L. Li, Y. Yang, A.-M. Tang, L. Du, Z.-Y. Tan, D. Zhang, H.-B. Chen, Graphene (rGO) hydrogel: A promising material for facile removal of uranium from aqueous solution, Chemical Engineering Journal 338 (2018) 333–340. https://doi.org/10.1016/j.cej.2018.01.037.

[76] M. Ban, R. Shimoda, Y. Okigawa, M. Ishihara, Proliferation of mesenchymal stem cells by graphene-attached soft material structure, Diam Relat Mater 111 (2021) 108229. https://doi.org/10.1016/j.diamond.2020.108229.

[77] T.M. Magne, T. de Oliveira Vieira, L.M.R. Alencar, F.F.M. Junior, S. Gemini-Piperni, S. V. Carneiro, L.M.U.D. Fechine, R.M. Freire, K. Golokhvast, P. Metrangolo, P.B.A. Fechine, R. Santos-Oliveira, Graphene and its derivatives: understanding the main chemical and medicinal chemistry roles for biomedical applications, J Nanostructure Chem 12 (2022) 693–727. https://doi.org/10.1007/s40097-021-00444-3.

[78] X. Wang, H. Zhang, S. Ham, R. Qiao, Graphene Oxide and Its Derivatives as Adsorbents for PFOA Molecules, J Phys Chem B 127 (2023) 9620–9629. https://doi.org/10.1021/acs.jpcb.3c04762.

[79] H. Seddiqi, E. Oliaei, H. Honarkar, J. Jin, L.C. Geonzon, R.G. Bacabac, J. Klein-Nulend, Cellulose and its derivatives: towards biomedical applications, Cellulose 28 (2021) 1893–1931. https://doi.org/10.1007/s10570-020-03674-w.

[80] U. Ray, S. Zhu, Z. Pang, T. Li, Mechanics Design in Cellulose-Enabled High-Performance Functional Materials, Advanced Materials 33 (2021). https://doi.org/10.1002/adma.202002504.

[81] N.M. Clauser, F.E. Felissia, M.C. Area, M.E. Vallejos, Design of nano and micro fibrillated cellulose production processes from forest industrial wastes in a multiproduct biorefinery, Chemical Engineering Research and Design 167 (2021) 1–14. https://doi.org/10.1016/j.cherd.2020.12.003.

[82] A. Zennifer, P. Senthilvelan, S. Sethuraman, D. Sundaramurthi, Key advances of carboxymethyl cellulose in tissue engineering & 3D bioprinting applications, Carbohydr Polym 256 (2021) 117561. https://doi.org/10.1016/j.carbpol.2020.117561.

[83] Md.S. Rahman, Md.S. Hasan, A.S. Nitai, S. Nam, A.K. Karmakar, Md.S. Ahsan, M.J.A. Shiddiky, M.B. Ahmed, Recent Developments of Carboxymethyl Cellulose, Polymers (Basel) 13 (2021) 1345. https://doi.org/10.3390/polym13081345.

[84] S. Zheng, H. Chen, T. Zhang, Y. Yao, Y. Chen, S. Zhang, B. Bai, Gene-modified BMSCs encapsulated with carboxymethyl cellulose facilitate osteogenesis in vitro and in vivo, J Biomater Appl 35 (2021) 814–822. https://doi.org/10.1177/0885328220948030.

[85] P. Chen, F. Xie, F. Tang, T. McNally, Structure and properties of thermomechanically processed chitosan/carboxymethyl cellulose/graphene oxide polyelectrolyte complexed bionanocomposites, Int J Biol Macromol 158 (2020) 420–429. https://doi.org/10.1016/j.ijbiomac.2020.04.259.

[86] G. Sharmila, C. Muthukumaran, S. Kirthika, S. Keerthana, N.M. Kumar, J. Jeyanthi, Fabrication and characterization of Spinacia oleracea extract incorporated alginate/carboxymethyl cellulose microporous scaffold for bone tissue engineering, Int J Biol Macromol 156 (2020) 430–437. https://doi.org/10.1016/j.ijbiomac.2020.04.059.

[87] S. Sadeghi, J. Nourmohammadi, A. Ghaee, N. Soleimani, Carboxymethyl cellulose-human hair keratin hydrogel with controlled clindamycin release as antibacterial wound dressing, Int J Biol Macromol 147 (2020) 1239–1247. https://doi.org/10.1016/j.ijbiomac.2019.09.251.

[88] Phosphate-buffered saline (PBS), Cold Spring Harb Protoc 2006 (2006) pdb.rec8247. https://doi.org/10.1101/pdb.rec8247.

[89] R. Dulbecco, G. Freeman, Plaque production by the polyoma virus, Virology 8 (1959) 396–397. https://doi.org/10.1016/0042-6822(59)90043-1.

[90] H. Eagle, Amino Acid Metabolism in Mammalian Cell Cultures, Science (1979) 130 (1959) 432–437. https://doi.org/10.1126/science.130.3373.432.
[91] K. Rosińska, M. Bartniak, A. Wierzbicka, A. Sobczyk-Guzenda, D. Bociaga, Solvent types used for the preparation of hydrogels determine their mechanical properties and influence cell viability through gelatine and calcium ions release, J Biomed Mater Res B Appl Biomater 111 (2023) 314–330. https://doi.org/10.1002/jbm.b.35152.
[92] L.F. Velásquez-García, Y. Kornbluth, Biomedical Applications of Metal 3D Printing, Annu Rev Biomed Eng 23 (2021) 307–338. https://doi.org/10.1146/annurev-bioeng-082020-032402.
[93] Q. Chen, G.A. Thouas, Metallic implant biomaterials, Materials Science and Engineering: R: Reports 87 (2015) 1–57. https://doi.org/10.1016/j.mser.2014.10.001.
[94] G.A. dos Santos, The Importance of Metallic Materials as Biomaterials, Advances in Tissue Engineering & Regenerative Medicine: Open Access 3 (2017). https://doi.org/10.15406/atroa.2017.03.00054.
[95] M. Sarraf, E. Rezvani Ghomi, S. Alipour, S. Ramakrishna, N. Liana Sukiman, A state-of-the-art review of the fabrication and characteristics of titanium and its alloys for biomedical applications, Biodes Manuf 5 (2022) 371–395. https://doi.org/10.1007/s42242-021-00170-3.
[96] S. Arabnejad, B. Johnston, M. Tanzer, D. Pasini, Fully porous 3D printed titanium femoral stem to reduce stress-shielding following total hip arthroplasty, Journal of Orthopaedic Research 35 (2017) 1774–1783. https://doi.org/10.1002/jor.23445.
[97] H. Hermawan, D. Ramdan, J.R. P. Djuansjah, Metals for Biomedical Applications, in: Biomedical Engineering - From Theory to Applications, InTech, 2011. https://doi.org/10.5772/19033.
[98] V. Esfahani Yeganeh, P. Li, Effect of beam offset on microstructure and mechanical properties of dissimilar electron beam welded high temperature titanium alloys, Mater Des 124 (2017) 78–86. https://doi.org/10.1016/j.matdes.2017.03.056.
[99] W. Wei, W. Wu, S. Fan, X. Duan, In-situ laser additive manufacturing of Ti6Al4V matrix composites by gas–liquid reaction in dilute nitrogen gas atmospheres, Mater Des 202 (2021) 109578. https://doi.org/10.1016/j.matdes.2021.109578.
[100] X. Yan, W. Cao, H. Li, Biomedical Alloys and Physical Surface Modifications: A Mini-Review, Materials 15 (2021) 66. https://doi.org/10.3390/ma15010066.
[101] A. Milovanović, A. Sedmak, A. Grbović, T. Mijatović, K. Čolić, Design Aspects of Hip Implant Made of Ti-6Al-4V Extra Low Interstitials Alloy, Procedia Structural Integrity 26 (2020) 299–305. https://doi.org/10.1016/j.prostr.2020.06.038.
[102] C. Lin, T. Wirtz, F. LaMarca, S.J. Hollister, Structural and mechanical evaluations of a topology optimized titanium interbody fusion cage fabricated by selective laser melting process, J Biomed Mater Res A 83A (2007) 272–279. https://doi.org/10.1002/jbm.a.31231.
[103] A. Azmat, S. Asrar, I.A. Channa, J. Ashfaq, I. Ali Chandio, A.D. Chandio, M. Ali Shar, M.S. AlSalhi, S. Devanesan, Comparative Study of Biocompatible Titanium Alloys Containing Non-Toxic Elements for Orthopedic Implants, Crystals (Basel) 13 (2023) 467. https://doi.org/10.3390/cryst13030467.
[104] J. Guan, Q. Wang, Laser Powder Bed Fusion of Dissimilar Metal Materials: A Review, Materials 16 (2023) 2757. https://doi.org/10.3390/ma16072757.

Chapter 4

Section 4.1

[1] B. Zhang, L. Gao, L. Ma, Y. Luo, H. Yang, Z. Cui, 3D Bioprinting: A Novel Avenue for Manufacturing Tissues and Organs, Engineering 5 (2019) 777–794. https://doi.org/10.1016/J.ENG.2019.03.009.

[2] S. Derakhshanfar, R. Mbeleck, K. Xu, X. Zhang, W. Zhong, M. Xing, 3D bioprinting for biomedical devices and tissue engineering: A review of recent trends and advances, Bioact Mater 3 (2018) 144–156. https://doi.org/10.1016/J.BIOACTMAT.2017.11.008.

[3] A. Gleadall, D. Visscher, J. Yang, D. Thomas, J. Segal, Review of additive manufactured tissue engineering scaffolds: relationship between geometry and performance, Burns Trauma 6 (2018). https://doi.org/10.1186/s41038-018-0121-4.

[4] D. Gastaldi, G. Parisi, R. Lucchini, R. Contro, S. Bignozzi, P.S. Ginestra, G. Filardo, E. Kon, P. Vena, A Predictive Model for the Elastic Properties of a Collagen-Hydroxyapatite Porous Scaffold for Multi-Layer Osteochondral Substitutes, Int J Appl Mech 07 (2015) 1550063. https://doi.org/10.1142/S1758825115500635.

[5] Z.M. Jessop, A. Al-Sabah, M.D. Gardiner, E. Combellack, K. Hawkins, I.S. Whitaker, 3D bioprinting for reconstructive surgery: Principles, applications and challenges, Journal of Plastic, Reconstructive & Aesthetic Surgery 70 (2017) 1155–1170. https://doi.org/10.1016/J.BJPS.2017.06.001.

[6] Angelats Lobo, Ginestra, Cell Bioprinting: The 3D-Bioplotter™ Case, Materials 12 (2019) 4005. https://doi.org/10.3390/ma12234005.

[7] D.A. Lobo, P. Ginestra, E. Ceretti, T.P. Miquel, J. Ciurana, Cancer Cell Direct Bioprinting: A Focused Review, Micromachines (Basel) 12 (2021) 764. https://doi.org/10.3390/mi12070764.

[8] D. Bhattarai, L. Aguilar, C. Park, C. Kim, A Review on Properties of Natural and Synthetic Based Electrospun Fibrous Materials for Bone Tissue Engineering, Membranes (Basel) 8 (2018) 62. https://doi.org/10.3390/membranes8030062.

[9] F. Zhan, X. Yan, J. Li, F. Sheng, B. Li, Encapsulation of tangeretin in PVA/PAA crosslinking electrospun fibers by emulsion-electrospinning: Morphology characterization, slow-release, and antioxidant activity assessment, Food Chem 337 (2021) 127763. https://doi.org/10.1016/J.FOODCHEM.2020.127763.

[10] A. Allafchian, H. Hosseini, S.M. Ghoreishi, Electrospinning of PVA-carboxymethyl cellulose nanofibers for flufenamic acid drug delivery, Int J Biol Macromol 163 (2020) 1780–1786. https://doi.org/10.1016/J.IJBIOMAC.2020.09.129.

[11] M. Hulupi, H. Haryadi, Synthesis and Characterization of Electrospinning PVA Nanofiber-Crosslinked by Glutaraldehyde, Mater Today Proc 13 (2019) 199–204. https://doi.org/10.1016/J.MATPR.2019.03.214.

[12] H. Li, C. Tan, L. Li, Review of 3D printable hydrogels and constructs, Mater Des 159 (2018) 20–38. https://doi.org/10.1016/J.MATDES.2018.08.023.

[13] P. Orsu, A. Koyyada, Recent progresses and challenges in graphene based nano materials for advanced therapeutical applications: a comprehensive review, Mater Today Commun 22 (2020) 100823. https://doi.org/10.1016/J.MTCOMM.2019.100823.

[14] E. Ceretti, P.S. Ginestra, M. Ghazinejad, A. Fiorentino, M. Madou, Electrospinning and characterization of polymer–graphene powder scaffolds, CIRP Annals 66 (2017) 233–236. https://doi.org/10.1016/J.CIRP.2017.04.122.
[15] S. Nemati, S. Kim, Y.M. Shin, H. Shin, Current progress in application of polymeric nanofibers to tissue engineering, Nano Converg 6 (2019) 36. https://doi.org/10.1186/s40580-019-0209-y.
[16] P.D. Dalton, C. Vaquette, B.L. Farrugia, T.R. Dargaville, T.D. Brown, D.W. Hutmacher, Electrospinning and additive manufacturing: converging technologies, Biomater. Sci. 1 (2013) 171–185. https://doi.org/10.1039/C2BM00039C.
[17] X.X. Wang, G.F. Yu, J. Zhang, M. Yu, S. Ramakrishna, Y.Z. Long, Conductive polymer ultrafine fibers via electrospinning: Preparation, physical properties and applications, Prog Mater Sci 115 (2021) 100704. https://doi.org/10.1016/J.PMATSCI.2020.100704.
[18] K. Havlíček, L. Svobodová, T. Bakalova, T. Lederer, Influence of electrospinning methods on characteristics of polyvinyl butyral and polyurethane nanofibres essential for biological applications, Mater Des 194 (2020) 108898. https://doi.org/10.1016/J.MATDES.2020.108898.
[19] P.S. Ginestra, R. Rovetta, A. Fiorentino, E. Ceretti, Bioprinting process optimization: evaluation of parameters influence on the extrusion of inorganic polymers, Procedia CIRP 89 (2020) 104–109. https://doi.org/10.1016/J.PROCIR.2020.05.125.

Section 4.2

[1] P.J. Bártolo, H.A. Almeida, R.A. Rezende, T. Laoui, B. Bidanda, Advanced Processes to Fabricate Scaffolds for Tissue Engineering, in: Virtual Prototyping & Bio Manufacturing in Medical Applications, Springer US, Boston, MA, n.d.: pp. 149–170. https://doi.org/10.1007/978-0-387-68831-2_8.
[2] D. Steffens, R. Alvarenga Rezende, B. Santi, F.D. Alencar de Sena Pereira, P. Inforçatti Neto, J.V. Lopes da Silva, P. Pranke, 3D-Printed PCL Scaffolds for the Cultivation of Mesenchymal Stem Cells, J Appl Biomater Funct Mater 14 (2016) 19–25. https://doi.org/10.5301/jabfm.5000252.
[3] J.L. Dávila, M.S. Freitas, P.I. Neto, Z.C. Silveira, J.V.L. Silva, M.A. d'Ávila, Software to generate 3-D continuous printing paths for the fabrication of tissue engineering scaffolds, The International Journal of Advanced Manufacturing Technology (2015). https://doi.org/10.1007/s00170-015-7866-8.
[4] C. Mendoza-Buenrostro, H. Lara, C. Rodriguez, Hybrid Fabrication of a 3D Printed Geometry Embedded with PCL Nanofibers for Tissue Engineering Applications, Procedia Eng 110 (2015) 128–134. https://doi.org/10.1016/j.proeng.2015.07.020.
[5] P.S. Ginestra, S. Pandini, A. Fiorentino, P. Benzoni, P. Dell'Era, E. Ceretti, Microstructured scaffold for guided cellular orientation: Poly(ε-caprolactone) electrospinning on laser ablated titanium collector, CIRP J Manuf Sci Technol 19 (2017) 147–157. https://doi.org/10.1016/j.cirpj.2017.08.002.
[6] P. Ginestra, A. Fiorentino, E. Ceretti, Micro-structuring of Titanium Collectors by Laser Ablation Technique: A Promising Approach to Produce Micro-patterned Scaffolds for Tissue Engineering Applications, Procedia CIRP 65 (2017) 19–24. https://doi.org/10.1016/j.procir.2017.04.043.

[7] P.S. Ginestra, M. Madou, E. Ceretti, Production of carbonized micro-patterns by photolithography and pyrolysis, Precis Eng 55 (2019) 137–143. https://doi.org/10.1016/J.PRECISIONENG.2018.08.019.

[8] E. Ceretti, P. Ginestra, P.I. Neto, A. Fiorentino, J.V.L. Da Silva, Multi-layered Scaffolds Production via Fused Deposition Modeling (FDM) Using an Open Source 3D Printer: Process Parameters Optimization for Dimensional Accuracy and Design Reproducibility, Procedia CIRP 65 (2017) 13–18. https://doi.org/10.1016/J.PROCIR.2017.04.042.

[9] H.A. Almeida, A.F. Costa, C. Ramos, C. Torres, M. Minondo, P.J. Bártolo, A. Nunes, D. Kemmoku, J.V.L. da Silva, Additive Manufacturing Systems for Medical Applications: Case Studies, in: Additive Manufacturing – Developments in Training and Education, Springer International Publishing, Cham, 2019: pp. 187–209. https://doi.org/10.1007/978-3-319-76084-1_13.

[10] P.S. Ginestra, E. Ceretti, A. Fiorentino, Potential of modeling and simulations of bioengineered devices: Endoprostheses, prostheses and orthoses, Proc Inst Mech Eng H 230 (2016) 607–638. https://doi.org/10.1177/0954411916643343.

[11] K.S. Prakash, T. Nancharaih, V.V.S. Rao, Additive Manufacturing Techniques in Manufacturing -An Overview, Mater Today Proc 5 (2018) 3873–3882. https://doi.org/10.1016/J.MATPR.2017.11.642.

[12] M. Attaran, The rise of 3-D printing: The advantages of additive manufacturing over traditional manufacturing, Bus Horiz 60 (2017) 677–688. https://doi.org/10.1016/J.BUSHOR.2017.05.011.

[13] T.D. Ngo, A. Kashani, G. Imbalzano, K.T.Q. Nguyen, D. Hui, Additive manufacturing (3D printing): A review of materials, methods, applications and challenges, Compos B Eng 143 (2018) 172–196. https://doi.org/10.1016/J.COMPOSITESB.2018.02.012.

[14] R.M. Ferraro, P.S. Ginestra, G. Lanzi, S. Giliani, E. Ceretti, Production of Micro-patterned Substrates to Direct Human iPSCs-derived Neural Stem Cells Orientation and Interaction, Procedia CIRP 65 (2017) 225–230. https://doi.org/10.1016/J.PROCIR.2017.04.044.

[15] E. L. Melgoza, G. Vallicrosa, L. Serenó, J. Ciurana, C. A. Rodríguez, Rapid tooling using 3D printing system for manufacturing of customized tracheal stent, Rapid Prototyp J 20 (2014) 2–12. https://doi.org/10.1108/RPJ-01-2012-0003.

[16] I.T. Ozbolat, K.K. Moncal, H. Gudapati, Evaluation of bioprinter technologies, Addit Manuf 13 (2017) 179–200. https://doi.org/10.1016/J.ADDMA.2016.10.003.

[17] R. Landers, R. Mülhaupt, Desktop manufacturing of complex objects, prototypes and biomedical scaffolds by means of computer-assisted design combined with computer-guided 3D plotting of polymers and reactive oligomers, Macromol Mater Eng 282 (2000) 17–21.

[18] M.S. Freitas, L. Serenó, Z.C. Silveira, J.V.L. Da Silva, J. Ciurana, Thermal model for curing implantable silicone in the moulding process applied to tracheal stents, Appl Therm Eng 75 (2015) 1001–1010. https://doi.org/10.1016/J.APPLTHERMALENG.2014.10.053.

[19] Rasband W.S., Image J, U. S. National Institutes of Health, Bethesda, Maryland, USA , (1997-2014) Http://Imagej.Nih.Gov/Ij/ (n.d.).

Section 4.3

[1] L. Moroni, T. Boland, J.A. Burdick, C. De Maria, B. Derby, G. Forgacs, J. Groll, Q. Li, J. Malda, V.A. Mironov, C. Mota, M. Nakamura, W. Shu, S. Takeuchi, T.B.F. Woodfield, T. Xu, J.J. Yoo, G. Vozzi, Biofabrication: A Guide to Technology and Terminology, Trends Biotechnol 36 (2018) 384–402. https://doi.org/10.1016/j.tibtech.2017.10.015.

[2] M.P. Francis, N. Kemper, Y. Maghdouri-White, N. Thayer, Additive manufacturing for biofabricated medical device applications, in: Addit Manuf, Elsevier, 2018: pp. 311–344. https://doi.org/10.1016/B978-0-12-812155-9.00009-8.

[3] A. Schwab, R. Levato, M. D'Este, S. Piluso, D. Eglin, J. Malda, Printability and Shape Fidelity of Bioinks in 3D Bioprinting, Chem Rev 120 (2020) 11028–11055. https://doi.org/10.1021/acs.chemrev.0c00084.

[4] A. Skardal, A. Atala, Biomaterials for Integration with 3-D Bioprinting, Ann Biomed Eng 43 (2015) 730–746. https://doi.org/10.1007/s10439-014-1207-1.

[5] R.M. Ferraro, M. Seiti, P.S. Ginestra, E.L. Mazzoldi, E. Ferraris, E. Ceretti, S. Giliani, Biocompatibility evaluation of encapsulated silver-based printed circuits for in-vitro long-term sensing devices, Procedia CIRP 110 (2022) 99–104. https://doi.org/10.1016/J.PROCIR.2022.06.020.

[6] M. Seiti, P.S. Ginestra, E. Ceretti, E. Ferraris, A. Ranga, Emerging Three-Dimensional Integrated Systems for Biomimetic Neural In Vitro Cultures, Adv Mater Interfaces 9 (2022). https://doi.org/10.1002/admi.202101297.

[7] L. Ouyang, R. Yao, Y. Zhao, W. Sun, Effect of bioink properties on printability and cell viability for 3D bioplotting of embryonic stem cells, Biofabrication 8 (2016) 035020. https://doi.org/10.1088/1758-5090/8/3/035020.

[8] P. Bajaj, R.M. Schweller, A. Khademhosseini, J.L. West, R. Bashir, 3D Biofabrication Strategies for Tissue Engineering and Regenerative Medicine, Annu Rev Biomed Eng 16 (2014) 247–276. https://doi.org/10.1146/annurev-bioeng-071813-105155.

[9] D.J. Shiwarski, A.R. Hudson, J.W. Tashman, A.W. Feinberg, Emergence of FRESH 3D printing as a platform for advanced tissue biofabrication, APL Bioeng 5 (2021). https://doi.org/10.1063/5.0032777.

[10] F. Kreimendahl, C. Kniebs, A.M. Tavares Sobreiro, T. Schmitz-Rode, S. Jockenhoevel, A.L. Thiebes, FRESH bioprinting technology for tissue engineering – the influence of printing process and bioink composition on cell behavior and vascularization, J Appl Biomater Funct Mater 19 (2021) 228080002110288. https://doi.org/10.1177/22808000211028808.

[11] J. Lewicki, J. Bergman, C. Kerins, O. Hermanson, Optimization of 3D bioprinting of human neuroblastoma cells using sodium alginate hydrogel, Bioprinting 16 (2019) e00053. https://doi.org/10.1016/J.BPRINT.2019.E00053.

[12] P.P. Shah, H.B. Shah, K.K. Maniar, T. Özel, Extrusion-based 3D bioprinting of alginate-based tissue constructs, in: Procedia CIRP, 2020: pp. 143–148. https://doi.org/10.1016/j.procir.2020.06.007.

[13] K.Y. Lee, D.J. Mooney, Alginate: Properties and biomedical applications, Prog Polym Sci 37 (2012) 106–126. https://doi.org/10.1016/J.PROGPOLYMSCI.2011.06.003.

[14] P. BÃ©guin, J.-P. Aubert, The biological degradation of cellulose, FEMS Microbiol Rev 13 (1994) 25–58. https://doi.org/10.1111/j.1574-6976.1994.tb00033.x.

[15] R.J. Hickey, A.E. Pelling, Cellulose Biomaterials for Tissue Engineering, Front Bioeng Biotechnol 7 (2019). https://doi.org/10.3389/fbioe.2019.00045.
[16] Y. Ogushi, S. Sakai, K. Kawakami, Synthesis of enzymatically-gellable carboxymethylcellulose for biomedical applications, J Biosci Bioeng 104 (2007) 30–33. https://doi.org/10.1263/jbb.104.30.
[17] S.R. Muppalla, S.R. Kanatt, S.P. Chawla, A. Sharma, Carboxymethyl cellulose–polyvinyl alcohol films with clove oil for active packaging of ground chicken meat, Food Packag Shelf Life 2 (2014) 51–58. https://doi.org/10.1016/J.FPSL.2014.07.002.
[18] N. Lavoine, I. Desloges, A. Dufresne, J. Bras, Microfibrillated cellulose – Its barrier properties and applications in cellulosic materials: A review, Carbohydr Polym 90 (2012) 735–764. https://doi.org/10.1016/j.carbpol.2012.05.026.
[19] R. Ramakrishnan, N. Kasoju, R. Raju, R. Geevarghese, A. Gauthaman, A. Bhatt, Exploring the Potential of Alginate-Gelatin-Diethylaminoethyl Cellulose-Fibrinogen based Bioink for 3D Bioprinting of Skin Tissue Constructs, Carbohydrate Polymer Technologies and Applications 3 (2022) 100184. https://doi.org/10.1016/J.CARPTA.2022.100184.
[20] H. Seddiqi, E. Oliaei, H. Honarkar, J. Jin, L.C. Geonzon, R.G. Bacabac, J. Klein-Nulend, Cellulose and its derivatives: towards biomedical applications, Cellulose 28 (2021) 1893–1931. https://doi.org/10.1007/s10570-020-03674-w.
[21] J. Li, Y. Wu, J. He, Y. Huang, A new insight to the effect of calcium concentration on gelation process and physical properties of alginate films, J Mater Sci 51 (2016) 5791–5801. https://doi.org/10.1007/s10853-016-9880-0.
[22] V. Kokol, Influence of hydroxyethyl and carboxymethyl celluloses on the rheology, water retention and surface tension of water-suspended microfibrillated cellulose, Cellulose 29 (2022) 7063–7081. https://doi.org/10.1007/s10570-022-04737-w.
[23] M.E. Cooke, D.H. Rosenzweig, The rheology of direct and suspended extrusion bioprinting, APL Bioeng 5 (2021). https://doi.org/10.1063/5.0031475.

Section 4.4

[1] S. Vijayavenkataraman, N. Vialli, J.Y.H. Fuh, W.F. Lu, Conductive collagen/polypyrrole-b-polycaprolactone hydrogel for bioprinting of neural tissue constructs., Int J Bioprint 5 (2019) 229. https://doi.org/10.18063/ijb.v5i2.1.229.
[2] S. Vijayavenkataraman, W.-C. Yan, W.F. Lu, C.-H. Wang, J.Y.H. Fuh, 3D bioprinting of tissues and organs for regenerative medicine., Adv Drug Deliv Rev 132 (2018) 296–332. https://doi.org/10.1016/j.addr.2018.07.004.
[3] S.F. Badylak, R.M. Nerem, Progress in tissue engineering and regenerative medicine., Proc Natl Acad Sci U S A 107 (2010) 3285–3286. https://doi.org/10.1073/pnas.1000256107.
[4] E. Furman, The dynamic state of patents in regenerative medicine, Tissue Eng Regen Med 10 (2013) 230–233. https://doi.org/10.1007/s13770-013-1082-0.
[5] J. Jang, J.Y. Park, G. Gao, D.-W. Cho, Biomaterials-based 3D cell printing for next-generation therapeutics and diagnostics., Biomaterials 156 (2018) 88–106. https://doi.org/10.1016/j.biomaterials.2017.11.030.

[6] J.E. Kim, S.H. Kim, Y. Jung, Current status of three-dimensional printing inks for soft tissue regeneration., Tissue Eng Regen Med 13 (2016) 636–646. https://doi.org/10.1007/s13770-016-0125-8.

[7] C.-S. Cho, J.J. Yoo, Three-dimensional printing in tissue engineering and regenerative medicine, Tissue Eng Regen Med 13 (2016) 611. https://doi.org/10.1007/s13770-016-9999-8.

[8] M.M. Stanton, J. Samitier, S. Sánchez, Bioprinting of 3D hydrogels, Lab Chip 15 (2015) 3111–3115. https://doi.org/10.1039/C5LC90069G.

[9] F. Pati, J. Jang, D.-H. Ha, S. Won Kim, J.-W. Rhie, J.-H. Shim, D.-H. Kim, D.-W. Cho, Printing three-dimensional tissue analogues with decellularized extracellular matrix bioink., Nat Commun 5 (2014) 3935. https://doi.org/10.1038/ncomms4935.

[10] S.-H. Park, C.S. Jung, B.-H. Min, Advances in three-dimensional bioprinting for hard tissue engineering., Tissue Eng Regen Med 13 (2016) 622–635. https://doi.org/10.1007/s13770-016-0145-4.

[11] S. Tian, H. Zhao, N. Lewinski, Key parameters and applications of extrusion-based bioprinting, Bioprinting 23 (2021) e00156. https://doi.org/https://doi.org/10.1016/j.bprint.2021.e00156.

[12] Y.-J. Choi, H. Park, D.-H. Ha, H.-S. Yun, H.-G. Yi, H. Lee, 3D Bioprinting of In Vitro Models Using Hydrogel-Based Bioinks, Polymers (Basel) 13 (2021). https://doi.org/10.3390/polym13030366.

[13] G. Choe, S. Oh, J.M. Seok, S.A. Park, J.Y. Lee, Graphene oxide/alginate composites as novel bioinks for three-dimensional mesenchymal stem cell printing and bone regeneration applications, Nanoscale 11 (2019) 23275–23285. https://doi.org/10.1039/c9nr07643c.

[14] P. Liu, H. Shen, Y. Zhi, J. Si, J. Shi, L. Guo, S.G. Shen, 3D bioprinting and in vitro study of bilayered membranous construct with human cells-laden alginate/gelatin composite hydrogels., Colloids Surf B Biointerfaces 181 (2019) 1026–1034. https://doi.org/10.1016/j.colsurfb.2019.06.069.

[15] S.Y. Sonaye, E.G. Ertugral, C.R. Kothapalli, P. Sikder, Extrusion 3D (Bio)Printing of Alginate-Gelatin-Based Composite Scaffolds for Skeletal Muscle Tissue Engineering, Materials 15 (2022). https://doi.org/10.3390/ma15227945.

[16] Y.-H. Cheng, S.-J. Cheng, H.-H. Chen, W.-C. Hsu, Development of injectable graphene oxide/laponite/gelatin hydrogel containing Wharton's jelly mesenchymal stem cells for treatment of oxidative stress-damaged cardiomyocytes., Colloids Surf B Biointerfaces 209 (2022) 112150. https://doi.org/10.1016/j.colsurfb.2021.112150.

[17] R. Ahmad Raus, W.M.F. Wan Nawawi, R.R. Nasaruddin, Alginate and alginate composites for biomedical applications., Asian J Pharm Sci 16 (2021) 280–306. https://doi.org/10.1016/j.ajps.2020.10.001.

[18] M.B. Łabowska, K. Cierluk, A.M. Jankowska, J. Kulbacka, J. Detyna, I. Michalak, A Review on the Adaption of Alginate-Gelatin Hydrogels for 3D Cultures and Bioprinting., Materials (Basel) 14 (2021). https://doi.org/10.3390/ma14040858.

[19] L.Y. Xu Xin Mu Yunping, Wang Jianying, Li Fanghong, Zhao Zijian, Preparation and biological evaluation of decellularized dermal matrix hydrogel, Chinese Journal of Tissue Engineering Research 27 (n.d.) 3325–3331. https://www.cjter.com.

[20] J. Zhang, H. Eyisoylu, X.H. Qin, M. Rubert, R. Müller, 3D bioprinting of graphene oxide-incorporated cell-laden bone mimicking scaffolds for promoting scaffold fidelity,

osteogenic differentiation and mineralization, Acta Biomater 121 (2021) 637–652. https://doi.org/10.1016/j.actbio.2020.12.026.

[21] R. Lozano, L. Stevens, B.C. Thompson, K.J. Gilmore, R. Gorkin, E.M. Stewart, M. in het Panhuis, M. Romero-Ortega, G.G. Wallace, 3D printing of layered brain-like structures using peptide modified gellan gum substrates, Biomaterials 67 (2015) 264–273. https://doi.org/10.1016/j.biomaterials.2015.07.022.

[22] Y. Gong, F. Wang, M.S.H. Al-Furjan, L. Shan, J. He, X. Bian, Z. Bi, H. Liu, W. Li, H. Shao, G. Chen, A.B. Sulong, Experimental Investigation and Optimal 3D Bioprinting Parameters of SA-Gel Porous Cartilage Scaffold, Applied Sciences 10 (2020). https://www.mdpi.com/2076-3417/10/3/768.

[23] L. Ouyang, R. Yao, Y. Zhao, W. Sun, Effect of bioink properties on printability and cell viability for 3D bioplotting of embryonic stem cells., Biofabrication 8 (2016) 35020. https://doi.org/10.1088/1758-5090/8/3/035020.

[24] A. Kirillova, R. Maxson, G. Stoychev, C.T. Gomillion, L. Ionov, 4D Biofabrication Using Shape-Morphing Hydrogels, Advanced Materials 29 (2017) 1703443. https://doi.org/https://doi.org/10.1002/adma.201703443.

[25] P. Bikmulina, N. Kosheleva, Y. Efremov, A. Antoshin, Z. Heydari, V. Kapustina, V. Royuk, V. Mikhaylov, V. Fomin, M. Vosough, P. Timashev, Y. Rochev, A. Shpichka, 3D or not 3D: a guide to assess cell viability in 3D cell systems, Soft Matter 18 (2022) 2222–2233. https://doi.org/10.1039/D2SM00018K.

[26] G. Gaudenzi, E.L. Mazzoldi, P.S. Ginestra, A. Piccininni, Evaluation of Bioprinting Process by RSM Training, in: ISIEA 2023, Springer, In press, n.d.

[27] A. Mondal, A. Gebeyehu, M. Miranda, D. Bahadur, N. Patel, S. Ramakrishnan, A.K. Rishi, M. Singh, Characterization and printability of Sodium alginate -Gelatin hydrogel for bioprinting NSCLC co-culture., Sci Rep 9 (2019) 19914. https://doi.org/10.1038/s41598-019-55034-9.

[28] F. Fayyazbakhsh, M.J. Khayat, M.C. Leu, 3D-Printed Gelatin-Alginate Hydrogel Dressings for Burn Wound Healing: A Comprehensive Study., Int J Bioprint 8 (2022) 618. https://doi.org/10.18063/ijb.v8i4.618.

[29] G. Ninan, J. Joseph, Z.A. Aliyamveettil, A comparative study on the physical, chemical and functional properties of carp skin and mammalian gelatins., J Food Sci Technol 51 (2014) 2085–2091. https://doi.org/10.1007/s13197-012-0681-4.

[30] L. Riva, E.L. Mazzoldi, P.S. Ginestra, E. Ceretti, S.C. Giliani, Eye model for floaters' studies: production of 3D printed scaffolds, Progress in Additive Manufacturing 7 (2022) 1127–1140. https://doi.org/10.1007/s40964-022-00288-5.

[31] E.L. Mazzoldi, L. Riva, R.M. Ferraro, P.S. Ginestra, S.C. Giliani, 3D Printing of Biocompatible Scaffolds for Eye Tissue Engineering, Procedia CIRP 110 (2022) 214–219. https://doi.org/10.1016/j.procir.2022.06.039.

[32] R. Rovetta, P. Ginestra, R.M. Ferraro, K. Zohar-Hauber, S. Giliani, E. Ceretti, Building Orientation and Post Processing of Ti6Al4V Produced by Laser Powder Bed Fusion Process, Journal of Manufacturing and Materials Processing 7 (2023). https://doi.org/10.3390/jmmp7010043.

[33] R.M. Ferraro, M. Seiti, P.S. Ginestra, E.L. Mazzoldi, E. Ferraris, E. Ceretti, S. Giliani, Biocompatibility evaluation of encapsulated silver-based printed circuits for in-vitro long-term sensing devices, Procedia CIRP 110 (2022) 99–104. https://doi.org/10.1016/j.procir.2022.06.020.

[34] T. Gao, G.J. Gillispie, J.S. Copus, A. Kumar, P. Rajan, Y. Seol, A. Atala, J.J. Yoo, S.J. Lee, Optimization of gelatin-alginate composite bioink printability using rheological parameters : a systematic approach, 10 (2019) 1–17. https://doi.org/10.1088/1758-5090/aacdc7.Optimization.

[35] A. Maihemuti, H. Zhang, X. Lin, Y. Wang, Z. Xu, D. Zhang, Q. Jiang, 3D-printed fish gelatin scaffolds for cartilage tissue engineering, Bioact Mater 26 (2023) 77–87. https://doi.org/10.1016/j.bioactmat.2023.02.007.

[36] Z. Li, S. Huang, Y. Liu, B. Yao, T. Hu, H. Shi, J. Xie, X. Fu, Tuning Alginate-Gelatin Bioink Properties by Varying Solvent and Their Impact on Stem Cell Behavior, Sci Rep 8 (2018) 1–8. https://doi.org/10.1038/s41598-018-26407-3.

[37] T. Gregory, P. Benhal, A. Scutte, D. Quashie, K. Harrison, C. Cargill, S. Grandison, M.J. Savitsky, S. Ramakrishnan, J. Ali, Rheological characterization of cell-laden alginate-gelatin hydrogels for 3D biofabrication, J Mech Behav Biomed Mater 136 (2022) 105474. https://doi.org/10.1016/j.jmbbm.2022.105474.

[38] N. Bessler, D. Ogiermann, M.-B. Buchholz, A. Santel, J. Heidenreich, R. Ahmmed, H. Zaehres, B. Brand-Saberi, Nydus One Syringe Extruder (NOSE): A Prusa i3 3D printer conversion for bioprinting applications utilizing the FRESH-method, HardwareX 6 (2019) e00069. https://doi.org/https://doi.org/10.1016/j.ohx.2019.e00069.

[39] F. Kreimendahl, C. Kniebs, A.M. Tavares Sobreiro, T. Schmitz-Rode, S. Jockenhoevel, A.L. Thiebes, FRESH bioprinting technology for tissue engineering - the influence of printing process and bioink composition on cell behavior and vascularization., J Appl Biomater Funct Mater 19 (2021) 22808000211028810. https://doi.org/10.1177/22808000211028808.

Chapter 5

Section 5.1

[1] R. Velu, T. Calais, A. Jayakumar, F. Raspall, A Comprehensive Review on Bio-Nanomaterials for Medical Implants and Feasibility Studies on Fabrication of Such Implants by Additive Manufacturing Technique, Materials 13 (2019) 92. https://doi.org/10.3390/ma13010092.

[2] P.S. Ginestra, E. Ceretti, A. Fiorentino, Potential of modeling and simulations of bioengineered devices: Endoprostheses, prostheses and orthoses, Proc Inst Mech Eng H 230 (2016) 607–638. https://doi.org/10.1177/0954411916643343.

[3] F. Bayata, C. Yildiz, The effects of design parameters on mechanical failure of Ti-6Al-4V implants using finite element analysis, Eng Fail Anal 110 (2020) 104445. https://doi.org/10.1016/J.ENGFAILANAL.2020.104445.

[4] S. Doliveux, F.Z. Jamjoom, M. Nadra, G.O. Gallucci, A. Hamilton, Fabrication technique for a custom implant emergence profile on 3D printed casts, J Prosthet Dent 123 (2020) 571–575. https://doi.org/10.1016/J.PROSDENT.2019.03.016.

[5] Angelats Lobo, Ginestra, Cell Bioprinting: The 3D-Bioplotter™ Case, Materials 12 (2019) 4005. https://doi.org/10.3390/ma12234005.

[6] M. Lowther, S. Louth, A. Davey, A. Hussain, P. Ginestra, L. Carter, N. Eisenstein, L. Grover, S. Cox, Clinical, industrial, and research perspectives on powder bed fusion

additively manufactured metal implants, Addit Manuf 28 (2019) 565–584. https://doi.org/10.1016/J.ADDMA.2019.05.033.

[7] M. Tilton, G.S. Lewis, H. Bok Wee, A. Armstrong, M.W. Hast, G. Manogharan, Additive manufacturing of fracture fixation implants: Design, material characterization, biomechanical modeling and experimentation, Addit Manuf 33 (2020) 101137. https://doi.org/10.1016/J.ADDMA.2020.101137.

[8] C.H. Li, C.H. Wu, C.L. Lin, Design of a patient-specific mandible reconstruction implant with dental prosthesis for metal 3D printing using integrated weighted topology optimization and finite element analysis, J Mech Behav Biomed Mater 105 (2020) 103700. https://doi.org/10.1016/J.JMBBM.2020.103700.

[9] J. Ni, H. Ling, S. Zhang, Z. Wang, Z. Peng, C. Benyshek, R. Zan, A.K. Miri, Z. Li, X. Zhang, J. Lee, K.J. Lee, H.J. Kim, P. Tebon, T. Hoffman, M.R. Dokmeci, N. Ashammakhi, X. Li, A. Khademhosseini, Three-dimensional printing of metals for biomedical applications, Mater Today Bio 3 (2019) 100024. https://doi.org/10.1016/J.MTBIO.2019.100024.

[10] M. Nirish, R. Rajendra, Suitability of metal additive manufacturing processes for part topology optimization – A comparative study, Mater Today Proc 27 (2020) 1601–1607. https://doi.org/10.1016/J.MATPR.2020.03.275.

[11] D. Zhao, C. Han, Y. Li, J. Li, K. Zhou, Q. Wei, J. Liu, Y. Shi, Improvement on mechanical properties and corrosion resistance of titanium-tantalum alloys in-situ fabricated via selective laser melting, J Alloys Compd 804 (2019) 288–298. https://doi.org/10.1016/J.JALLCOM.2019.06.307.

[12] W.M.I. Makhetha, T.H. Becker, N. Sacks, Post-Processing Framework for As-Built LPBF Ti-6Al-4V Parts Towards Meeting Industry Functional Requirements, JOM 74 (2022) 764–776. https://doi.org/10.1007/s11837-021-05078-y.

[13] T. Grover, A. Pandey, S.T. Kumari, A. Awasthi, B. Singh, P. Dixit, P. Singhal, K.K. Saxena, Role of titanium in bio implants and additive manufacturing: An overview, Mater Today Proc 26 (2020) 3071–3080. https://doi.org/10.1016/J.MATPR.2020.02.636.

[14] L. Zhang, L. Chen, A Review on Biomedical Titanium Alloys: Recent Progress and Prospect, Adv Eng Mater 21 (2019). https://doi.org/10.1002/adem.201801215.

[15] A.M. Khorasani, M. Goldberg, E.H. Doeven, G. Littlefair, Titanium in Biomedical Applications—Properties and Fabrication: A Review, J Biomater Tissue Eng 5 (2015) 593–619. https://doi.org/10.1166/jbt.2015.1361.

[16] S.S. Sidhu, M.A.-H. Gepreel, M. Bahraminasab, Advances in titanium bio-implants: Alloy design, surface engineering and manufacturing processes, J Mater Res 37 (2022) 2487–2490. https://doi.org/10.1557/s43578-022-00661-8.

[17] Y.K. Balasubramanian Gayathri, R.L. Kumar, V.V. Ramalingam, G.S. Priyadharshini, K.S. Kumar, T.R. Prabhu, Additive Manufacturing of Ti-6Al-4V alloy for Biomedical Applications, J Bio Tribocorros 8 (2022) 98. https://doi.org/10.1007/s40735-022-00700-1.

[18] L.E. Murr, Metallurgy principles applied to powder bed fusion 3D printing/additive manufacturing of personalized and optimized metal and alloy biomedical implants: an overview, Journal of Materials Research and Technology 9 (2020) 1087–1103. https://doi.org/10.1016/J.JMRT.2019.12.015.

[19] B. Gaur, D. Soman, R. Ghyar, R. Bhallamudi, Ti6Al4V scaffolds fabricated by laser powder bed fusion with hybrid volumetric energy density, Rapid Prototyp J 29 (2023) 67–79. https://doi.org/10.1108/RPJ-01-2022-0036.

[20] A.N. Aufa, M.Z. Hassan, Z. Ismail, Recent advances in Ti-6Al-4V additively manufactured by selective laser melting for biomedical implants: Prospect development, J Alloys Compd 896 (2022) 163072. https://doi.org/10.1016/J.JALLCOM.2021.163072.

[21] M.A. Buhairi, F.M. Foudzi, F.I. Jamhari, A.B. Sulong, N.A.M. Radzuan, N. Muhamad, I.F. Mohamed, A.H. Azman, W.S.W. Harun, M.S.H. Al-Furjan, Review on volumetric energy density: influence on morphology and mechanical properties of Ti6Al4V manufactured via laser powder bed fusion, Progress in Additive Manufacturing 8 (2023) 265–283. https://doi.org/10.1007/s40964-022-00328-0.

[22] H. Eskandari, H.R. Lashgari, Sh. Zangeneh, C. Kong, L. Ye, M. Eizadjou, H. Wang, Microstructural characterization and mechanical properties of SLM-printed Ti–6Al–4V alloy: Effect of build orientation, J Mater Res 37 (2022) 2645–2660. https://doi.org/10.1557/s43578-021-00468-z.

[23] P. Krakhmalev, G. Fredriksson, I. Yadroitsava, N. Kazantseva, A. Du Plessis, I. Yadroitsev, Deformation Behavior and Microstructure of Ti6Al4V Manufactured by SLM, Phys Procedia 83 (2016) 778–788. https://doi.org/10.1016/J.PHPRO.2016.08.080.

[24] T.A. Mukalay, J.A. Trimble, K. Mpofu, R. Muvunzi, A systematic review of process uncertainty in Ti6Al4V-selective laser melting, CIRP J Manuf Sci Technol 36 (2022) 185–212. https://doi.org/10.1016/J.CIRPJ.2021.12.005.

[25] L.N. Carter, V.M. Villapún, L. Grover, S.C. Cox, Exploring the duality of powder adhesion and underlying surface roughness in laser powder bed fusion processed Ti-6Al-4V, J Manuf Process 81 (2022) 14–26. https://doi.org/10.1016/J.JMAPRO.2022.06.057.

[26] L.C.P. Dos Santos, F.C. Malheiros, A.Z. Guarato, Surface parameters of as-built additive manufactured metal for intraosseous dental implants, J Prosthet Dent 124 (2020) 217–222. https://doi.org/10.1016/J.PROSDENT.2019.09.010.

[27] G.M. Rodriguez, J. Bowen, M. Zelzer, A. Stamboulis, Selective modification of Ti6Al4V surfaces for biomedical applications, RSC Adv 10 (2020) 17642–17652. https://doi.org/10.1039/C9RA11000C.

[28] W. Zhou, X. Peng, Y. Ma, Y. Hu, Y. Wu, F. Lan, M.D. Weir, M. Li, B. Ren, T.W. Oates, H.H.K. Xu, X. Zhou, L. Cheng, Two-staged time-dependent materials for the prevention of implant-related infections, Acta Biomater 101 (2020) 128–140. https://doi.org/10.1016/J.ACTBIO.2019.10.023.

[29] A. Sarker, N. Tran, A. Rifai, M. Brandt, P.A. Tran, M. Leary, K. Fox, R. Williams, Rational design of additively manufactured Ti6Al4V implants to control Staphylococcus aureus biofilm formation, Materialia (Oxf) 5 (2019) 100250. https://doi.org/10.1016/J.MTLA.2019.100250.

[30] K. Xie, Y. Guo, S. Zhao, L. Wang, J. Wu, J. Tan, Y. Yang, W. Wu, W. Jiang, Y. Hao, Partially Melted Ti6Al4V Particles Increase Bacterial Adhesion and Inhibit Osteogenic Activity on 3D-printed Implants: An In Vitro Study, Clin Orthop Relat Res 477 (2019) 2772–2782. https://doi.org/10.1097/CORR.0000000000000954.

[31] B. Ren, Y. Wan, C. Liu, H. Wang, M. Yu, X. Zhang, Y. Huang, Improved osseointegration of 3D printed Ti-6Al-4V implant with a hierarchical micro/nano surface topography: An in vitro and in vivo study, Materials Science and Engineering: C 118 (2021) 111505. https://doi.org/10.1016/J.MSEC.2020.111505.

[32] P. Ginestra, A. Fiorentino, E. Ceretti, Micro-structuring of Titanium Collectors by Laser Ablation Technique: A Promising Approach to Produce Micro-patterned Scaffolds for Tissue Engineering Applications, Procedia CIRP 65 (2017) 19–24. https://doi.org/10.1016/J.PROCIR.2017.04.043.

[33] P.S. Ginestra, S. Pandini, A. Fiorentino, P. Benzoni, P. Dell'Era, E. Ceretti, Microstructured scaffold for guided cellular orientation: Poly(ε-caprolactone) electrospinning on laser ablated titanium collector, CIRP J Manuf Sci Technol 19 (2017) 147–157. https://doi.org/10.1016/J.CIRPJ.2017.08.002.

[34] A. Malik, S. Rouf, M.I. Ul Haq, A. Raina, A.P. Valerga Puerta, B. Sagbas, A. Ruggiero, Tribo-corrosive behavior of additive manufactured parts for orthopaedic applications, J Orthop 34 (2022) 49–60. https://doi.org/10.1016/J.JOR.2022.08.006.

[35] N. Erwin, D. Sur, G.B. Basim, Remediation of machining medium effect on biocompatibility of titanium-based dental implants by chemical mechanical nano-structuring, J Mater Res 37 (2022) 2686–2697. https://doi.org/10.1557/s43578-022-00553-x.

[36] S. Dwivedi, A.R. Dixit, A.K. Das, K. Adamczuk, Additive texturing of metallic implant surfaces for improved wetting and biotribological performance, Journal of Materials Research and Technology 20 (2022) 2650–2667. https://doi.org/10.1016/J.JMRT.2022.08.029.

[37] J. Zhang, C. Zhao, R. Sheng, K. Lin, X. Wang, S. Zhang, Construction of a Hierarchical Micro-/Submicro-/Nanostructured 3D-Printed Ti6Al4V Surface Feature to Promote Osteogenesis: Involvement of Sema7A through the ITGB1/FAK/ERK Signaling Pathway, ACS Appl Mater Interfaces 14 (2022) 30571–30581. https://doi.org/10.1021/acsami.2c06454.

[38] H. Wang, J. Liu, C. Wang, S.G. Shen, X. Wang, K. Lin, The synergistic effect of 3D-printed microscale roughness surface and nanoscale feature on enhancing osteogenic differentiation and rapid osseointegration, J Mater Sci Technol 63 (2021) 18–26. https://doi.org/10.1016/J.JMST.2019.12.030.

[39] J. Stepanovska, R. Matejka, M. Otahal, J. Rosina, L. Bacakova, The Effect of Various Surface Treatments of Ti6Al4V on the Growth and Osteogenic Differentiation of Adipose Tissue-Derived Stem Cells, Coatings 10 (2020) 762. https://doi.org/10.3390/coatings10080762.

[40] P. Ginestra, R.M. Ferraro, K. Zohar-Hauber, A. Abeni, S. Giliani, E. Ceretti, Selective Laser Melting and Electron Beam Melting of Ti6Al4V for Orthopedic Applications: A Comparative Study on the Applied Building Direction, Materials 13 (2020) 5584. https://doi.org/10.3390/ma13235584.

[41] M. İzmir, B. Ercan, Anodization of titanium alloys for orthopedic applications, Front Chem Sci Eng 13 (2019) 28–45. https://doi.org/10.1007/s11705-018-1759-y.

[42] M. Manjaiah, R.F. Laubscher, Effect of anodizing on surface integrity of Grade 4 titanium for biomedical applications, Surf Coat Technol 310 (2017) 263–272. https://doi.org/10.1016/j.surfcoat.2016.12.038.

[43] K.-Y. Hung, Y.-C. Lin, H.-P. Feng, The Effects of Acid Etching on the Nanomorphological Surface Characteristics and Activation Energy of Titanium Medical Materials, Materials 10 (2017) 1164. https://doi.org/10.3390/ma10101164.

[44] M.A. Surmeneva, D. Khrapov, K. Prosolov, M. Kozadayeva, A. Koptyug, A. Volkova, A. Paveleva, R.A. Surmenev, The influence of chemical etching on porous structure and

mechanical properties of the Ti6AL4V Functionally Graded Porous Scaffolds fabricated by EBM, Mater Chem Phys 275 (2022) 125217. https://doi.org/10.1016/j.matchemphys.2021.125217.

[45] R. Bright, A. Hayles, J. Wood, N. Ninan, D. Palms, R.M. Visalakshan, A. Burzava, T. Brown, D. Barker, K. Vasilev, Bio-Inspired Nanostructured Ti-6Al-4V Alloy: The Role of Two Alkaline Etchants and the Hydrothermal Processing Duration on Antibacterial Activity, Nanomaterials 12 (2022) 1140. https://doi.org/10.3390/nano12071140.

[46] ASTM B214-16, Standard Test Method for Sieve Analysis of Metal Powders, in: ASTM: West Conshohocken, PA, USA, 2016.

[47] ASTM F2924-14, Standard Specification for Additive Manufacturing Titanium-6 Aluminum-4 Vanadium with Powder Bed Fusion, ASTM: West Conshohocken, PA, USA 10.04 (2014).

[48] ASTM F1472-08, Standard Specification for Wrought Titanium-6Aluminum-4Vanadium Alloy for Surgical Implant Applications, ASTM: West Conshohocken, PA, USA 10.15 (2008).

[49] F. Yazid, A.N.M. Kay, W.Y. Qin, N.A. Luchman, R.M.A. Wahab, S.H.Z. Ariffin, Morphology and Osteogenic Capability of MC3T3-E1 Cells on Granular Hydroxyapatite Scaffold, Journal of Biological Sciences 19 (2019) 201–209. https://doi.org/10.3923/jbs.2019.201.209.

[50] E.H. Jimenez, A. Kreitcberg, E. Moquin, V. Brailovski, Influence of Post-Processing Conditions on the Microstructure, Static, and Fatigue Resistance of Laser Powder Bed Fused Ti-6Al-4V Components, Journal of Manufacturing and Materials Processing 6 (2022) 85. https://doi.org/10.3390/jmmp6040085.

[51] D. Chen, Y. Li, X. Zhao, H. He, G. Sun, W. Li, X. Wang, Spray-deposited Ag nanoparticles on micro/nano structured Ti6Al4V surface for enhanced bactericidal property and cytocompatibility, Surf Coat Technol 431 (2022) 128010. https://doi.org/10.1016/j.surfcoat.2021.128010.

[52] M.A. Obeidi, A. Mussatto, M.N. Dogu, S.P. Sreenilayam, E. McCarthy, I.U. Ahad, S. Keaveney, D. Brabazon, Laser surface polishing of Ti-6Al-4V parts manufactured by laser powder bed fusion, Surf Coat Technol 434 (2022) 128179. https://doi.org/10.1016/j.surfcoat.2022.128179.

[53] L. Damiati, M.G. Eales, A.H. Nobbs, B. Su, P.M. Tsimbouri, M. Salmeron-Sanchez, M.J. Dalby, Impact of surface topography and coating on osteogenesis and bacterial attachment on titanium implants, J Tissue Eng 9 (2018) 204173141879069. https://doi.org/10.1177/2041731418790694.

[54] P. Ginestra, E. Ceretti, D. Lobo, M. Lowther, S. Cruchley, S. Kuehne, V. Villapun, S. Cox, L. Grover, D. Shepherd, M. Attallah, O. Addison, M. Webber, Post Processing of 3D Printed Metal Scaffolds: a Preliminary Study of Antimicrobial Efficiency, Procedia Manuf 47 (2020) 1106–1112. https://doi.org/10.1016/j.promfg.2020.04.126.